Tokyo Metropolitan University

Study on High Resolution and High Sensitivity Imaging of Scatterer Distribution in Medical Ultrasound

by

ZHU , JING

Student ID 15990504

A thesis submitted to the Department of Information and Communications Systems Engineering, Graduate School of System Design,
in partial fulfillment of the requirements for the degree of Doctor of Philosophy in Information and Communications Systems Engineering

March 2019

Contents

List of Figures

List of Tables

Chapter 1

Introduction

1.1 Brief History of Ultrasound

Sound wave technology has been used to detect objects for a long time. In 1912, the English meteorologist L. F. Richardson [1] was the first person who suggested using sound wave to detect underwater objects. Inspired by that, P. Langevin [2] proposed using sound wave to find ships, submarines and mines, which started the application of the low frequency sound wave transmission and reception. During World War II, the first radar system was developed by U.S. Navy, which used the electromagnetic waves in a pulse-echo mode to detect enemy aircrafts [3].

During the same period, an important development about ultrasonic technology started: the pulsed-echo ultrasonic metal flaw detection. The purpose of this development was to check the integrity of the metal hulls of large ships and the armor plates of battle tanks. The concept of ultrasonic metal flaw detection was first suggested by Soviet scientist S. Y. Sokolov in 1928 at the Electro Technical Institute of Leningrad [4].

Since then, ultrasonic researches have been rapidly conducted all over the world, and the medical ultrasonography technology also entered a new phase. In 1951, Dr. Wild [5] performed the first medical ultrasound diagnostic, assessing the thickness of bowel tissue by using the amplitude mode (A-mode) imaging. Later in 1956, T. Ciezynski [6] developed the first single element transducer catheter and measured a canine heart chamber. Just two years later, I. Donald and engineer T. G. Brown [7] produced a prototype of the first compound brightness mode (B-mode) contacting sector-scanner manually and automatically. In 1971, the linear array transducers were designed by a Dutch team under the direction of N. Born [8].

There is no doubt that medical ultrasonic imaging is a young technology, but it is also one of the fastest-growing medical techniques. In the last half century, medical ultrasonic imaging has been clinically tested and has progressed from barely interpretable images to one of the top choices to noninvasively image internal soft tissue structures and blood flow, such as mammography [9], laparoscopy [10], endoscopy [11], endorectal [12] and vascular diagnosis [13].

1.2 Basic Knowledge

1.2.1 The nature of ultrasound

The various sounds that people can hear are caused by the vibrations of air particles next to the source, then the vibrations reach the ear drum. Whether the ear drum can react or not depends on the frequency and amplitude of the sound. The ear drum can respond to the incoming frequencies from 20 Hz to roughly 20 kHz. Variations in the audible frequencies can be perceived, while sounds with frequencies below 20 Hz are not perceived as sound, and sounds in this range are described as infrasound. Infrasound can be dangerous for the human body due to the fact that physical damage to the ear and some loss of hearing has been found after being exposed to infrasound at the level above 140 dB. Just like infrasound, sounds with frequencies above 20 kHz are also not perceivable, and these sounds are called ultrasound. Ultrasound has a very wide use in medical and industrial applications. Fig. 1.1 presents the frequency ranges for infrasound and ultrasound.

Ultrasound waves are mechanical vibrations that typically propagate as acoustic pressure waves, through a transmission medium such as gas, liquid or solid. They are coupled modes between medium particles oscillating about equilibrium positions and a traveling

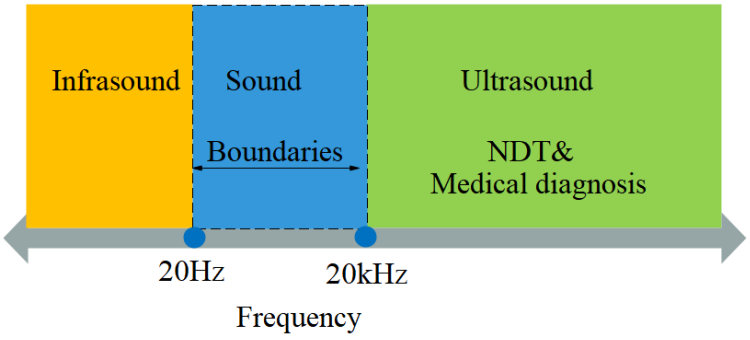

Figure 1.1: Frequency ranges for infrasound and ultrasound.

ultrasonic wave. For industrial inspection, ultrasound in solid can support the propagation of both longitudinal and transverse waves. But for medical diagnostic ultrasounds, as human body is almost entirely composed of water, only longitudinal waves can be used to probe the human body. Transverse waves may be generated in bone due to mode conversion, but those transverse waves are not easy to propagate, and the energy will be rapidly released due to the high attenuation of the bone. Therefore, transverse waves are not of great importance to the medical ultrasound [14].

1.2.2 Ultrasound imaging principles

Ultrasound imaging is built up from scan lines. Generally, ultrasonic waves propagate in every straight line, each line is based on "pulse-echo" principle [15], as shown in Fig. 1.2. First, ultrasonic waves are generated by a transducer containing a ceramic crystal which is excited by a short electrical pulse that has a typical form of several sine cycles (Fig. 1.2(a)). Through the piezoelectric effect, this electrical energy will be converted to a mechanical wave and propagated into the medium (Fig. 1.2(b)). After a complex combination of reflection, refraction, scattering and attenuation, some reflected and diffused waves will rise. Finally, these echoes are propagated back to the transducer, which will translate them into electrical signals again (Fig. 1.2(c)).

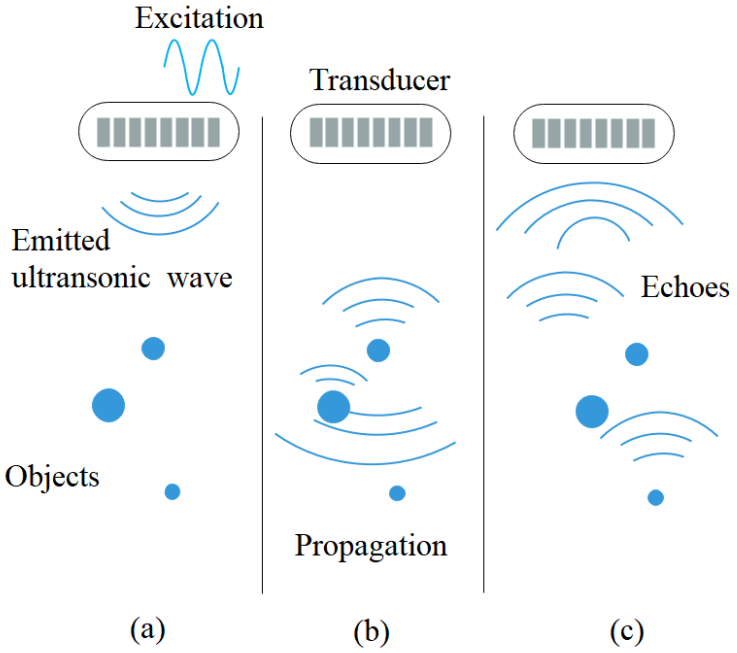

Figure 1.2: The principle of ultrasound imaging: (a) an electrical pulse (excitation) is transmitted to the piezoelectric transducer, transforming the pulse into an ultrasound wave; (b) the wave propagates and interacts with the medium; (c) the reflected waves received by the transducer are transformed in electrical signals.

Until now, we have explained the basic principle of ultrasound imaging. For a better understanding of the principle, we will also describe the mathematical equation. The wave equation is typically written and solved in terms of pressure, displacement, or velocity potentials [16].

As a wave in homogeneous medium without attenuation is at a position *(x, y, z)* of the propagating space and at a time t can be described by a second-order differential equation:

$$\frac{1}{c^2}\,\frac{\partial^2 P(x,y,z,t)}{\partial t^2} = \nabla^2 P, \tag{1.1}$$

where

$$\nabla^2 = \frac{\partial^2}{\partial x^2} + \frac{\partial^2}{\partial y^2} + \frac{\partial^2}{\partial z^2} \tag{1.2}$$

is the Laplacian operator. P and c are the sound pressure and velocity, respectively.

In the medium, the wave velocity c has the expression:

$$c = \sqrt{\frac{E}{\rho}}, \tag{1.3}$$

where ρ is the medium density and E is the bulk modulus. The average velocity of sound in the human body is 1540 m/s. Table 1.1 lists the typical values of acoustic parameters for some relevant tissues [17]. The other parameters of the Table 1.1 will be defined in the following subsection.

Any wave can be mathematically regarded as one of the solutions that satisfy the Eq. 1.1 and the boundary condition, in a steady state. In the case of this study, the plane wave

Table 1.1: Some parameters include the velocity, acoustic impedance and attenuation coefficients for common biological materials

Material	c [m/s]	Z $[kg \cdot m^{-2} \cdot sec^{-1}] \times 10^{-4}$	α [dB/cm] at 1 MHz
Air	330	0.0004	12
Water	1480	1.48	0.0022
Fat	1450-1460	1.34-1.38	0.52
Brain	1560	1.55	0.85
Liver	1555-1570	1.65	0.96
Kidney	1560	1.62	1.0
Spleen	1570	1.64	1.0
Blood	1550-1560	1.61-1.65	0.167
Muscle	1550-1600	1.62-1.71	1.3-3.3
Lens of eye	1620	1.85	2.0
Skull bone	3360-4080	6.0-7.8	11.3

propagates in the x direction, and the result is given by:

$$P(x,t) = Ae^{j(kx-\omega t)}, \tag{1.4}$$

where A is the amplitude of the propagating signal, ω is the angular frequency, and $k = \omega/\mathrm{c}$ is the wavenumber. In fact, the plane wave equation can calculate the displacement at any point in a one-dimensional (1D) medium as waves travel in it at velocity c.

1.2.3 Reflection and transmission

When a wave occurs at an interface between two dissimilar media, some of the waves are reflected in the specular direction, some of the waves are scattered in all directions of the incident medium, and some of them are transmitted through the interface. The behavior of the wave's interaction with an interface is illustrated in Fig. 1.3.

In engineering, it is common to consider that the plane wave in the Eq. 1.4 propagates through the medium and is reflected, thereby the measured signal at the transducer can be defined as:

$$y(t) = Ae^{j(kx-\omega t)}. \tag{1.5}$$

The acoustic properties of the medium are characterized by acoustic impedance. Usually, the acoustic impedance is the ratio of acoustic pressure to the associated particle velocity. It allows us to calculate the reflection and transmission at boundaries. We have the acoustic impedance, Z:

$$Z = P/\mu = \rho c\mu/\mu = \rho c, \tag{1.6}$$

where μ is an associated particle velocity. Through the propagation of the wave in the medium, a portion of the incident energy is reflected, while the other portion is transmitted, as illustrated in Fig. 1.4. The reflection coefficient R is used to measure the reflection between two adjacent tissues with different impedances:

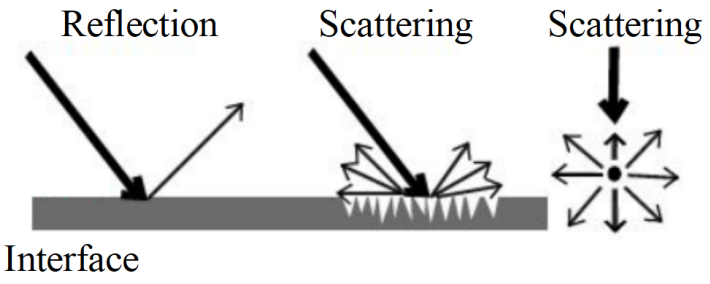

Figure 1.3: The behavior of the wave at an interface and in a small scatterer.

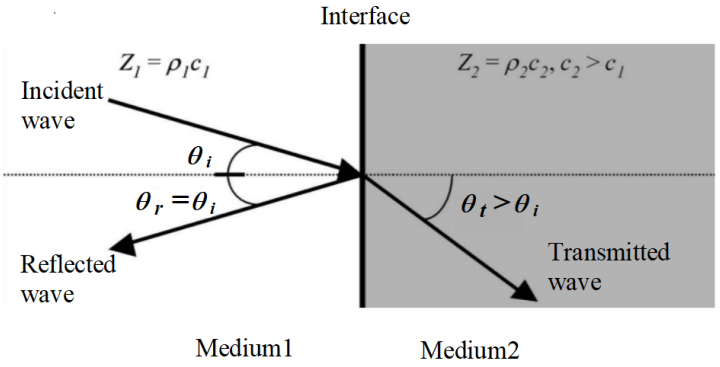

Figure 1.4: Reflection and transmission for non-perpendicular incidence of an ultrasound wave on a planar interface between two media with different acoustic impedances.

$$R = \frac{P_r}{P_i} = (\frac{Z_2}{\cos\theta_t} - \frac{Z_1}{\cos\theta_i})^2 / (\frac{Z_2}{\cos\theta_t} + \frac{Z_1}{\cos\theta_i})^2. \tag{1.7}$$

The transmission coefficient can be calculated by:

$$T = \frac{P_t}{P_i} = 1 - R. \tag{1.8}$$

The degree of bending the sound wave undergoes as it travels through media of different velocities is dictated by Snell's Law [18]. This law states that the index of refraction of the incident medium multiplied by the sine of the incident angle is equal to the index of refraction of the refracting medium multiplied by the sine of the refracted angle.

$$\theta_i = \theta_r,$$

$$\frac{\sin\theta_i}{\sin\theta_t} = \frac{c_1}{c_2}, \tag{1.9}$$

where θ_i, θ_r and θ_t are the angles of incidence, reflection, and transmission, respectively. Especially, when $\theta_i = \theta_t = 0$, we can rewrite Eq. 1.7 as follows:

$$R = \frac{(Z_2 - Z_1)^2}{(Z_2 + Z_1)^2}. \tag{1.10}$$

Considering a soft tissue as the interface, the acoustic impedance of some common biological tissues is presented in Table 1.1. It can be seen that the intensity of the reflected ultrasound wave at some interfaces can reach 0.1% of the incident intensity. The reflection on other types of interfaces (e.g., skull bone) can be higher due to the higher specific acoustic impedance.

1.2.4 Scattering, absorption and attenuation

If there are microscopic irregularities when ultrasonic waves propagate through the interface, it will generate diffuse scattering instead of specular reflection. As illustrated in the Fig. 1.3. The same goes for ultrasound waves passing through the medium of a human body: if there are irregularities, roughness and density fluctuations, some of the waves will deviate from their original trajectory. Scattering also occurs when the dimension of the target is negligible in relation to the wavelength (e.g., blood cells).

In a physical description of the phenomenon, we distinguish between two types of scattering, namely elastic and inelastic. Elastic scattering involves no (or a very small) loss or gain of energy, whereas inelastic scattering does involve some changes in energy. If the wave is substantially or completely extinguished by the interaction (losing a significant proportion of its energy), the process is known as absorption.

The echo energy reflected from deeper structures will be weaker than that reflected from more superficial ones. This happens because the deeper the wave travels, the more energy is lost due to the scattering and absorption. Typically, the attenuation depends on the type of the tissue and is proportional to the frequency. Mathematically, attenuation can be defined as:

$$P = P_0 e^{-\alpha x},$$

$$\alpha = \alpha_0 f^n, \tag{1.11}$$

where x is acoustic path length in the attenuating medium, α_0 is a constant and n is the power of frequency dependence of α.

As seen from these equations, attenuation increases with increasing frequency, which limits the maximum frequency that can be used to scan the particular depth of tissue or region of body; the working frequency range is typically 1-5 MHz for scanning the abdomen, heart, or head, and 5-20 MHz for scanning the eyes. Thus, by limiting the maximum frequency, the attenuation also limits the range resolution indirectly. Since range resolution is important for image quality, it will be discussed in detail in Chapter 4 and Chapter 5.

1.2.5 Ultrasound techniques and classifications

The echo principle forms the basis of all common ultrasound techniques. The distance between the transducer and the reflector or scatterer in the tissue is measured by the time between the emission of a pulse and reception of its echo. Additionally, the intensity of the echo can be measured. Some definitions of ultrasonic echo display modes are [19]:

(1) A-mode: is the display of intensity (amplitude) information of signal from the receiver versus a time (distance). A-mode consists of an x and y axis, where x represents the distance and y represents the amplitude. This mode is rarely used today, as it conveys only 1D information and cannot display the shape of the scatterer.

(2) B-mode: is the most common technique for ultrasound imaging. It is obtained by physically moving the scan line to multiple adjacent locations and converts A-mode information into brightness-modulated dots. Therefore, B-mode will display an image composed of two-dimensional (2D) information. And those large and small dots represent strong and weak echoes, respectively.

(3) Motion mode (M-mode) [20]: uses B-mode information to display the echoes from a moving organ. This can be accomplished by recording the amplitude and rate of motion in real time by repeatedly measuring the distance of an object from a single transducer at a given moment. M-mode can be useful when imaging adult and fetal hearts.

(4) Doppler mode [21]: this mode uses the doppler effect to measure and visualize blood flow. In ultrasound, the doppler effect is associated with relative motions between the source of sound wave and the receiver, resulting in an apparent difference in frequency between that emitted by the source and that perceived by the receiver. In other words, an approaching wave is perceived to be emitting sound at a higher frequency than it actually is, while a retreating wave appears to emit at a lower frequency. Doppler mode is usually utilized in the clinical adjusting to evaluate and estimate blood flow in both the major and the minor vessels of the body.

(5) Harmonic mode [22]: on the basis of the non-linear properties of ultrasound, a deep penetrating fundamental frequency is emitted into the media and a harmonic component can be detected. In this way, the noises and artifacts caused by reverberation and aberration are greatly reduced. Some researchers also believe that harmonic imaging can improve spatial resolution compared to fundamental imaging at the original frequency. Thus, tissue harmonic imaging (THI) has become the default imaging mode for most abdominal imaging examinations.

(6) Three and four-dimensional mode [23]: nowadays, we use linear arrays to produce images. Three-dimensional (3D) mode requires methods to determine the position and orientation of the 2D images within the 3D image volume, as illustrated in Fig. 1.5. However, generating a four-dimensional (4D) mode (4D = 3D + real time), it is necessary to process the collected data at high speed, so that the real-time imaging presentation on the screen is possible. Currently, 3D and 4D modes have been developed and researched in two major ways. One is to overcome the limitations of 2D technique and allows the clinician to view the anatomy in 3D; the other is to provide better spatial guidance

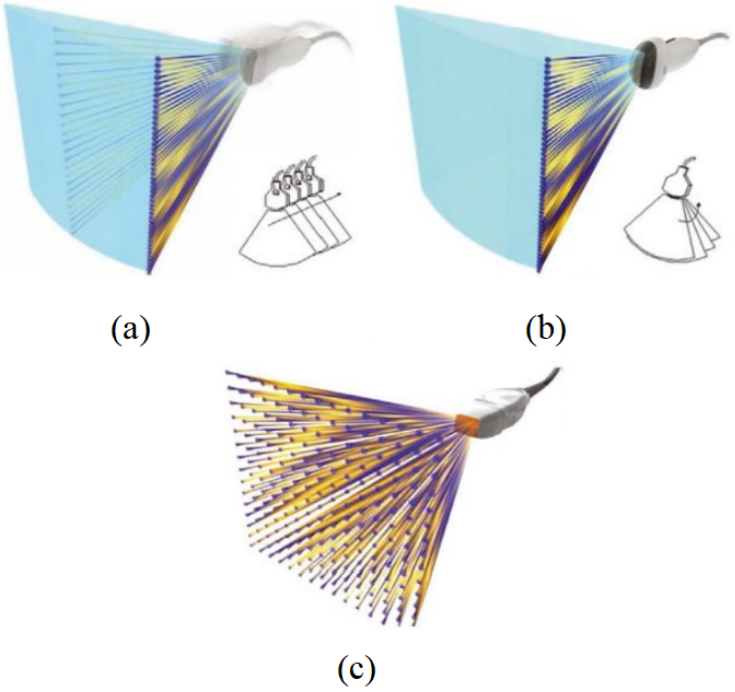

Figure 1.5: 3D scanning approaches: (a) free-hand scanning; (b) mechanical scanning with a fan type motor-driven mechanical transducer; (c) electronic scanning with a 2D matrix array transducer.

for various interventional procedures, such as biopsy, focal ablative therapy, and image-guided surgery.

1.3 Transducers

1.3.1 Piezoelectric effect

In most cases, the working principle for an ultrasonic transducer is based on a phenomenon called piezoelectric effect (see Fig. 1.6). The piezoelectric effect was first discovered by Jacques and Pierre Curie in 1880 [24]. This effect can be divided into direct piezoelectric effect and inverse piezoelectric effect. When a mechanical stress is applied to some certain materials, an electrical potential difference is generated across the material. This process is called the direct piezoelectric effect. Conversely, when an electrical energy across the material is applied to generate the mechanical stress. This process is called the inverse piezoelectric effect.

1.3.2 Piezoelectric materials

Some materials hold the piezoelectricity property naturally (see Table 1.2), such as single crystals. Additionally, certain ceramics, polymers and composites are also have piezoelectric property and can be used to design an ultrasound transducer. A typical piezoelectric material is lead zirconate titanate ($PbZrTiO_3$), called PZT [25]. The performances of transducers are strongly related to the piezoelectric materials. For instance, the strength of the electro-mechanical vibrations is dependent on the coupling factors, k_t for thickness mode and k_{33} for length-extensional mode. The acoustic impedance Z reflects the efficiency of energy transferred outwards from the piezoelectric layer, thus determining the matching and backing layers. Relative permittivity ε_{33}^{S} is useful in the design of electrical driving or receiving circuit of the transducer.

1.3.3 Transducer design

Ultrasound transducer is the core technology of ultrasound imaging. The major approaches to fabricate it include piezoelectric, magnetostrictive, electromagnetic, laser conversion and so on [26]. Among them, the most common transducer is made by the piezoelectric approach, which is based on the piezoelectric effect. This effect allows the transducer to convert electricity into mechanical waves in transmission, or convert the energy in mechanical waves into electricity at reception.

There are many different types of piezoelectric ultrasound transducers. The most common types are single-element, dual-element and array. The basic structure comes from the respective components. In a transducer stack, piezoelectric material is surrounded by matching layer and backing material for mechanical damping and absorbing residual

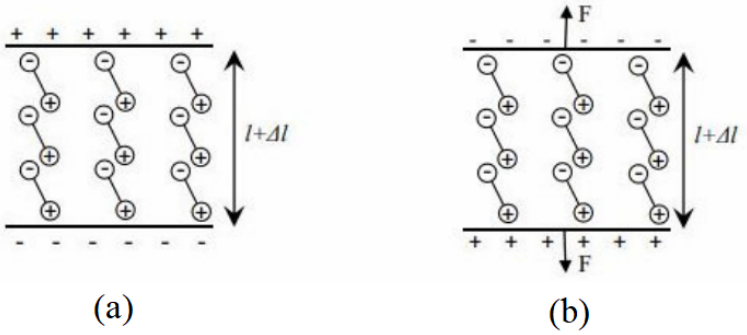

Figure 1.6: Piezoelectric effect: (a) inverse piezoelectric effect; (b) direct piezoelectric effect.

Table 1.2: Properties of piezoelectric materials commonly used in ultrasonic transducer

Material	PZT4	PZT5H	$PbNbO_3$	PVDF	$LiNbO_3$	AIN	PMN-PT
Thickness mode coupling coefficient k_t	0.47	0.52	0.33	0.19	0.16	0.24	0.57
Length-extensional coupling coefficient k_{33}	0.69	0.75	0.33	0.13	0.16	0.31	0.9
Piezoelectric strain constant d_{33} (pm/V)	290	590	85	25	5.9	5.5	1400
Piezoelectric voltage constant g_{33} (mV · m/N)	26	20	32	230	22	52	30
Longitudinal speed c (m/s)	4600	4800	3100	2200	7400	11400	4040
Acoustic impedence Z (MRayl)	35	34	19	3.9	34	37	32
Mechanical quality factor Q_m	High	Medium	Low	Low	Very high	Very high	Low
Relative permittivity at constant stress ε_{33}^T	1270	3430	300	8.4	29.8	12	3950
Relative permittivity at constant strain ε_{33}^S	640	1470	270	10-12	29	10.7	818
Curie temperature T_c (°C)	-350	-200	-400	-150	-1200	-1150	-90
Usual form	Bulk	Bulk	Bulk	Thin	Bulk	Thin	Bulk

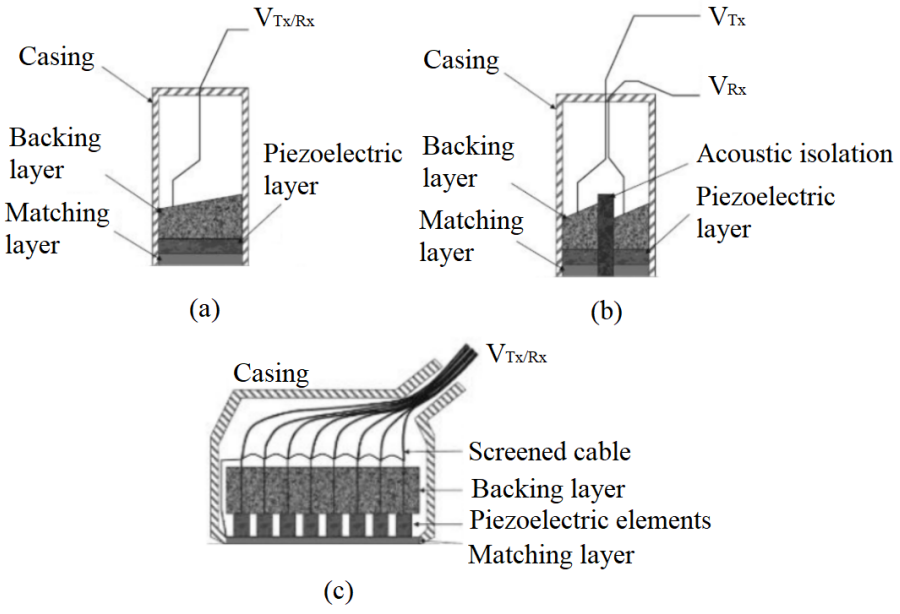

Figure 1.7: Details of piezoelectric ultrasound transducers: (a) single-element transducer; (b) dual-element transducer; (c) array transducer.

ultrasound energy that reverberates in the piezoelectric materials. Additional components include electric cable, electrical impedance matching, and physical casing. Details of different piezoelectric ultrasound transducers are described in Fig. 1.7.

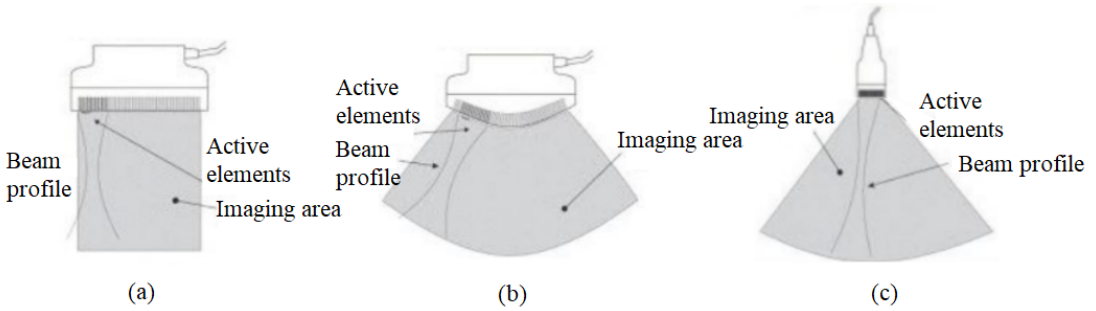

Figure 1.8: Typical electronic scanning with (a) linear array; (b) convex array; (c) phased array.

1.3.4 Transducer imaging

Today, array transducer is a ubiquitous transducer for ultrasonic imaging. The array transducer consists of an ensemble of arranged individual single transducers, or elements that can be controlled in groups or clusters to create pulse echo lines. Typically, array transducer can be divided into three main categories: linear, convex, and phased arrays. The array configuration also plays a major role in dynamic focusing and electronic beamforming. Fig. 1.8 illustrates the three configurations and the electronic scanning for each case.

1.4 Ultrasound Imaging Quality Factors

It is well known that the quality of an ultrasound image is very important, so an accurate representation of the image is necessary [27]. However, the image is subjected to a variety of distortions in various processes, from transmission to acquisition and back to reconstruction. Therefore, image quality is not a single factor, but a combination of many different factors, which depends on the characteristics of the equipment, the operators proficiency, reconstruction method and so on. The most common quality factors used in ultrasound image assessment will be discussed in the following subsections.

1.4.1 Signal to noise (SNR)

Noise is a random variation of image density. It arises from the effect of the propagation nature of wave and the thermal and electronic noise at the transducer. The SNR is the ratio of the reference target peak signal to the ultrasonic noise level. If the SNR is in a high level, it indicates that more useful information can be obtained compared to noise. Thus, in ultrasound imaging, the greater value of SNR is required [28].

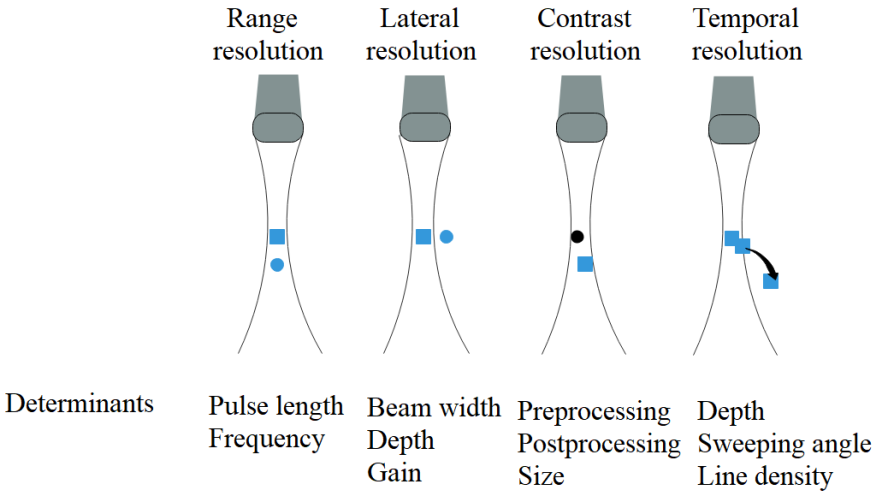

Figure 1.9: Concept of resolution.

1.4.2 Resolution

The resolution of ultrasound imaging can be simply defined in four categories:

(1) Axial resolution or range resolution: is the ability to distinguish between two objects lying in the direction of the propagation of the ultrasound beam. Axial resolution depends on the wavelength/frequency. Thus, the speed of the sound, the frequency and the physical length of pulses used to form the ultrasound beam are all related to it.

(2) Lateral resolution: is the ability to distinguish between two objects lying in the direction perpendicular to the ultrasound beam. Objects will only be resolved if the separation between them is greater than the beam width. Therefore, the thinner the beam, the better the lateral resolution.

As we can see in the Fig. 1.9, the lateral resolution can be optimized by using the dynamic focusing beamforming. Thence, the lateral resolution depends on the geometry of the transducer, the frequency, the focal distance and so on.

(3) Contrast resolution: refers to the minimum contrast that makes an object in the region of interest (ROI) more detectable than the background noise in an image. The loss of contrast resolution comes from acoustic clutter, mainly referring to side lobes and grating lobes. In particular, the side lobes results from a finite aperture size and the received signals out of the main beam, which seriously reduce the contrast resolution. Contrast resolution can be enhanced with various methods, such as compression and compounding techniques.

(4) Temporal resolution: is the time from the beginning of one frame to the next, and it refers to the ability of the ultrasound system to visualize moving objects. Temporal resolution is quantified by temporal bandwidth, and determined by frame rate and bandwidth of temporal filters. However, there is a trade-off in the relationship between the temporal resolution and its spatial resolution. Here, the spatial resolution is referred to both the axial resolution and lateral resolution.

1.4.3 Uniformity

Image uniformity is usually defined as the variation of the system's point spread function throughout the entire image. In a medical ultrasound system, it is defined as the equipment ability to give ultrasound echos with the same amplitude and deepness when the brightness is fixed. It is reasonable to expect brightness uniformity in ultrasound image. However, sometimes non-uniformity happens among scan lines (due to piezoelectric element failure) and horizontal bands (due to acoustic energy distribution over the field of view). Factors of image uniformity include depth of field, pulse shapes and variations due to lateral displacement.

1.4.4 Sensitivity

Sensitivity is an important parameter to describe the electro-acoustic energy conversion efficiency of ultrasonic transducer, which is defined in the context of the detection of weak signals. In principle, the frequency response function of a transducer is the spectrum of its sensitivity. For a given energy input, the greater the signal that is received from these scatterers, the higher the receiving sensitivity. Sensitivity is related to transducer design and system's dynamic range.

1.4.5 Penetration

Penetration is determined by ultrasonic power delivered to the scatterer on the transmitting side and the dynamic range of the system on the receiving side. At a higher penetration, the transducer needs to cover a longer distance (which is needed to lower the frequency), therefore the frame rate and the spatial resolution are not good enough. Conversely, to improve spatial resolution, one strategy is to increase the frequency accompanied by a loss of penetration.

Table 1.3: Useful and nonuseful artifacts

Useful artifacts	Distal acoustic enhancement	
	Acoustic shadowing	·dirty shadowing
		·clean shadowing
Nonuseful artifacts	Side or grating lobe artifact	
	Refraction artifact	
	Transmission speed errors	
	Mirror image artifact	
	Contact artifact	

1.4.6 Artifacts

Another important quality factor of ultrasound imaging is the identification of artifacts. In many situations, artifacts do not significantly influence the visibility and diagnostic accuracy of objects. But artifacts can obscure a part of an image or they may be interpreted as an anatomical feature. Various factors associated with each imaging method may cause image artifacts, such as the inherent errors of ultrasonic beam's characteristics, the existence of multiple echo paths, velocity errors, and attenuation errors.

Now that many of the common artifacts occurring in ultrasound images have been identified, but we still need to learn how to overcome or minimize them and to definitively recognize them as artifactual echoes rather than real echoes. Understanding the underlying physics of ultrasound and the assumptions used for ultrasound image formation is important for understanding ultrasound artifacts.

As an alternative, certain artifacts may offer useful diagnostic information in some certain respects. Acoustic shadowing can be very useful clinically, is often seen with calcifications, bone, and gas, and appears as clean or dirty shadowing. Clean shadowing as an example commonly occurs distal to larger calculi and bone and appears as a dark anechoic band. In this case, the presence of shadowing is critical for their recognition. Table 1.3 gives more insights into the useful and nonuseful artifacts.

1.5 Advantages and Disadvantages

Ultrasound imaging is widely used as an effective and intuitive method in medical diagnosis and non-destructive testing (NDT). In particular, ultrasound imaging plays an

Table 1.4: Comparison of imaging modalities

Modality	Ultrasound	X-ray	CT	MRI
Principle	Mechanical properties	Mean tissue absorption	Tissue absorption	Biochemistry
Resolution	Frequency dependent	1 mm	1 mm	1 mm
Penetration	Frequency dependent	Excellent	Excellent	Excellent
Safety	Very good	Ionizing radiation	Ionizing radiation	Very good
Speed	100 frames/s	Minutes	0.5-1 minute	10 frames/s
Cost	Less expensive	Less expensive	Expensive	Very expensive
Portability	Excellent	Good	Poor	Poor

important role in medical diagnosis due to its safety, little discomfort, inexpensiveness and speed compared with other medical imaging techniques. There is no ionizing radiation from ultrasounds, unlike an X-ray or computerized tomography (CT) scan, and no harm to the patient from the ultrasound scan has been reported. In addition, ultrasound images can be displayed in real-time much faster than magnetic resonance imaging (MRI), and provides valuable real-time diagnostic information to the surgeon. Furthermore, the instrument for an ultrasound system is relatively portable and less expensive than other instruments such as MRI, CT or X-ray scanners. All the features reviewed in this section are compared to the others popular medical imaging modalities in Table 1.4.

Despite these advantages, there are several disadvantages. First, ultrasound image generally has more speckles and less clarity than the CT and MRI image. Second, in terms of the mechanism of ultrasound scanning, a relatively larger wavelength will result in a comparatively less directional beam and weak focusing as well as higher sidelobes. This will distort the image and reduce the image quality since some artifacts which are not from the scanning area are displayed. In contrast, reducing the wavelength means increasing the center frequency of the transducer. This will decrease the SNR, since the attenuation of the medium is to some extent directly proportional to the transmission frequency. Thus, a compromise has to be found when performing ultrasound imaging improvement.

1.6 Motivations and Objectives

As stated above, the main limitation of ultrasound in medical applications is keeping a balance between spatial resolution and diagnosable depth. The spatial resolution along the range direction increases as the pulse width decreases. To attain high resolution, it is necessary to widen the frequency bandwidth of transmitting and receiving. Therefore, the resonance frequency of the transducer used to generate ultrasound must be high.

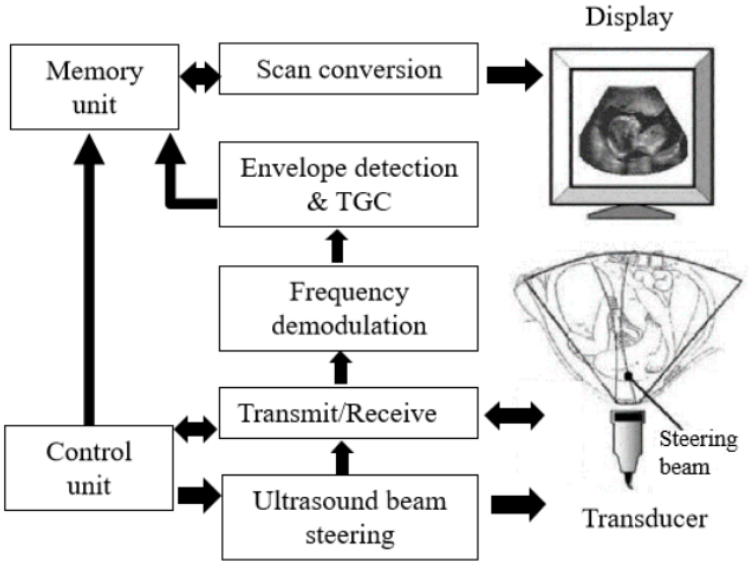

Figure 1.10: Schematic of medical ultrasound imaging.

However, the diagnosable depth decreases as the frequency increases, because there is less attenuation of ultrasound propagation when the frequency is low. To attain a large diagnosable depth, it is necessary to obtain a higher transmitting efficiency so that ultrasonic waves can propagate to deeper regions. Also higher receiving sensitivity is need to detect very small ultrasonic signals, which means the improvement of the SNR. Overall, it is difficult to accomplish the high spatial resolution and the large diagnosable depth simultaneously.

Increased ultrasound technology satisfied the growing medical needs and raised possiblities for new imaging solutions to medical problems. Fig. 1.10 shows a simplified schematic of medical ultrasound imaging. Advances in medical ultrasound imaging have been involving the combination of system architecture, transducer development, digital electronics, signal processing and display technology.

The purpose of this thesis is to improve the quality of ultrasound imaging. As every source of information comes from the transducer employed in the system. Therefore, the exploitation of transducer is necessary. Once the accuracy of the developed transducer has been assessed through experimental validation, the signal processing can be employed to improve the performance of ultrasound imaging display.

The specific objectives are outlined as follows:

1. Conduct some fundamental experiments to reveal the performance of a receiver called the PZT-FET.

2. Explore small scatterer-based restoration in ultrasound imaging.

3. Explore strong scatterer-based super-resolution in ultrasound imaging.

Chapter 2

Literature Review

2.1 Introduction

In this chapter, we will present an extensive survey of medical ultrasound improvements in literature, including the research of improvements in ultrasound imaging based on ultrasound transducer and signal processing.

2.2 Recent Improvements in Ultrasound Imaging Based on Ultrasonic Transducers

Ultrasonic transducers have two functions: transmission and reception. Depending on the system and its mission, there may be separate transducers for each function or there may be a single transducer for both functions. A transducer array may be used in either function.

Many researchers consider that the key to successful design of diagnostic and therapeutic ultrasound system is closely related to ultrasonic transducers properties. This is because the task for the ultrasonic transducers is not merely to detect ultrasound, as intelligent transducers, they should be efficiently extract the information carried by the ultrasonic signals with significance (accuracy, resolution, repeatability). Therefore, a summary of the development of recent transducers would help us judge its impact on the progress of medical ultrasound.

2.2.1 Basic ultrasound transducer

As mentioned above, the piezoelectric or crystal resonator was developed by the Curie brothers as early as 1880 [24]. Later, in 1894, Voigt et al. discovered that quartz crystal vibrating at resonance produces an electrical signal with a very precise, stable frequency. These characteristics were found to be suited for use in stabilization of transmitting and receiving signals [29]. Interestingly, B. Jaffe et al. [30] discovered PZT ceramics in 1954, which have better piezoelectricity than $BaTiO_3$ ceramics found in 1946 [31].

After that, there are so many explorations of novel piezoelectric materials for ultrasonic transducers [32], such as PZT-4, PZT-5H, polyvinylidene difluoride (PVDF) [33], aluminum nitride (AlN) [34], gallium nitride (GaN) [35] , zinc oxide (ZnO) [36], lithium niobate ($LiNbO_3$) [37], (1-x)$Pb(Mg_{1/3}Nb_{2/3})O_3$-$xPbTiO_3$ (PMN-PT) [38], $Pb(In_{1/2}Nb_{1/2})O_3$-PMN-PT (PIN-PMN-PT) [39], $K_{0.5}Na_{0.5}NbO_3$ (KNN) [40], $Bi_{1/2}Na_{1/2}TiO_3$(BNT) [41], $BiFeO_3$ (BFO) [42] and so on. All of those materials have received much attention in the past decade because some significant progresses in their physical properties, and great breakthroughs in the manufacture of ultrasonic transducers have been made.

The following literature reviews outline some of the major breakthroughs in the development of ultrasonic transducers in recent years.

Manufacturing piezoelectric materials for ultrasonic transducers needs high pressure and high temperature. In order to improve the temperature stability of piezoelectricity, H. J. Lee et al [43] and M. J. Zipparo et al [44] reported a piezoelectric composites structure that have improved thermal stability and mechanical quality factor.

To achieve a linear response to an alternating electric drive, those piezoelectric materials must be polarized. S. Saitoh et al [45] and C. Y. Park et al [46] proposed a design and fabrication of an ultrasound linear array transducer based on polarization inversion technique for increasing the center frequency and bandwidth of the transducer.

Harmonic imaging shows favorable potentials for high spatial and contrast resolution, and better delineation of borders and other structures compared to fundamental imaging. For the high sensitivity of different frequency ranges in harmonic imaging, many studies of transducers which can generate the fundamental frequency and the second-order harmonic frequency at the same time based on double peak type frequency characteristics have been reported [47–49]. Presently, J. Lee et al [50] reported a developed dual-element focused intravascular ultrasound (IVUS) [51] transducer for measuring third harmonic. In this case, multi-frequency array transducers are selected and have different center frequencies for transmission and reception.

Besides the piezoelectric deformation in the d_{33} mode [52], there are many other modes of ultrasonic transducer. A number of approximate methods have been employed to analyze the response of transducers using other models, and the related transducers have been fabricated. Such as d_{31} mode [53], d_{15} mode [54], d_{24} mode [55] and d_{36} mode [38, 56]. It should be noted that except the d_{33} and d_{31} mode, the other modes are used to generate shear waves.

Over the years, ultrasonic transducer technology has been mainly based on 1D line transducer arrays, because of the convenience of low cost and real-time operation. While extending to 1.25D [57], 1.5D [57, 58], 1.75D [59] and 2D [60, 61] transducer arrays have also been successfully addressed.

On the other hand, it is difficult to achieve full focusing capabilities in 1D linear or 2D array transducers at high frequencies. As a result, a number of researchers have explored annular array transducers [62, 63], which the beam focusing is done by addressing the inner rings with a time delay with respect to the outer rings.

2.2.2 FET-based ultrasound transducer

Electronics fabricated by using inner-crystal piezopotential as a "gate" voltage to tune or control the charge transport behavior is named piezotronics. Piezotronics concept was first introduced by Z. L. Wang group in 2006 [64, 65]. One common use of piezotronics is based on electrically gated field effect transistor (FET). By trial and error, many problems in traditional ultrasound transducers can be potentially overcome by FET-based ultrasound transducers. This type of transducer offers significant advantages in terms of high energy, high sensitivity and biocompatibility.

It is clear that, if the work function of the gate metal can be controlled by an external parameter, the piezotronics device is a direct sensor for this parameter. As ultrasonic transducers, the most nature choice is piezoelectricity. For this purpose, some materials, such as PZT, ZnO and GaN have been chosen[66, 67].

Fundamental understanding about this device is that the source and drain are located at the two ends of the device, and the gate voltage is applied to the channel and the substrate [68–70]. By applying a source to drain driving voltage, V_{DS}, the charge carrier transport process in the semiconductor device is tuned or gated by the gate voltage V_G, which is an externally applied potential. Alternatively, the gate voltage can be replaced by the piezopotential generated inside the crystal (inner potential), so that the charge carrier transport process in FET can be tuned or gated by applying pressure to the device [71].

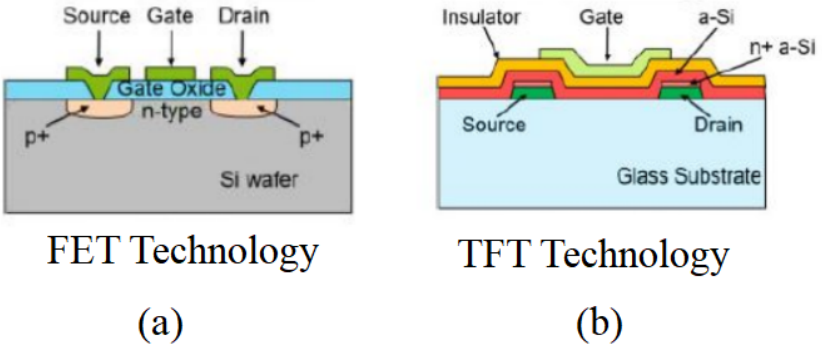

Figure 2.1: Cross section of (a) p-MOSFET; (b) amorphous silicon top-gate TFT.

Some related researches began early in 1980, P. Bergveld [72] discussed the development and application of FET-based biosensors, as well as a prediction with respect to future developments of FET-based biosensors. After that, ongoing efforts continue to develop this area. Today, monolithic integration of a FET in close proximity to piezoelectric materials has advantages for signal conditioning and processing due to the early conversion of the signal impedance into the low output impedance of the FET. It must be pointed out that the FET-based transducer is possible to excite and acquire the signals with high sensitivity. But honestly, the commercial manufacturing of reliable FET-based ultrasound transducer still has a long way to go.

2.2.3 TFT-based ultrasound transducer

Thin-film transistors (TFTs) can be seen as a class of FETs [73]. The main emphasis for TFTs is on large area and low temperature processing; Conversely, FETs are essentially focused on high performance at the cost of considerably larger processing temperature. Besides, FETs use a silicon wafer as a substrate; while TFTs use an insulator substrate, such as glass, which is not an active element for device operation (Fig. 2.1). Furthermore, the operation mode is also different between the FETs and the TFTs. The former is based on inversion, while the latter relies on accumulation. Table 2.1 lists the differences in the two technologies.

Flexible TFTs offer a new direction for innovative ultrasound transducers. Similarly, some materials such as PVDF [74], ZnO [75] and AlN [76] have been investigated with TFTs extensively. These materials are chosen for their electrical properties, particularly the electron mobility and the stability of the threshold voltage. Therefore, TFT-based ultrasound transducers can control transport of charge carriers, emission of wave and so on which also provide a solution for fully integrated flexible devices.

Table 2.1: Comparison of FET and TFT technology

	FET technology	TFT technology
Operation mode	Inversion	Accumulation
Layer growth technology	Implantation, deposition, growth from substrate	Deposition (sputtering, PECVD)
Process temperature	High temperature (> 600 °C)	Low temperature (< 600 °C)
Quality of layers	High crystalline quality of source and drain pockets and channel	Amorphous or polycrystalline
Carrier mobility in the channel($cm^2\ V^{-1}\ s^{-1}$)	500	0.5200
Type of substrate	Semiconductor substrates	Any kind of substrate, including glass
Substrate dimensions	Millimeter size	Centimeter to meter size

Before the publication of T. P. Brody's 1973 paper, very few publications has been reported on TFTs. In this paper, Brody first demonstrated a liquid crystal display (LCD) based on CdSe TFTs [77]. Then, the breakthrough in this field came from a report in 1979 of the first functional TFT made from hydrogenated amorphous silicon (a-Si:H) with a silicon nitride gate dielectric layer [78].

To comprehend the recent ultrasound transducer development of TFTs, S. Kim et al. described an electrostatic actuator based on a-Si:H TFT driver. The single actuator emits ultrasonic waves at 25 kHz and pressure of 27 dB sound pressure level (SPL), and a 1 $\times$ 2 array emits up to 34.6 dB SPL at 1cm distance [79].

To mention another interesting piece of research, organic TFT devices or circuits have been developed for purposes such as flexible sensors [80, 81], actuators [82] and in vivo medical diagnostics [83].

2.2.4 Micromachined ultrasound transducer (MUT)

With the development of micro electro mechanical systems (MEMS), micromachined ultrasound transducers (MUTs) have become a very promising alternative to replace traditional bulk ceramic transducers. Arrays with high element density, small element size and high resonant frequency are easy to realize through MUTs. Moreover, the MUTs array and external circuit can be integrated in a chip. MUTs work on either electrostatic or piezoelectric approaches, and they can be classified as capacitive MUTs (cMUTs) and piezoelectric MUTs (pMUTs). cMUTs based on flexural vibrations are caused by a field-induced electrostatic attraction between suspended membrane and the substrate (Fig. 2.2(a)); while pMUTs based on flexural vibrations are caused by d_{33} or d_{31} mode excitation of a piezoelectric membrane (Fig. 2.2(b)-(c)). In summary, the key comparisons between the two MUTs technologies are shown in Table 2.2.

Table 2.2: Comparison of the main differences between cMUT and pMUT

Comparison Parameters	cMUT	pMUT
DC bias	Yes	No
Frequency range	$>$ 200 kHz	$>$ 1 kHz
Bandwidth	High	Low
Electromechanical coupling	$>$ 50%	$\ll$ 50%
Fabrication techniques	Micromachined and wafer bonding	Micromachineds
IC integration	Easy	Difficult

In recent years, increasing attention has been paid to MUTs because of their advantages over conventional ultrasound transducers, such as miniaturization, low impedance, high bandwidth, high sensitivity, high electromechanical coupling coefficients, also with potential for automated large batch production and integration with front-end electronics.

O. Oralkan et al. fabricated a 128 × 128 element 2D cMUT array with a 420 μm element pitch [84]. As an experimental prototype, results demonstrated that 2D CMUT array could be fabricated with high yield using silicon IC-fabrication processes, individual electrical connections could be provided using through-wafer vias, and flip-chip bonding could be used to integrate these dense 2D arrays with electronic circuits for practical 3D imaging applications.

Dausch et al. reported the design and fabrication of 2D pMUT arrays [85]. They also described the vibrational modes for operation of flexure-mode pMUT elements, transmit output pressures, receive and pulse-echo characteristics, and B-mode imaging performance of the 81 element 2D arrays at a center frequency of 7.1 MHz [86].

Besides the above progress in MUTs, combination of MEMS technology with FETs or TFTs have certainly encouraged the innovation and development of ultrasound transducers [87, 88].

A zero-bias complementary metal oxide semiconductor (CMOS)-based cMUT was proposed in 2013, which is implemented based on TSMC 0.35 μm CMOS-MEMS 2P4M process [89]. The collapse voltage is lowered down to 150 V by scarifying the thinnest

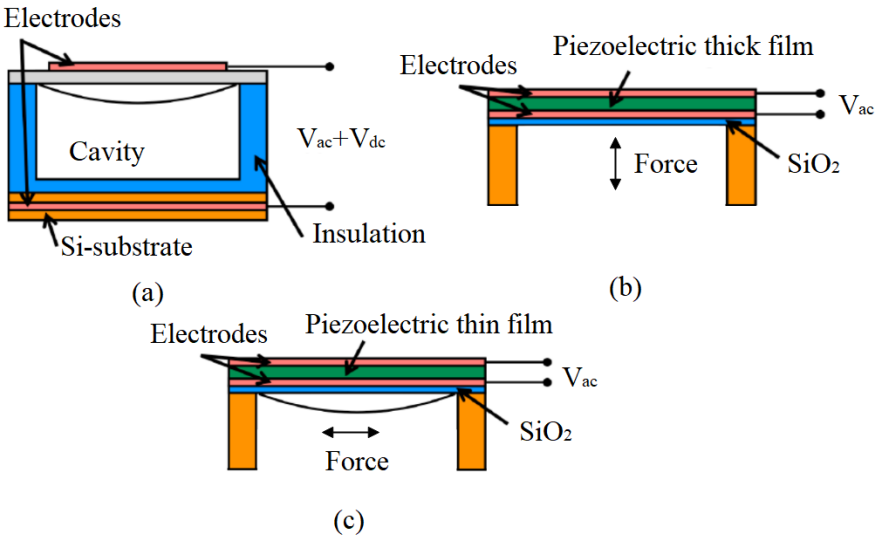

Figure 2.2: Micromachined ultrasound transducers: (a) cMUT; (b) d_{33} mode pMUT; (c) d_{31} mode pMUT.

layer (polysilicon) as a gap and sealing the device by depositing a thin film of parylene C. The receiving sensitivity is proved to be as high as the conventional operation with a DC bias. It is believed that the injection of charges on CMUTs due to the AC pulses can improve the sensitivity of the device.

Reger designed a pMUT-based ultrasonic imaging sensor which relies on post-CMOS monolithic integration rather than MEMS-to-CMOS wafer-to-wafer bonding. Device characterization demonstrated that a range of frequencies from 100kHz to 800 kHz with varying electrode coverage [90].

2.3 Recent Improvements in Ultrasound Imaging Based on Signal Processing

2.3.1 For small scatterer

The reflection and distribution of small scatterers in living tissue make the echo signals interfere with each other to generate speckle patterns, which causes the noisy nature of medical ultrasound images, and its presence in the image may obscure small structures, degrade the edge definition and limit the contrast resolution. Thus, various suppression methods have been proposed. At the same time, some other researchers are considering the speckle not as a noise term to be suppressed, but rather as a precious source of information.

The principles for analyzing the speckles are exploited in a wide range of applications as classification, segmentation, deconvolution and tracking. In this literature review, we will only address the major problems encountered in medical ultrasound tackling with statistically inspired approaches: the deconvolution related to our study.

Deconvolution in medical imaging is commonly employed for the purpose of visual quality improvement, which provides physicians with better contrast and resolved data for easier interpretation. As long as the improvement of image quality is concerned, deconvolution schemes exploit simple models for tissue reflectivity will be continue.

Deconvolution problem, or equivalently, restoration or deblurring problem, was first introduced by J. A. Jensen for ultrasound imaging [91, 92]. According to a convolution model, the radio-frequency (RF) image, obtained from the raw data after the beamforming operation, can be represented as a convolution between the point spread function (PSF) of ultrasound system and the tissue reflectivity function (TRF). Ultrasound imaging with limited spatial resolution can be improved by deconvolution.

Since 1990s, the deconvolution problem has been tackled in two ways. The first is carried out through estimating the PSF and TRF simultaneously, called blind deconvolution [93]. The second is to restore the TRF following the PSF estimate. This is called non-blind deconvolution [94, 95].

To solve the deconvolution problem, a number of methods have been employed, such as through the inverse filter, n-length least-squares deconvolution filter (Wiener filter) [96], weighted least squares (WLS) filter [97], minimum variance deconvolution (MVD) [98], Oldenburgs frequency domain deconvolution algorithm [99], l_1-norm deconvolution [100, 101], l_2-norm deconvolution, l_p-norm deconvolution, matching pursuit (MP) [102, 103], basis pursuit (BP) [104, 105], and some others [106, 107].

To briefly summarize the methods described above, we herein give the comparison presented in M. Alessandri PhD thesis [108], which is about the result of the Wiener and the l_1-norm deconvolution based on ultrasound imaging in vivo (see Fig. 2.3). The increased information associated with the Laplacian prior is evident, along with the oversmooting effect caused by Wiener deconvolution.

It is also clear that many classical models have been widely assumed for medical ultrasound restoration, such as Bayesian model [109–111], Gaussian model [112, 113], Rayleigh model [114], Laplacian model [112, 115], autoregressive (AR) model [116] and autoregressive moving average (ARMA) model [117, 118].

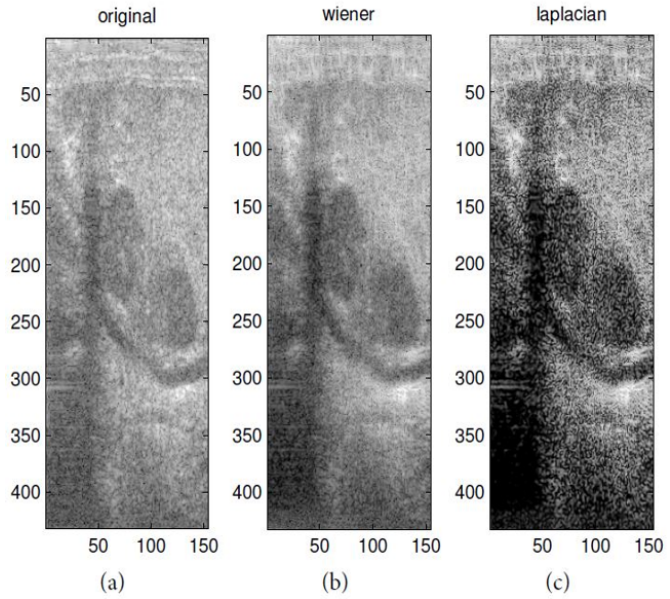

Figure 2.3: Results from a prostate ultrasound image: (a) observed B-mode image; (b) wiener deconvolution; (c) l_1-norm deconvolution.

After the landmark study by J. A. Jensen [91, 92, 95, 117, 118] at medical ultrasound restoration. N. Testoni [119] addressed an extensive dissertation on the employment of predictive deconvolution techniques and adaptive filters, which can be used for medical ultrasound restoration. And recently, S. Maggio et al. [116, 120] reported predictive deconvolution for the computer-aided detection of prostate cancer.

Deconvolution relies on the image restoration of an estimate of the true images. In fact, many existing researches in the medical ultrasound area [121–123] have shown its worth. The feasibility of deconvolution in our study is tackled by maximum a posteriori (MAP) estimate, in which tissue reflectivity is restored along with an estimate of the associated scale and shape parameter. An expectation maximization (EM) step is designed to address this task [124].

Overall, the preliminary investigation based on deconvolution of the microstructure and fundamental properties of small scatterers in living tissue is a major objective in our work, and also one of the most interesting and fruitful developing applications for medical ultrasound.

2.3.2 For strong scatterer

At present, the improvement on ultrasound imaging for strong scatterer can be achieved by numerous signal processing methods. However, in this literature review, we investigated the methods of strong scatterers based on beamforming for ultrasound imaging.

First, the most basic non-adaptive beamforming method is called delay-and-sum (DAS) [125]. Several other techniques such as coherence factor (CF) [126] and phase coherence factor (PCF) [127] can be combined with DAS to further reduce sidelobes, resulting in improved contrast of the beamformed image.

In reception, one idea of adaptive beamformings is to use the received echoes (raw channel data) to calculate the weights. The most widely used method is Capon method, also known as minimum variance (MV) method [128]. Capon beamforming applied to medical ultrasound imaging can improve lateral resolution and contrast. The original Capon method for ultrasound imaging is based on element-space (ES) signal processing [129–131]. ES signal processing requires the inversion of large matrices, which severely increases the complexity. To reduce the complexity associated with calculating the inverse matrices, beam-space (BS) Capon method has been reported [129, 132, 133]. This method uses a few orthogonal beams to reduce the matrix size.

Another class of adaptive beamformings has attracted significant interest, that is multiple signal classification (MUSIC) beamforming [134], which commonly relies on noise

subspaces, also konwn as orthogonal subspaces, for evaluation of imaging function. Result of such beamforming leads to satisfactory performance as long as signal subspace dimension does not occupy entire data space dimension. There are three common techniques to further improve the robustness of the MUSIC beamforming: TR-MUSIC [135], root-MUSIC [136] and unitary root-MUSIC [137].

Maximum likelihood (ML) beamforming is based on models containing parameters to be estimated and a variety of assumptions need to be taken into account [138, 139]. One possible assumption can be the shape of the signals, that can be modeled as deterministic or using statistical assumptions. The benefit of the ML beamforming is the ability to resolve coherent signals.

Compared to conventional DAS beamforming, delay multiply and sum (DMAS) beamforming utilizes multiplicative coupling of channel pairs for spatial coherence of receiving aperture to improve image resolution and contrast [140, 141]. However, present DMAS beamforming is based on the radio-frequency (RF) channel signals and thus requires large oversampling to avoid the corresponding spectral components for imaging. Baseband (BB)-DMAS in C. C. Shen study [142] has indicated that the proposed BB-DMAS requires less computational load and performs higher flexibility compared to RF-DMAS. Further researches have focused on the application of filtered-delay multiply and sum (F-DMAS) beamforming to high frame rate imaging [143, 144].

More recently, a new class of deconvolution algorithms has emerged and is called compressive sensing (CS) [145, 146], which can exploit the sparsity of RF signal. In contrast to classical inversion-based methods, these sparse deconvolution methods (SDMs) directly estimate the RF and provide significant resolution gains. However, SDMs generally assuming the ultrasound pulse is invariant throughout the propagation path. Although convenient, this assumption is not completely realistic in medical ultrasound due to the frequency dependent absorption and scattering. Therefore, echoes degrade severely compromises the performance of SDMs and leads to inaccurate estimations of the RF.

It is worth noting that numerical algorithms that are combined with each other have been developed. Proposed technique uses a modified DMAS + CF approach [147] to receive lateral resolution enhancement and sidelobes reduction. Similarly, MV + CF [148], MV + DMAS [149] and DAS + DMAS [150] have also been developed to improve ultrasound image quality.

The reconstructed images in M. Mozaffarzadeh study [149] using some mentioned beamformings are shown in Fig. 2.4. As can be seen, the reconstructed image using DAS contains high levels of sidelobe and artifacts, and the quality of reconstructed image

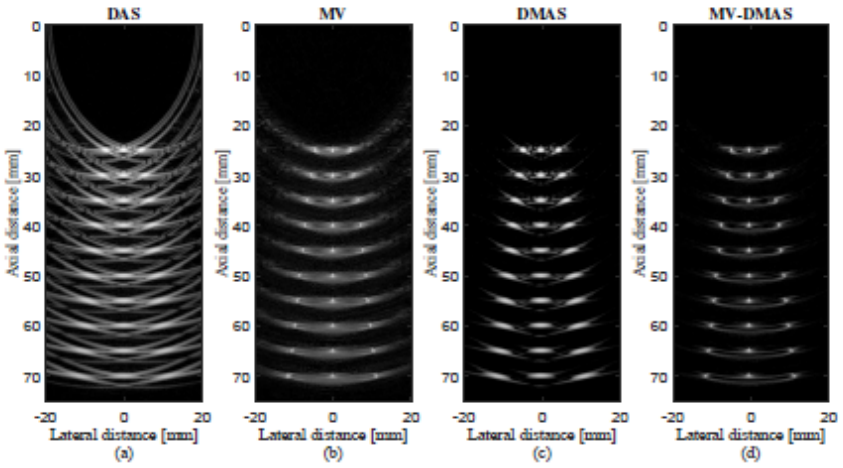

Figure 2.4: Simulated point targets using linear array. (a) DAS; (b) MV; (c) DMAS; (d) MV-DMAS. All images are shown with a dynamic range of 60 dB. 50 dB noise was added to detected signals.

is low. MV improves the quality of the reconstructed image in comparison with DAS. However, the levels of sidelobe are annoying and degrading the quality of image. The formed image using DMAS is shown in Fig. 2.4(c), and it can be seen that DMAS results in lower levels of sidelobe compared to DAS and MV. However, the resolution of point targets are still low. Using MV-DMAS as a beamforming algorithm leads to the low levels of sidelobe of DMAS and the high resolution of MV beamforming.

Chapter 3

Development and Measurement of FET-Based Ultrasound Receiver

3.1 Introduction

Over the past few decades, ultrasound imaging has been widely used in medical diagnosis and NDT. In these applications, it is very important to enhance image accuracy. High-frequency ultrasound waves (which have short wavelengths) generally generate images with high resolution and thus ultrasound reception performance must be improved to let high-sensitivity detection of very weak echoes in the high-frequency domain. In particular, the harmonics that are generated by nonlinear propagation of an ultrasound beam through a medium under test and its echo are effective for use in high-resolution imaging but the signals are very weak [151]. The high quality image based on those methods require the detection of weak signals. However, it is becoming increasingly difficult for traditional technology based on bulk ceramic transducers to simultaneously achieve the high resolution and large diagnosable depths required for these measurements, as the trade-off in the relationship between the spatial resolution and the diagnosable depth.

At present, researchers in various studies using novel piezoelectric materials in MUTs, which have demonstrated a certain increase in the reception sensitivity. In this study, we demonstrate a novel piezotronics device with an attempt to produce a much more sensitive ultrasound receiver. Piezotronics are those which consist of FET [152] and piezoelectric material for its gate layer. This is recently developed in a trend of smart device, for example, a sensor is directly coupled with a semiconductor to form a monolithic chip. Attributing to a property of mechanoelectric conversion of the piezomaterial, broad applications are known including sensors for humidity [153], pressure [154], acoustics [155], cantilevered- [156] and surface [157] forces.

Signal output against piezotronics responses is driven by direct charge injection into semiconductor to form a conductive channel by electric field effect, where source-drain current is observed depending on stress applied to the piezoelectric material. This principle eliminating use of long wiring between piezoelectric material and metal oxide transistor and of efficient charge usage output by piezoelectricity [158] results in improved SNR, sensitivity and dynamic range, when compared with a conventional piezoelectric transducer. Piezoelectric materials such as PZT crystals, PVDF, ZnO and AlN piezoelectric films have been investigated with FET extensively. However, few were found for the ultrasound receiving sensor in piezotronic device applications, particularly with measuring a sensitivity by minimum detectable sound pressure and frequency property. This might come from a difficulty in optimizing the device structure and its charge injection condition.

As a general tendency for measurable output of the piezotronic device, decrease of electric capacity of the piezomaterial is a considerable way for contribution of the efficient charge injection, the amount of which is to exceed that of parasitic capacity between the piezoelectric material and the FET gate linkage. For the first attempt to prototype for observing the piezotronic device characteristics for an ultrasonic use, we have designed a piezoelectric gated FET structure in which a bulk PZT body is connected directly on the gate of a MOSFET, called PZT-FET. This paper reports the frequency properties through the FET output conducted by simply thickening the piezoelectric structure of a certain area. The specific structural fabrication of PZT-FET will be briefly depicted in the next section.

3.2 PZT-FET Design

In most cases, the basic working principle of an ultrasound transducer for reception is that PZT crystal functions piezoelectric effect to convert either random or generated vibrations that are present in the environment into usable amounts of electrical energy that can then be detected by a receiving circuitry. Therefore, in this study, we demonstrate the first piezoelectric FET fabricated using a bulk PZT element for ultrasonic receiver.

The proposed PZT-FET device is depicted in Fig. 3.1, which consists of a FET with a piezo-body combined on the gate of the FET. To take advantages of the piezoelectric phenomena, bulk PZT element [159] was selected. Since it not only has a good driving capability and piezoelectric characteristics that can inject sufficient charge to drive the FET, but also it has very high resistivity, which prevents leakage of the charges in the gate metal layer. The FET used here is a commercially available N-MOSFET having a

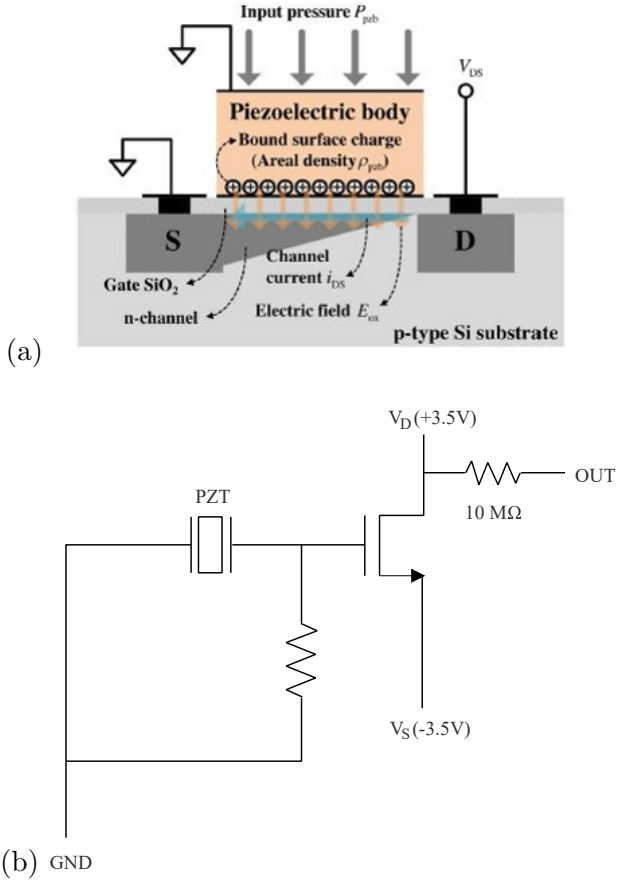

Figure 3.1: Structure of the PZT-FET structure. (a) schematic diagram; (b) its equivalent circuit.

N-channel region between source and drain, and the substrate is P-type. The PZT-FET was prepared by wiring the anode of a 40-μm-thick PZT to the gate of the N-MOSFET. To realize the proposed design as shown in Fig. 3.1(a), the size and the dielectric constant of the PZT that are critical to the observation with a certain property, were tuned to optimal values of $8 \times 40 \times 0.04mm^3$ and 800, respectively. In addition, Fig. 3.1(b) shows the quivalent circuit model of the PZT-FET, which suggests that the effective output of the PZT-FET was recorded in the form of its drain voltage, and was determined via current-voltage (I-V) conversion of the source-drain current using a 10 MΩ resistor.

3.3 Device Operating

Fig. 3.2 shows the working principle of the proposed PZT-FET mechanism. As we can see, in response to a change in applied pressure, the change in the bound surface charge density at the piezo-body directly results in a change in the vertical electric field at the gate oxide, which modulates the channel and hence the source-drain current that flows

with a given source-drain bias applied in the FET. As a result, the device will going through the accumulation, depletion and inversion. The typical capacitance-pressure (C-P) response curve of the PZT-FET is shown in Fig. 3.2(b), and the dotted curve indicates low frequency whereas the black curve illustrates the high-frequency.

On the basis of the early observations, we confirmed the operation of the device, and found that the equivalence of the pressure to the voltage applied to the gate was indicative of the formation of accumulation, depletion and inversion layers between the source and drain with increasing pressure. Therfore, such a novel PZT-gated FET design provides the potential for high performance ultrasonic transducer systems with high sensitivity and high frequency. This is because the device can theoretically amplify electrical signals, and it is easy to measure weak signals. However, even if the operating characteristics of the PZT-FET are well known, the ability of the device to operate as a sensor and obtain an output that is dependent on the sound pressure when an ultrasound wave is received at the gate is not yet known. Therefore, we need to specifically analyze the performance of the PZT-FET based on ultrasonic experiments.

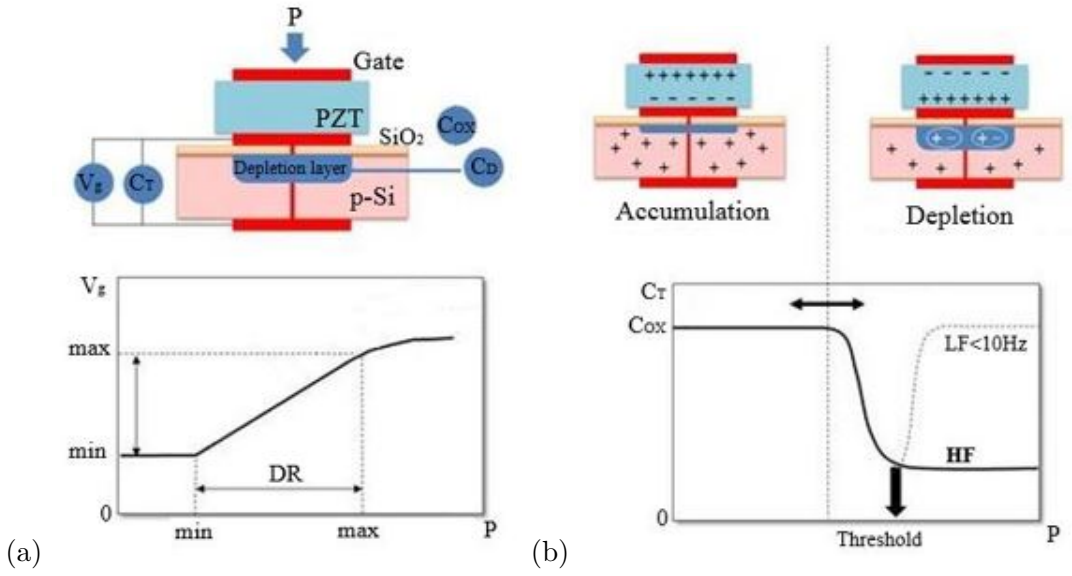

Figure 3.2: Working principle of the proposed PZT-FET mechanism. (a) voltage-pressure characteristics; (b) capacitance-pressure characteristics at low and high frequencies.

3.4 Device Characteristics

3.4.1 Evaluation method

In this study, the performance of the PZT-FET as a receiver was further evaluated in terms of the following three aspects and compared with those aspects of a conventional PZT-based ultrasound receiver:

- Minimum detectable sound pressure (MDSP) [160]

The minimum detectable sound pressure defines pressure detection threshold at which the received signal corresponding to the pressure can be distinguished from the electrical noise level. This can be used as an index for evaluation of the sensitivity. The recently published sensitivities of pressure sensors are represented in Table 3.1. The minimum detectable sound pressure for a typical ultrasound transducer is approximately 2000 Pa. In this study, we are aiming to achieve a high sensitivity that is similar to or greater than the values listed in Table 3.1.

- Dynamic range (DR) [161]

The DR is a representation of the ratio of the maximum and minimum values of the signals that the device can sense and the DR is evaluated in decibels, as follows:

$$\mathrm{DR\,(dB)} = 20\log_{10}\frac{\mathrm{V_{max}(detectable\,signal)}}{\mathrm{V_{min}(detectable\,signal)}} \tag{3.1}$$

- -6 dB specific bandwidth [162]

The -6 dB specific bandwidth represents ratio of the device's bandwidth to its center frequency. This index is used to evaluate the device's wideband characteristics. Naturally, wideband characteristics are preferable for an imaging with high spatial resolution. Therefore, the specific bandwidth refers to a high-performance device. The specific bandwidth of a typical ultrasound transducer is approximately 60%. The -6 dB specific bandwidth can be described as follows:

$$\mathrm{Specific\,Bandwidth(\%)} = \frac{\mathrm{Bandwidth}}{\mathrm{Center\,frequency}} \tag{3.2}$$

Table 3.1: MDSP values from recent studies of pressure sensors

Principle	**MDSP**
Ring resonator [163]	590 Pa
Piezoelectric micromachined ultrasound transducer [164]	116 Pa
Polymer ferroelectret actuators based on TFT [74]	2 Pa
Piezoelectric FET based on a ZnO nanowire [64]	17nN

3.4.2 Experimental setup

As a first step in the experimental procedure, using a calibrated hydrophone with 13 nV/Pa sensitivity (HGL0085, ONDA Corp., California, USA; see Fig. 3.3(b)) as a receiver, the output voltage characteristics in water were measured for each frequency of

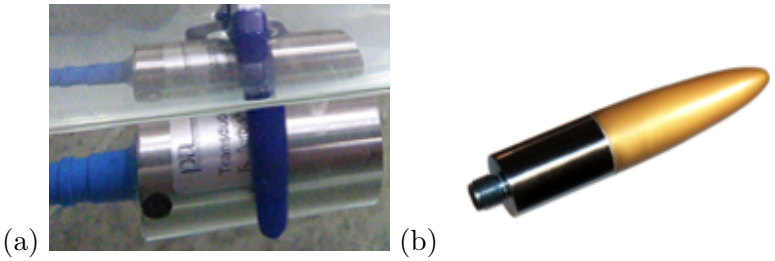

(a) (b)

Figure 3.3: Images of: (a) the 15 MHz transmitting transducer used in the sensitivity test; (b) the hydrophone.

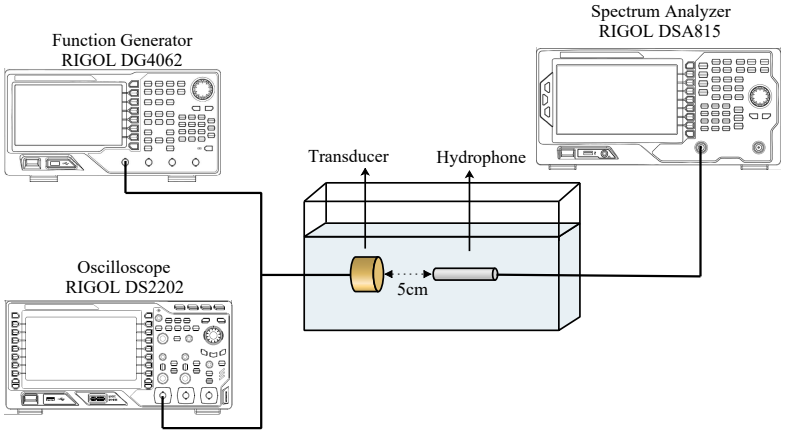

Figure 3.4: Experimental setup used for the transmitter calibration.

the transmitter (PA250, Precision Acoustics Ltd., Dorchester, UK; see Fig. 3.3(a)) using the setup shown in Fig. 3.4. The resonant frequency of the transmitter was 15 MHz, and the transmitted voltage was measured by using an oscilloscope and regulated to maintain at a constant level over the observation frequency range by tuning excitation voltages. The distance between the hydrophone and the transmitter was 5 cm. Continuous ultrasound waves were emitted by the transmitter at frequencies ranging from 1 MHz to 20 MHz.

Fig. 3.5 shows the frequency characteristics of the transmitter that were measured at a transmitted voltage of 10 V. The sound pressure was then obtained by dividing the output voltage of the ultrasound wave received at the spectrum analyzer by the sensitivity

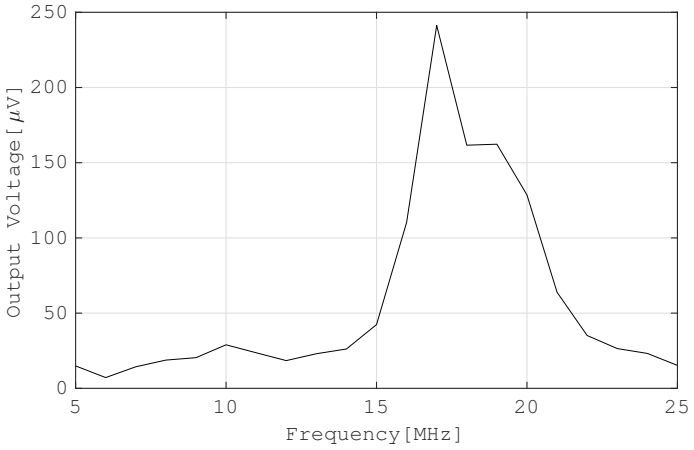

Figure 3.5: Frequency spectrum of the transmitter.

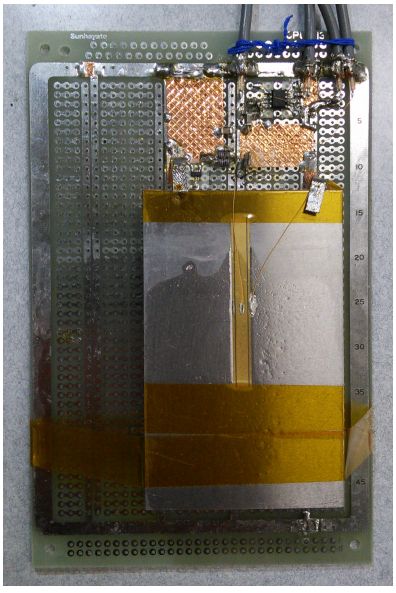

Figure 3.6: PZT-FET prototype device.

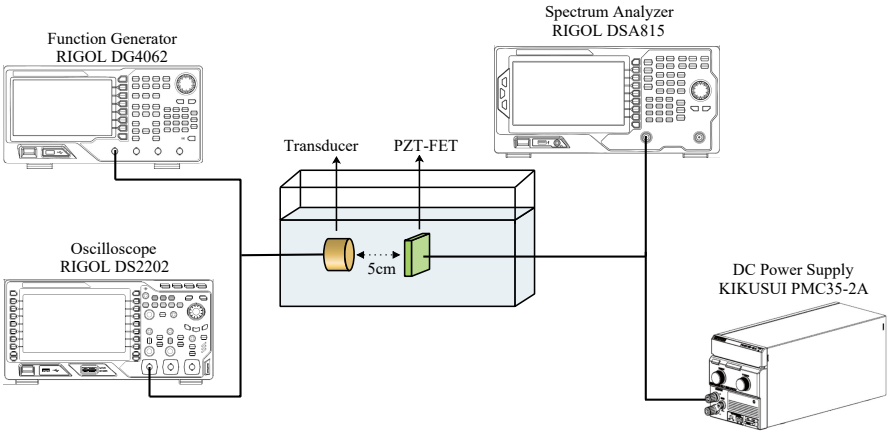

Figure 3.7: Experimental setup used for measurement of the PZT-FET.

of the hydrophone.

Subsequently, the hydrophone was replaced by the PZT-FET (see Fig. 3.6). and the reception properties of the PZT-FET were observed in water using the same transmitter. The observation conditions were exactly the same as those used in the previous experiment, except for ±3 V biasing (source: PMC 35-2A, Kikusui Electronics Corp., Kanagawa, Japan) to the PZT-FET, as shown in Fig. 3.7. The output voltage of the PZT-FET was determined via I-V conversion of the source-drain current using a 10 MΩ resistor, which was recorded by the spectrum analyzer.

3.4.3 Results and discussion

Fig. 3.8(a) shows the linearity of the receiver outputs with respect to the transmitted acoustic pressure over the observation frequency. These linear proportions ranged widely particularly from very low initial level. The dynamic range defining the minimum and maximum detectable sound pressures are 8 Pa and 11000 Pa, respectively, from Fig. 3.8(b) and (c). Fig. 3.9 shows the output voltage of the PZT-FET in response to swept frequencies in the range 10-20 MHz. We found that the resonant frequency of PZT-FET is almost 14 MHz when the pressure at 1000 Pa. Based on those results, the receiving performance of the PZT-FET was characterized in terms of the minimum detectable sound pressure, the linear dynamic range and the -6 dB specific bandwidth, which were observed to be 8 Pa, 63 dB and 20%, respectively. Because the minimum detectable pressure was 8 Pa, which was very difficult to measure using a conventional PZT transducer, this relatively enhanced performance indicated the excellence of the PZT-FET. Furthermore, the dynamic range of the device has been greatly improved when compared with that of a conventional device, having increased from normally 40

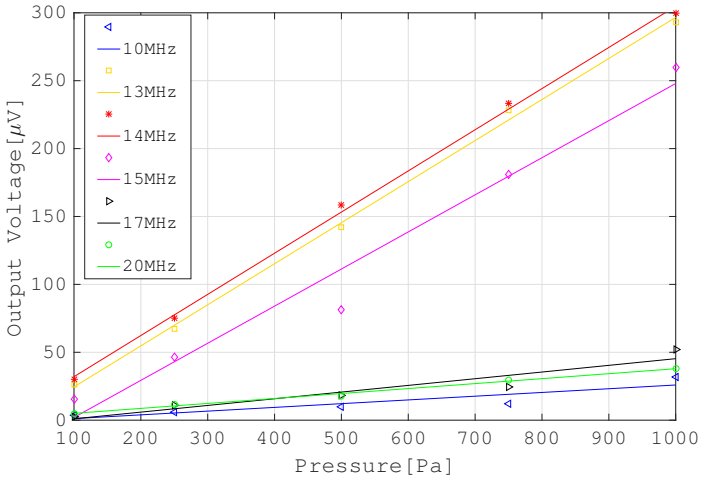

(a)

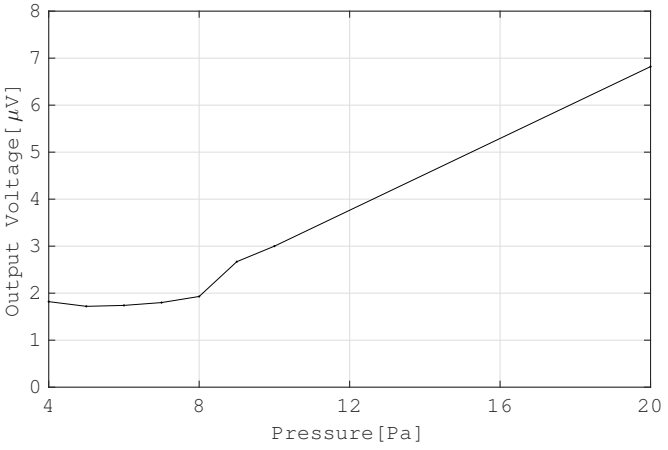

(b)

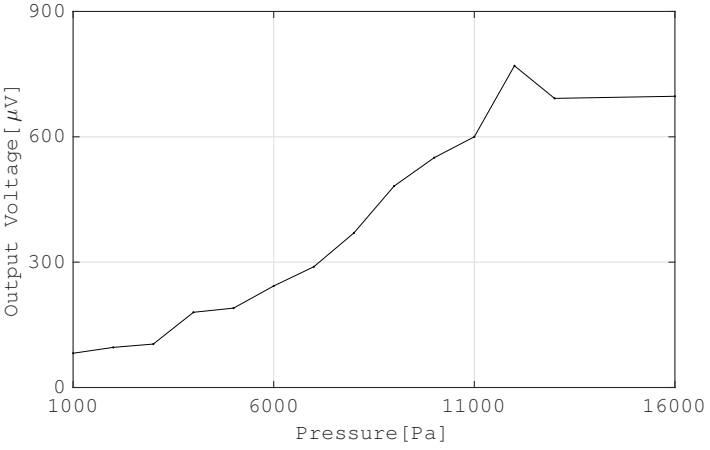

(c)

Figure 3.8: PZT-FET output vs. acoustic pressure input. (a) whole range with different frequencies (100-1000 Pa); (b) low pressure range at 14 MHz (4-20 Pa); (c) elevated pressure range at 14 MHz (1000-17000 Pa).

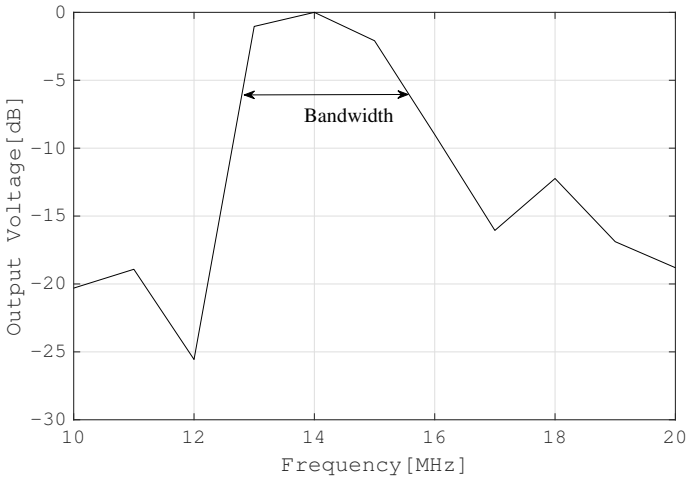

Figure 3.9: Frequency dependence of the PZT-FET output observed from an input acoustic pressure of 1000 Pa.

dB to 63 dB. These findings are attributed to the sensitivity of the linearly varying piezoelectric charges and the channel conductivity.

However, the specific bandwidth remains low because of the dominance of the PZT resonance at the quarter-wave ($1/4\lambda$) resonance frequency, f_R (14 MHz) reflecting a vibration characteristics of bulk thickness mode prone to show single frequency. Thus, as a potential solution, it may be possible to expand the receiver characteristics and provide further improvements using a relaxer with higher piezoelectric properties than the PZT.

Another possible solution to increase device performance is to design an array containing a number of PZT-FET MUTs, and each array has a different f_R. A unit of the PZT-FET MUTs is shown in Fig 3.10, the structure having a square diaphragm as the gate of the PZT-FET was simulated and the f_R was measured at approximately 20 MHz. The reason for using the square shape is that it can lengthen source and drain electrodes, and the width-to-length ratio (in addition to the PZT parameters) is also related to the device sensitivity. Furthermore, in the MEMS-type processing [165] [166], it was assumed that a thin diaphragm was used rather than a bulk PZT element. In particular, PZT-FET MUTs with f_R values ranging from 10 MHz to 30 MHz can be obtained by a simple control of the diaphragms dimensions.

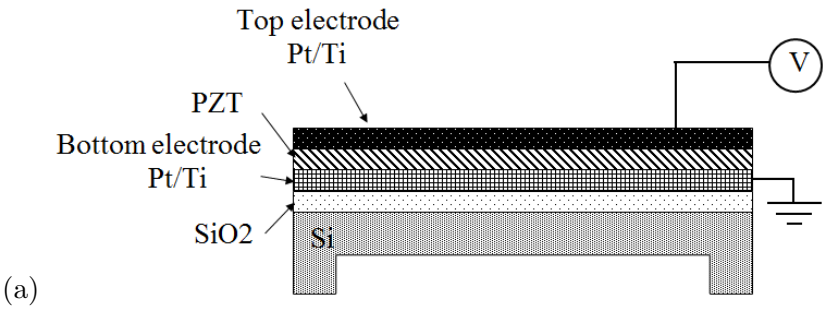

(a)

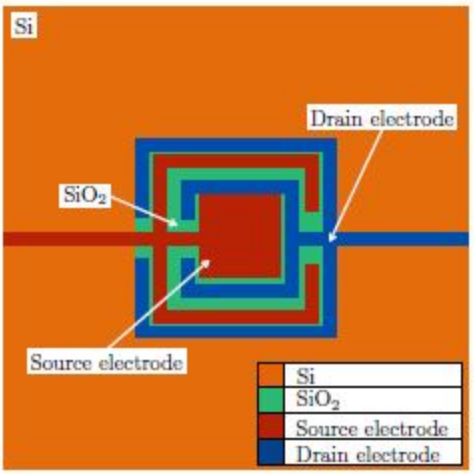

(b)

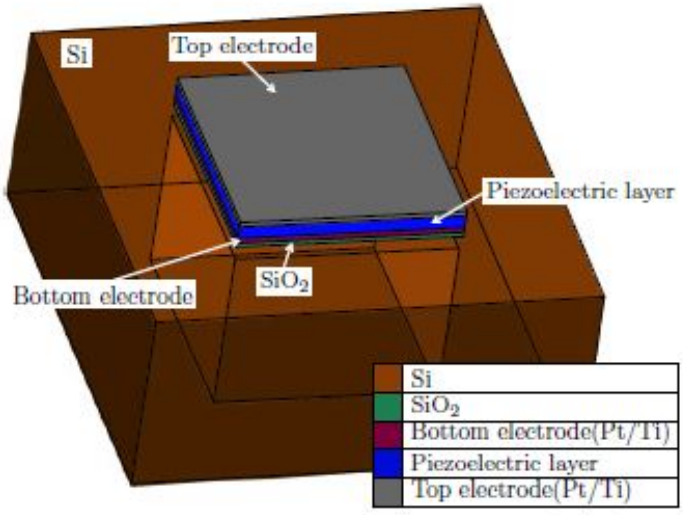

(c)

Figure 3.10: Structure having square diaphragm as a unit of the PZT-FET MUTs: (a) PZT-FET MUT model; (b) unique electrode structure; (c) epitaxial structure and configuration.

3.5 Conclusions

In this study, the PZT-FET receiver was proposed and fabricated for the first time, and the reception characteristics of the device were analyzed in detail. The experimental results demonstrated that an almost linear relationship between the input pressure and output voltage was found at a large region, which demonstrates the PZT-FET is suitable for making the ultrasonic receiver. Furthermore, the PZT-FET provided excellent ultrasound reception characteristics with high sensitivity and high dynamic range with an expectedly narrow specific band width. It is promising to use this device to obtain very weak echoes at high frequencies, which demonstrates potential applications to high frequency ultrasound and harmonic ultrasound. Besides the results described above, we also consider further device improvements attained by micromachining, one of the ideas is to fabricate the PZT-FET MUTs array transducers. In future work, we will apply the techniques proposed in this study to develop a much improved device, which is expected to lead to high-performance ultrasonic transducer systems, as well as system-on-chip functionality.

Chapter 4

Small Scatterer-Based Empirical Bayesian Estimation Applied to Echo Signals

4.1 Introduction

In ultrasound medical imaging, it is important that the boundaries and edges of organs, blood vessels and tumors are detected [167–169]. In addition, the reflection and distribution of small scatterers in living tissue has important information for diagnosing tissue properties. If the bandwidth of the transmitted pulse is sufficiently wide, that is, if very sharp pulses can be transmitted, high resolution imaging can be carried out and thus, the distribution of the scatterers producing echoes can be measured exactly. However, in actual imaging, typical ultrasonic transducers have a narrow band of characteristics. Furthermore, in order to clearly obtain echoes, the transmitted pulse contains several cycles of sin waves. As a result, the reflectance distribution is convoluted with the transmitted signal, and the echo whose resolution is greatly reduced is reflected toward the transducer. These echo signals interfere with each other to generate speckle patterns, which making the measurement of scatterer distribution difficult.

The speckle patterns are often used efficiently for medical diagnosis based on physician experience, which results in subjective interpretation and inter-observer variability. These are also effective for tissue motion analysis using image processing. On the other hand, since the speckle patterns hinder the detection of small tumors, various suppression methods have been proposed [170–172]. Recently, studies on reducing speckle observation by actively imaging a small number of strong echo sources attract attention, which are based on CS or sparse modeling techniques [173–175]. In this strategy, only

the echo intensity is taken into account while the speckle characteristics are ignored. Contrary to those facts, in this study, we aim at estimating the reflection distribution of scatterers, which is the source of the speckle pattern, from echoes. If small scatterers can be accurately restored from the echoes, by subtracting the corresponding echoes from the entire echo, the images consisting only of sparse scatterers with strong reflection, i.e., contours of organs, blood vessels, tumors can be obtained by, for example, our super-resolution imaging method [176]. Namely, by separately processing small scatterers and large scatterers, both can be separately imaged, which leads to high resolution imaging.

This scatterers restoration must be treated as an ill-posed problem, because echoes occur through convolution process. It is impossible to uniquely restore the distribution of the scatterer from only the observed information, and observation noise is also likely to influence the solution. In order to solve these problems, it is necessary to (i) increase observation information and (ii) apply appropriate assumptions and constraints to the solution. The former can be realized, for example, by using harmonic echoes in addition to fundamental echoes. For the measurement of harmonic echoes, we proposed techniques to improve SNR [177] and compensate for distortion caused by frequency dependent attenuation (FDA) [178]. In this study, focusing on the latter, we consider the reflection distribution of small scatterers as a stochastic sequence arranged in the range direction, and we model it with AR process usually used in random signal processing. The parameters of the AR model show correlations inherent in the reflection distribution, which are expected to parametrize the tissue properties. The ill-posed characteristics in this restoration problem are very strong when compared with blurred image restoration, because the frequency band that cannot be observed so wide. Therefore, it is necessary to investigate the estimation possibility and accuracy of both the AR parameters and the reflection distribution itself. To realize it, we can apply the algorithm constructed in the time domain based on empirical Bayesian method [179, 180]. After that, we considering recovery the reflection distribution in the frequency domain. As a first step of our future efforts, in this study we evaluate the performance through numerical simulation using data correctly fitted to the assumed model.

4.2 Problem Definition

Since the echo depends not only on the reflection of the scatterer but also on the transmittance and the diffraction, it is difficult to formulate the echo generation process considering all these properties. In this study, we define the equivalent reflectance that generates echo by convolution with the transmitted pulse.

An N-dimensional vector $\boldsymbol{y}$ is defined as an observed RF echo signal, in which N corresponds to the number of time-sampling. We assume that $\boldsymbol{y}$ contains an additive white normal random numbers $\boldsymbol{n}$ with zero mean and variance σ_n^2 as observation noise. By using the N-dimensional vector $\boldsymbol{h}$ as the above mentioned equivalent reflectance, $\boldsymbol{y}$ can be formulated as follows:

$$\boldsymbol{y} = \boldsymbol{W}\boldsymbol{h} + \boldsymbol{n}, \tag{4.1}$$

where $\boldsymbol{W}$ is an $N \times N$ matrix representing convolution with the transmission pulse. As the width of the transmission pulse increases, the rank of $\boldsymbol{W}$ approaches zero. Therefore, we can simply restore $\boldsymbol{h}$ using $\boldsymbol{W}^+$ which is a pseudo-inverse of $\boldsymbol{W}$.

$$\hat{\boldsymbol{h}} = \boldsymbol{W}^+\boldsymbol{y}. \tag{4.2}$$

However, the solution is sensitive to the noise contained in $\boldsymbol{y}$, and furthermore, the information contained in $\boldsymbol{h}$ discarded by $\boldsymbol{W}$ can not be restored. Instead, by applying the AR model to $\boldsymbol{h}$ we consider the method to recover such discarded information by extrapolation.

The AR model is a general stochastic representation of random time series with correlation between components. Using i to indicate the order of the components, and $\boldsymbol{h}$ is defined using the white normal noise ϵ_i with variance σ_h^2, as follows:

$$h_i = \sum_{j=1}^{P} a_j h_{i-j} + \epsilon_i, \tag{4.3}$$

Here, $\boldsymbol{a} \equiv \{a_1, a_2, ..., a_P\}$ is called the AR coefficient, and P is the order of the AR model and indicates the number of past components explicitly affecting the current component. The matrix and vector representation of Eq. 4.3 is listed as follows:

$$\boldsymbol{A}\boldsymbol{h} = \boldsymbol{\epsilon}. \tag{4.4}$$

For example, when $P = 2$, the matrix $\boldsymbol{A}$ is written as

$$\boldsymbol{A} = \begin{pmatrix} 1 & 0 & 0 & 0 & \cdots \\ -a_1 & 1 & 0 & 0 & \cdots \\ -a_2 & -a_1 & 1 & 0 & \cdots \\ 0 & -a_2 & -a_1 & 1 & \cdots \\ \vdots & \vdots & \vdots & \vdots & \ddots \end{pmatrix}. \tag{4.5}$$

From Eq. 4.4, $\boldsymbol{h}$ is a sample from the following multi-dimensional normal distribution.

$$p(\boldsymbol{h}|\boldsymbol{a},\sigma_h^2) = \frac{1}{\sqrt{(2\pi\sigma_h^2)^N \det(\boldsymbol{A}^\top\boldsymbol{A})^{-1}}} \exp\left(-\frac{\boldsymbol{h}^\top\boldsymbol{A}^\top\boldsymbol{A}\boldsymbol{h}}{2\sigma_h^2}\right). \tag{4.6}$$

We can know that the mean of $\boldsymbol{h}$ is $\boldsymbol{0}$ and the variance-covariance matrix is $\boldsymbol{V}_h = \sigma_h^2(\boldsymbol{A}^\top\boldsymbol{A})^{-1}$.

4.3 Method in Time Domain

4.3.1 Estimation method based on empirical Bayes

Considering that $\boldsymbol{y}$ contains observation noise, we aim at recovering $\boldsymbol{h}$ in the time domain. From Eq. 4.1, the probabilistic density of $\boldsymbol{y}$ under the condition that $\boldsymbol{h}$ is given forms the following normal distribution.

$$p(\boldsymbol{y}|\boldsymbol{h},\sigma_n^2) = \frac{1}{\sqrt{(2\pi\sigma_n^2)^N}} \exp\left[-\frac{(\boldsymbol{y}-\boldsymbol{W}\boldsymbol{h})^\top(\boldsymbol{y}-\boldsymbol{W}\boldsymbol{h})}{2\sigma_n^2}\right]. \tag{4.7}$$

The joint probability of $\boldsymbol{y}$ and $\boldsymbol{h}$ is derived using Eqs. 4.6 and 4.7 as follows:

$$p(\boldsymbol{y},\boldsymbol{h}|\boldsymbol{a},\sigma_n^2,\sigma_h^2) = \frac{\exp\left[-\frac{(\boldsymbol{y}-\boldsymbol{W}\boldsymbol{h})^\top(\boldsymbol{y}-\boldsymbol{W}\boldsymbol{h})}{2\sigma_n^2} - \frac{\boldsymbol{h}^\top\boldsymbol{A}^\top\boldsymbol{A}\boldsymbol{h}}{2\sigma_h^2}\right]}{(2\pi)^N\sqrt{\sigma_n^{2N}\sigma_h^{2N}\det(\boldsymbol{A}^\top\boldsymbol{A})^{-1}}}. \tag{4.8}$$

In general, $\{\sigma_n^2,\sigma_h^2,\boldsymbol{a}\}$ is estimated as the maximum likelihood estimator (MLE) using the probabilistic density of $\boldsymbol{y}$ obtained by marginalizing Eq. 4.8 with respect to $\boldsymbol{h}$.

$$\begin{aligned} p(\boldsymbol{y}|\boldsymbol{a},\sigma_n^2,\sigma_h^2) &= \int p(\boldsymbol{y},\boldsymbol{h}|\boldsymbol{a},\sigma_n^2,\sigma_h^2)d\boldsymbol{h} \\ &= \frac{1}{\sqrt{(2\pi)^N\det\boldsymbol{\Lambda}}} \exp\left(-\frac{\boldsymbol{y}^\top\boldsymbol{\Lambda}^{-1}\boldsymbol{y}}{2}\right), \end{aligned} \tag{4.9}$$

$$\boldsymbol{\Lambda} = \sigma_h^2\boldsymbol{W}(\boldsymbol{A}^\top\boldsymbol{A})^{-1}\boldsymbol{W}^\top + \sigma_n^2\boldsymbol{I}. \tag{4.10}$$

Assigning the observed value of $\boldsymbol{y}$ to Eq. 4.9 and considering it as a function of the parameters, Eq. 4.9 is called a likelihood function, and its logarithm is a log-likelihood function. The value that maximizes the likelihood function, and hence the value that maximizes the log-likelihood function, is the ML estimate. Using the ML estimate of $\{\sigma_n^2,\sigma_h^2,\boldsymbol{a}\}$, $\boldsymbol{h}$ can be determined as the maximum a posteriori (MAP) estimator $\hat{\boldsymbol{h}}_{MAP}$

, which maximizes the posteriori probability of $\boldsymbol{h}$ as follows:

$$\begin{aligned} p(\boldsymbol{h}|\boldsymbol{y},\boldsymbol{a},\sigma_n^2,\sigma_h^2) &= \frac{p(\boldsymbol{y}|\boldsymbol{h},\sigma_n^2)p(\boldsymbol{h}|\boldsymbol{a},\sigma_h^2)}{p(\boldsymbol{y}|\boldsymbol{a},\sigma_n^2,\sigma_h^2)} \\ &\propto \exp\left[-\frac{1}{2}\left(\boldsymbol{h}-\hat{\boldsymbol{h}}_{MAP}\right)^\top \boldsymbol{V}_{h|y}^{-1}\left(\boldsymbol{h}-\hat{\boldsymbol{h}}_{MAP}\right)\right], \end{aligned} \tag{4.11}$$

$$\hat{\boldsymbol{h}}_{MAP} = \left(\frac{\boldsymbol{W}^\top\boldsymbol{W}}{\sigma_n^2}+\frac{\boldsymbol{A}^\top\boldsymbol{A}}{\sigma_h^2}\right)^{-1}\frac{\boldsymbol{W}^\top\boldsymbol{y}}{\sigma_n^2}, \tag{4.12}$$

$$\boldsymbol{V}_{h|y} = \left(\frac{\boldsymbol{W}^\top\boldsymbol{W}}{\sigma_n^2}+\frac{\boldsymbol{A}^\top\boldsymbol{A}}{\sigma_h^2}\right)^{-1}. \tag{4.13}$$

We can use $\hat{\boldsymbol{h}}_{MAP}$ as the recovery result of $\boldsymbol{h}$ by using the ML estimate $\{\hat{\sigma}_n^2,\hat{\sigma}_h^2,\hat{\boldsymbol{a}}\}$ as the values of the parameters in Eq. 4.12. Thus, the scheme of Bayesian estimation using the parameters estimated based on marginal likelihood is called empirical Bayesian method.

4.3.2 Algorithm implementation by EM scheme

The MLE based on Eq. 4.9 generally requires iterative calculations, and each calculation is a little complicated. Instead, we can use an EM algorithm where the MLE of the parameter and the MAP estimator of the latent variable are alternately updated by iterative calculation. In the EM algorithm, observation and latent variables are collectively referred to as complete data. The EM algorithm is effectively executed against the problem that the MLE of the parameter is easy when complete data is observed. Eq. 4.8 corresponds to the probability of complete data, and the log-likelihood function of complete data is formulated from Eq. 4.8 as follows:

$$\begin{aligned} &\ln L_c(\sigma_n^2,\sigma_h^2,\boldsymbol{a}) \\ &= \text{Const.} - \frac{N\ln\sigma_n^2}{2} - \frac{N\ln\sigma_h^2}{2} - \frac{\ln\det(\boldsymbol{A}^\top\boldsymbol{A})^{-1}}{2} \\ &\quad -\frac{(\boldsymbol{y}-\boldsymbol{W}\boldsymbol{h})^\top(\boldsymbol{y}-\boldsymbol{W}\boldsymbol{h})}{2\sigma_n^2} - \frac{\boldsymbol{h}^\top\boldsymbol{A}^\top\boldsymbol{A}\boldsymbol{h}}{2\sigma_h^2}. \end{aligned} \tag{4.14}$$

The following E-step and M-step are repeated until convergence.

In the E-step, we derive the expectation of Eq. 4.14 with respect to the posteriori probability of $\boldsymbol{h}$, $p(\boldsymbol{h}|\boldsymbol{y},\hat{\sigma_n^2}^{(p)},\hat{\sigma_h^2}^{(p)},\hat{\boldsymbol{a}}^{(p)})$, where $\hat{\boldsymbol{\Theta}}^{(p)} \equiv (\hat{\sigma_n^2}^{(p)},\hat{\sigma_h^2}^{(p)},\hat{\boldsymbol{a}}^{(p)})$ is the estimate determined at the pth iteration. As a result, this expectation of Eq. 4.14, called the Q

function, can be derived as follows:

$$
\begin{aligned}
&Q(\boldsymbol{\Theta}|\hat{\boldsymbol{\Theta}}^{(p)}) \\
&\quad = \text{Const.} - \frac{N\ln\sigma_n^2}{2} - \frac{N\ln\sigma_h^2}{2} - \frac{\ln\det(\boldsymbol{A}^\top\boldsymbol{A})^{-1}}{2} \\
&\quad - \frac{\boldsymbol{y}^\top\boldsymbol{y} + 2\boldsymbol{y}^\top\boldsymbol{W}\hat{\boldsymbol{h}}^{(p)} + \text{trace}\boldsymbol{W}\hat{\boldsymbol{V}}_h^{(p)}\boldsymbol{W}^\top}{2\sigma_n^2} \\
&\quad - \frac{\text{trace}\boldsymbol{A}^\top\boldsymbol{A}\hat{\boldsymbol{V}}_h^{(p)}}{2\sigma_h^2},
\end{aligned} \tag{4.15}
$$

$$
\hat{\boldsymbol{h}}^{(p)} = \left(\frac{\boldsymbol{W}^\top\boldsymbol{W}}{\hat{\sigma_n^2}^{(p)}} + \frac{\hat{\boldsymbol{A}}^{(p)\top}\hat{\boldsymbol{A}}^{(p)}}{\hat{\sigma_h^2}^{(p)}}\right)^{-1}\frac{\boldsymbol{W}^\top\boldsymbol{y}}{\hat{\sigma_n^2}^{(p)}}, \tag{4.16}
$$

$$
\hat{\boldsymbol{V}}_h^{(p)} = \hat{\boldsymbol{h}}^{(p)}\hat{\boldsymbol{h}}^{(p)\top} + \left(\frac{\boldsymbol{W}^\top\boldsymbol{W}}{\hat{\sigma_n^2}^{(p)}} + \frac{\hat{\boldsymbol{A}}^{(p)\top}\hat{\boldsymbol{A}}^{(p)}}{\hat{\sigma_h^2}^{(p)}}\right)^{-1}. \tag{4.17}
$$

In the M-step, $\hat{\boldsymbol{\Theta}}$ is updated so as to maximize the Q function derived as Eq. 4.15 with respect to $\boldsymbol{\Theta}$. For $\boldsymbol{a}$, we need to maximize the 4th and 6th terms on the right side of Eq. 4.15. When the number of observation is sufficiently large, since the 6th term is $O(N)$, the 4th term can be neglected when compared with the 6th term. Therefore, in this study, we update $\hat{\boldsymbol{a}}$ to satisfy the following equation.

$$
\text{trace}\frac{\partial(\boldsymbol{A}^\top\boldsymbol{A})}{\partial\boldsymbol{a}}\hat{\boldsymbol{V}}_h^{(p)} = \boldsymbol{0}. \tag{4.18}
$$

Both variances are updated as follows:

$$
\hat{\sigma_n^2}^{(p+1)} = \frac{\boldsymbol{y}^\top\boldsymbol{y} + 2\boldsymbol{y}^\top\boldsymbol{W}\hat{\boldsymbol{h}}^{(p)} + \text{trace}\boldsymbol{W}\hat{\boldsymbol{V}}_h^{(p)}\boldsymbol{W}^\top}{N}, \tag{4.19}
$$

$$
\hat{\sigma_h^2}^{(p+1)} = \frac{\text{trace}\hat{\boldsymbol{A}}^{(p+1)\top}\hat{\boldsymbol{A}}^{(p+1)}\hat{\boldsymbol{V}}_h^{(p)}}{N}. \tag{4.20}
$$

The above two steps are repeated and the update is stopped when the change of $\hat{\boldsymbol{\Theta}}$ becomes sufficiently small. $\hat{\boldsymbol{\Theta}}^{(p)}$ obtained when converging corresponds to the MLE, and also $\hat{\boldsymbol{h}}^{(p)}$ is the MAP estimator.

4.4 Method in Frequency Domain

Considering that observed values in this problem correspond to the convolution of unknown parameters, we can also recover $\boldsymbol{h}$ in the frequency domain. In the frequency

domain, we can rewrite Eq. 4.1 as:

$$Y_i^F = W_i^F H_i^F + N_i^F. \tag{4.21}$$

Here, if W_i^F is sufficiently large, we can solve $\boldsymbol{h}$ as

$$\hat{H}_i^F = Y_i^F / W_i^F. \tag{4.22}$$

But if W_i^F is sufficiently small, we cannot solve $\boldsymbol{h}$ by Eq. 4.22, which means that if only a part of the frequency band of the scatterer reflectance distribution is observed, we need to apply the AR model in the frequency band, and further consider a way to estimate the AR parameters.

The power spectrum density (PSD) $P(f)$ of the AR model, which is the expectation value of the square of frequency component can theoretically be formulated as follows:

$$P(f) = \frac{\sigma_h^2}{|1 - \sum_{i=1}^{P} a_i e^{-j2\pi f i}|^2}. \tag{4.23}$$

Note that Eq. 4.22 multiplied by its complex conjugate, we can calculate the value of the power spectrum, then average for multiple observation sequences to obtain the power spectrum density $\hat{P}_i$. However, $\hat{P}_i$ here is raised by the level of observation noise with variance σ_n^2.

Thus, evaluation function J after logarithmic transformation can be defined as:

$$J \equiv \Sigma\{ln\hat{P}_i - lnP(f_i)\}^2 = \Sigma\{ln\hat{P}_i - ln\sigma_h^2 - ln|1 - \sum_{i=1}^{P} a_i e^{-j2\pi f i}|^2\}^2. \tag{4.24}$$

We can minimize this evaluation function with $\boldsymbol{a}$ and σ_h^2. Now that it cannot be solved theoretically, this time we use an iterative method to alternately update $\boldsymbol{a}$ and σ_h^2 in the direction of the steepest descent [181]. Therefore, the estimated overall values $\{\hat{\sigma}_n^2, \hat{\sigma}_h^2, \hat{\boldsymbol{a}}\}$ are obtained, and $\boldsymbol{h}$ can be recovered by Eq. 4.12 using these parameters.

4.5 Numerical Evaluation for Time Domain Method

4.5.1 Evaluation method

Numerical performance evaluation of our method was done using ideal data satisfying Eq. 4.1. As the number of cycles included in the transmission pulse increases, the observed frequency band decreases, and it becomes difficult to estimate the AR parameters and hence, to recover $\boldsymbol{h}$. Impulse, 1 cycle of 5 MHz and 5 cycles of 5 MHz were used as the transmission pulse. Of the above, two 5 MHz pulses were apodized by the Gaussian window function. Observing the echo generated by impulse transmission, it is expected that $\boldsymbol{h}$ can be almost completely restored. This is because the entire frequency band can be observed. Observation data $\boldsymbol{y}$ was prepared by the following procedure.

1. We set $\boldsymbol{a}$ and σ_h^2, and use these to generate $\boldsymbol{h}$ as AR time series.
2. $\boldsymbol{h}$ is convoluted with the transmission pulse selected from the above three, and the result corresponds to $\boldsymbol{y}$ with no noise.
3. We set σ_n^2 and use it to generate Gaussian noise. This noise is added to $\boldsymbol{y}$ generated above to obtain observation data.

Transducer characteristics, beam focusing and propagation attenuation were ignored and data exactly matched to the evaluation model were used for evaluation.

Performance evaluation that depends on the order of AR model and AR coefficient will be a subject for the future, and we set the order to 2 and fixed the parameters $\boldsymbol{a} = \{0.6, 0.3\}$ and $\sigma_h^2 = 0.02$. In that case, each value of generated $\boldsymbol{h}$ remained almost in the range of ± 1. We also set the noise variance $\sigma_n^2 = 0.02$, and the peak amplitude of the transmission pulse was normalized to 1.0. Under this condition, the standard deviation of noise was 2.5% of the standard deviation of $\boldsymbol{y}$ when transmitting a pulse consisting of one cycle, and 1.2% when transmitting a pulse consisting of 5 cycles. Since it is assumeed that the observation noise is electric noise, we can suppose that σ_n^2 is known in advance with no practical problems.

4.5.2 Results

In this study, 10 time series of echo consisting of 1000 sampling values were used. The time sampling rate is about 100 points per 5 MHz sinusoidal cycle common to all processing. For all trials performed, we confirmed that the EM algorithm had almost converged by 500 iterative updates, therefore we adopt $\hat{\boldsymbol{h}}^{(500)}$ as an estimation result and simply

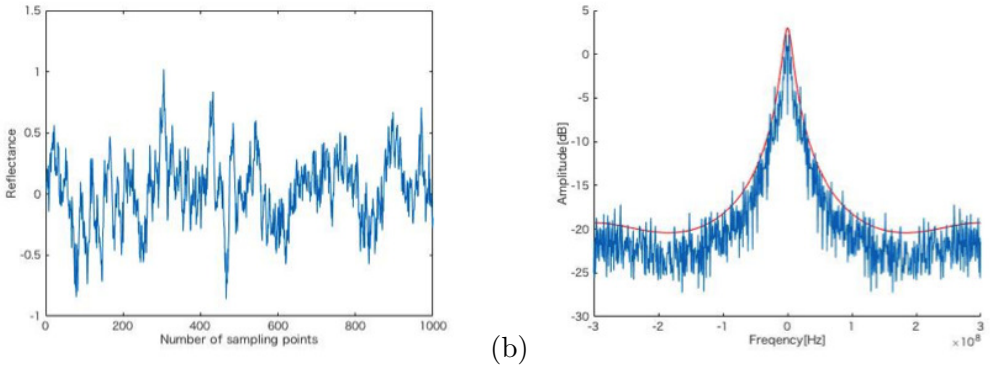

(a) (b)

Figure 4.1: One series of $\boldsymbol{h}$ consisting of 1,000 samples for time domain method is shown in (a), and its power spectrum is shown in (b). The red curve in (b) indicates the theoretical power spectrum of the set AR model.

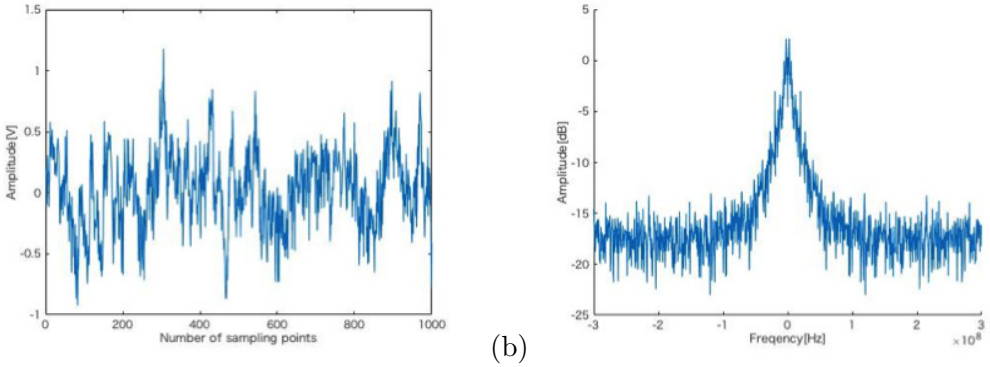

(a) (b)

Figure 4.2: The echo $\boldsymbol{y}$ generated by convolving the impulse with $\boldsymbol{h}$ and adding observation noise is shown in (a) and its PSD is shown in (b).

write it as $\hat{\boldsymbol{h}}$. An example of the setting value of $\boldsymbol{h}$ to be recovered is shown in Fig. 4.1. Instead of ensemble average, the power spectrum in Fig. 4.1(b) was calculated by taking the average value of 10 series of $\boldsymbol{h}$. PSD of the AR model can be formulated as Eq. 4.23 and the theoretical value corresponding to the assumed AR model is shown in Fig. 4.1(b) as a red curve.

First, we attempted to restore $\hat{\boldsymbol{h}}$ when the transmission pulse is impulse. In this case, almost all frequencies are observed, and only observation noise hinders estimation. Fig. 4.2 shows the echo signal $\boldsymbol{y}$ and its power spectrum. Since the observation noise exists, the level of high frequency components in Fig. 4.2(b) rise compared to the power spectrum of $\boldsymbol{h}$ in Fig. 4.1(b). The $\hat{\boldsymbol{h}}$ corresponding to Fig. 4.1(a) is indicated by a red line in Fig. 4.3(a), and its power spectrum is also shown in Fig. 4.3(b), in which the red curve and the green curve show respectively the theoretical values of the set AR model and the theoretical values of the estimated AR model, both of which are approximately equal. Estimated AR parameters are $\hat{\boldsymbol{a}} = \{0.618, 0.278\}$ and $\hat{\sigma_h^2} = 0.0198$. From this result, it

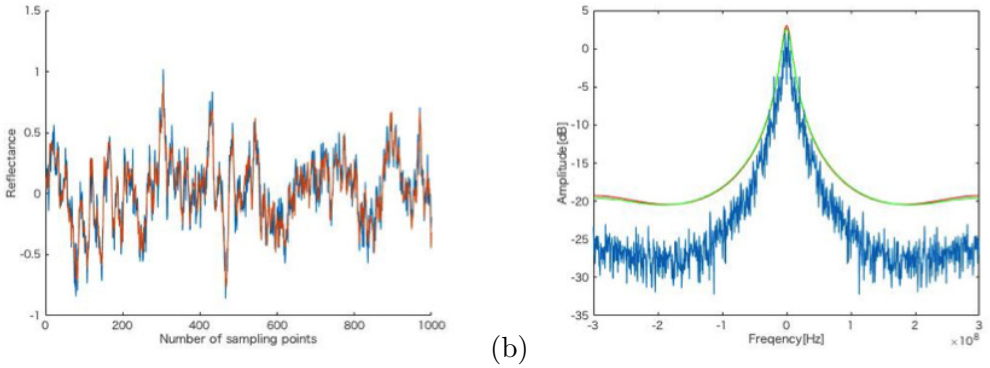

(a) (b)

Figure 4.3: $\hat{\boldsymbol{h}}$ restored for impulse transmission is indicated by red line in (a) and blue line is set value. The PSD of the restored result (red line) in (a) is shown in (b) using blue curve, the red curve corresponds to the theoretical value of the set AR model, and the green curve corresponds to the theoretical value of the estimated AR model.

can be seen that the AR model can be estimated with extremely high accuracy. Regarding the recovery of $\boldsymbol{h}$, it is difficult to obtain the white noise component in principle, and in the high frequency band in Fig. 4.3(b), the restoration error appears conspicuously.

Next, we estimated the AR parameters and restore $\boldsymbol{h}$ from the echo generated by one cycle pulse transmission. Fig. 4.4 presents one cycle pulse in time and frequency domain. As in Fig. 4.2, $\boldsymbol{y}$ and its PSD are shown in Fig. 4.5. Comparing Fig. 4.2 and Fig. 4.5, it can be seen that one cycle pulse transmission restricts the observable frequency band to a low range. The restored $\hat{\boldsymbol{h}}$ is shown in Fig. 4.6, and the estimated parameters are $\hat{\boldsymbol{a}} = \{0.589, 0.313\}$ and $\hat{\sigma_h^2} = 0.0185$, and the estimation error is slightly larger than that of impulse transmission. Although it can be easily predicted that the restoration problem from very limited observation is a difficult task, AR model can be estimated with high accuracy. The reason for this is presumed to be that the local frequency component has sufficient information to restore the AR model as extrapolation. This

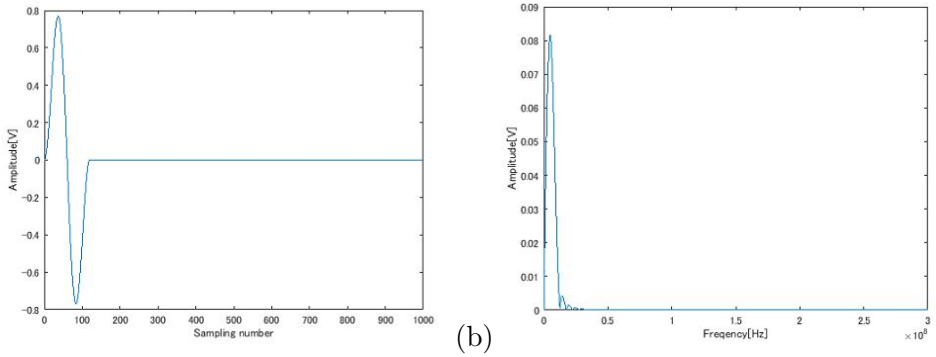

(a) (b)

Figure 4.4: One cycle pulse: (a) time waveform; (b) frequency domain.

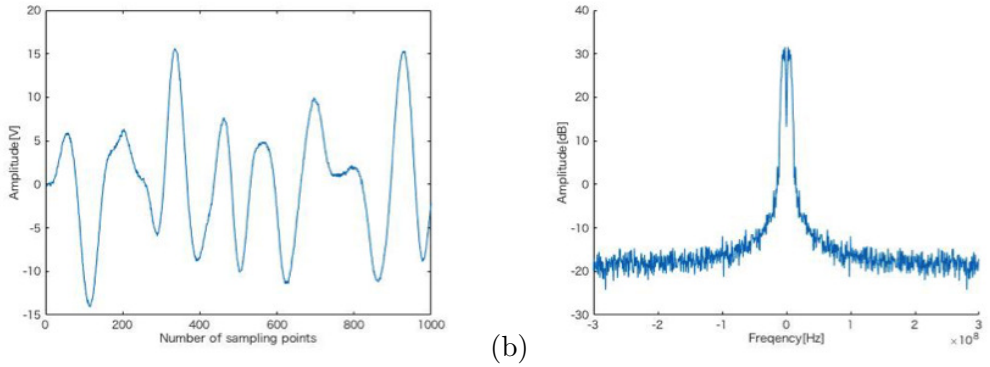

(a) (b)

Figure 4.5: The echo $\boldsymbol{y}$ generated by convolving the one cycle pulse with $\boldsymbol{h}$ and adding observation noise is shown in (a) and its PSD is shown in (b).

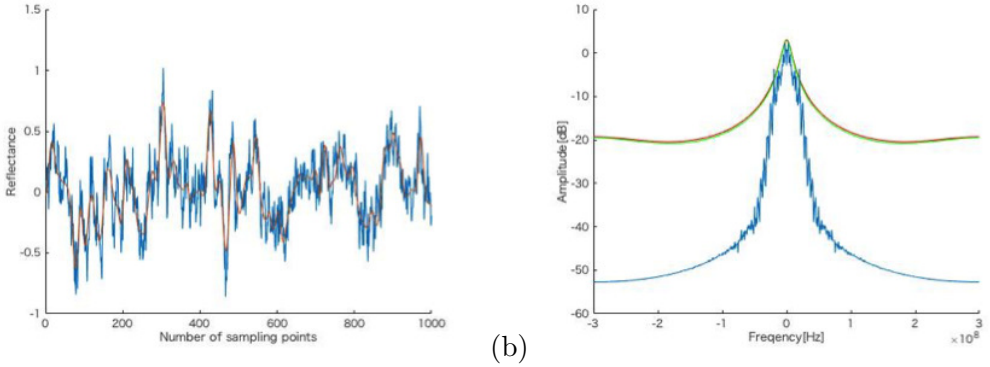

(a) (b)

Figure 4.6: $\hat{\boldsymbol{h}}$ restored for one cycle pulse transmission is indicated by red line in (a) and blue line is set value. The PSD of the restored result (red line) in (a) is shown in (b) using blue curve, the red curve corresponds to the theoretical value of the set AR model, and the green curve corresponds to the theoretical value of the estimated AR model.

characteristic seems to be weakened as the order of the AR model increases, that is, the degree of freedom of the AR model increases. In Fig. 4.6(b), there are little differences between the red curve showing the theoretical PSD of the true model and the green curve of the estimated model. Comparing Fig. 4.6(b) with Fig. 4.5(b), it is clear that the PSD of $\hat{\boldsymbol{h}}$ becomes obviously a wide band and approaches the PSD of the set value in Fig. 4.1. In other words, a part not in the high frequency band of the unobservable frequencies can be effectively restored by assuming the AR model.

Finally, we estimated the AR parameters and restore $\boldsymbol{h}$ from the echo generated by five cycles pulse transmission. Fig. 4.7 presents five cycles pulse in time and frequency domain. $\boldsymbol{y}$ and $\hat{\boldsymbol{h}}$ for 5 cycles pulse transmission are shown in Figs. 4.8 and 4.9. The parameters are estimated as $\hat{\boldsymbol{a}} = \{0.546, 0.365\}$ and $\hat{\sigma_h^2} = 0.0168$. Since the frequency band to be observed is further limited, the estimation error of the parameters is slightly

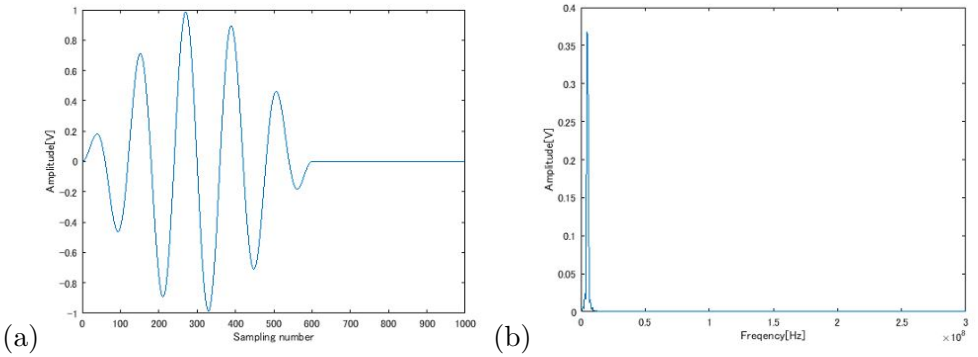

(a) (b)

Figure 4.7: Five cycles pulse: (a) time waveform; (b) frequency domain.

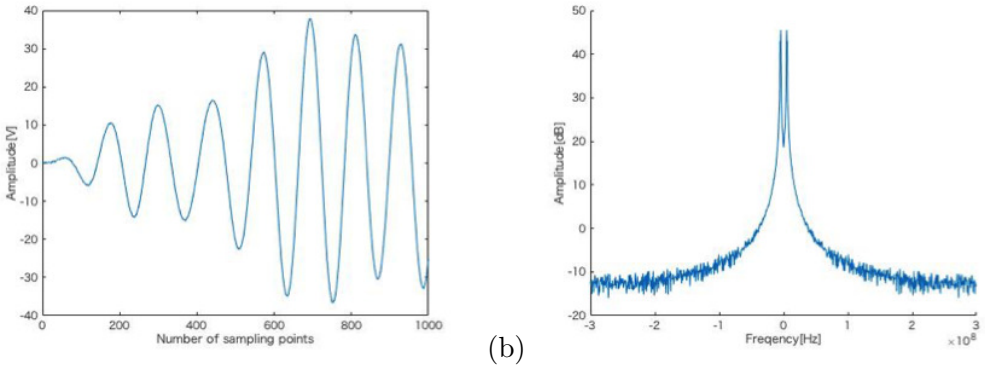

(a) (b)

Figure 4.8: The echo $\boldsymbol{y}$ generated by convolving the five cycles pulse with $\boldsymbol{h}$ and adding observation noise is shown in (a) and its PSD is shown in (b).

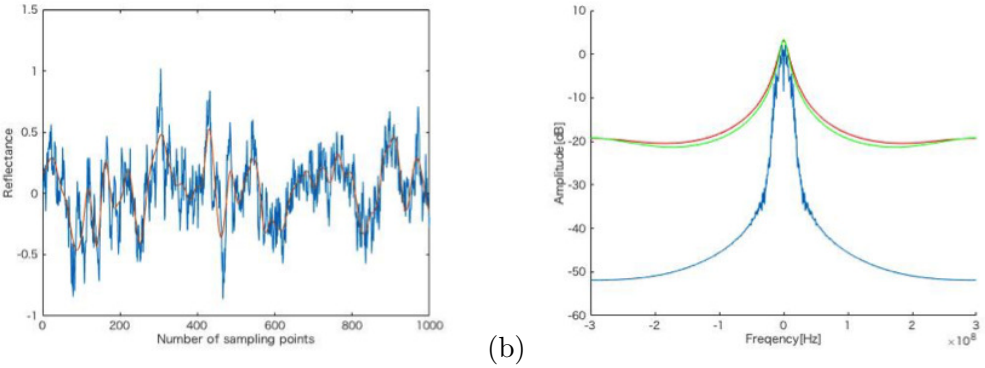

(a) (b)

Figure 4.9: $\hat{\boldsymbol{h}}$ restored for five cycles pulse transmission is indicated by red line in (a) and blue line is set value. The PSD of the restored result (red line) in (a) is shown in (b) using blue curve, the red curve corresponds to the theoretical value of the set AR model, and the green curve corresponds to the theoretical value of the estimated AR model.

larger than the estimation error of the one cycle transmission. However, the theoretical PSD computed using $\hat{\boldsymbol{a}}$ and $\hat{\sigma_h^2}$ is sufficiently close to that of the true model.

The above results are better than expected and it was confirmed that the empirical Bayesian method is very useful for latent variable estimation where the observation is limited and the parameters of the prior knowledge of the latent variable are unknown [182]. Our subject in this chapter can be interpreted as extrapolation problem of PSD observed in the limited narrow frequency region.

4.6 Numerical Evaluation for Frequency Domain Method

4.6.1 Evaluation method

Like section 4.5.1, the setting value of $\boldsymbol{h}$ to be recovered is the same, which the parameters are $\boldsymbol{a} = \{0.6, 0.3\}$ and $\sigma_h^2 = 0.02$. In this case, an example of the setting value of $\boldsymbol{h}$ to be recovered is shown in Fig. 4.10(a), and the power spectrum is shown in Fig. 4.10(b). For $\boldsymbol{y}$, the noise variance is $\sigma_n^2 = 0.02$, and we use 1 cycle of 5 MHz and 5 cycles of 5 MHz as the transmission pulse.

4.6.2 Results

We attempted to restore $\boldsymbol{h}$ using frequency domain method. First, we consider that the transmission pulse is one cycle pulse. In this case, $\boldsymbol{y}$ and its square amplitude of $\boldsymbol{y}$ in frequency domain are shown in Fig. 4.11. The restored $\hat{\boldsymbol{h}}$ is shown in Fig. 4.12, and the estimated parameters are $\hat{\boldsymbol{a}} = \{0.6407, 0.6404\}$ and $\hat{\sigma_h^2} = 0.0875$, and the estimation error is slightly larger than that of time domain method.

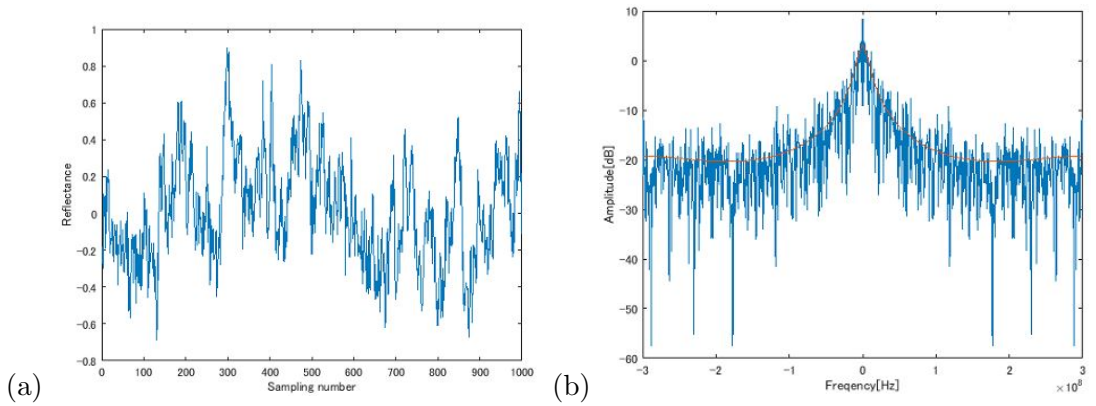

(a) (b)

Figure 4.10: One series of $\boldsymbol{h}$ consisting of 1,000 samples for frequency domain method is shown in (a), and its power spectrum is shown in (b). The red curve in (b) indicates the theoretical power spectrum of the set AR model.

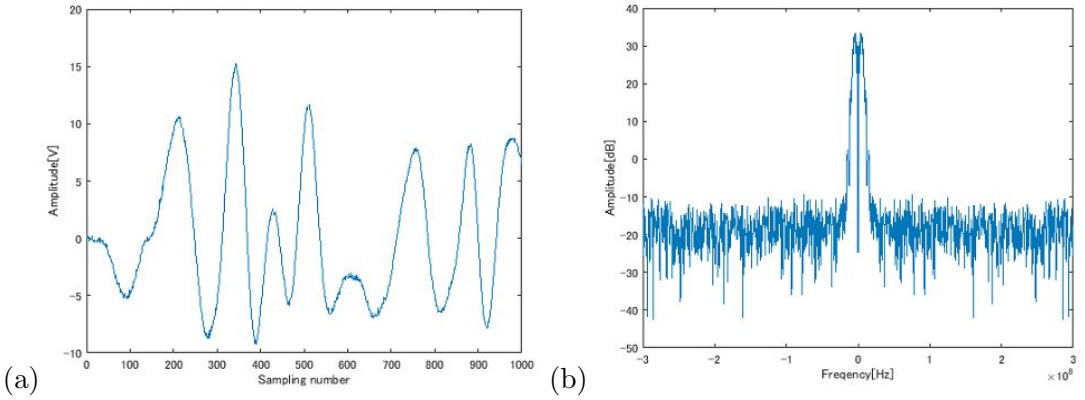

Figure 4.11: The echo $\boldsymbol{y}$ generated by convolving the one cycle pulse with $\boldsymbol{h}$ and adding observation noise is shown in (a) and its square amplitude of $\boldsymbol{y}$ in frequency domain is shown in (b).

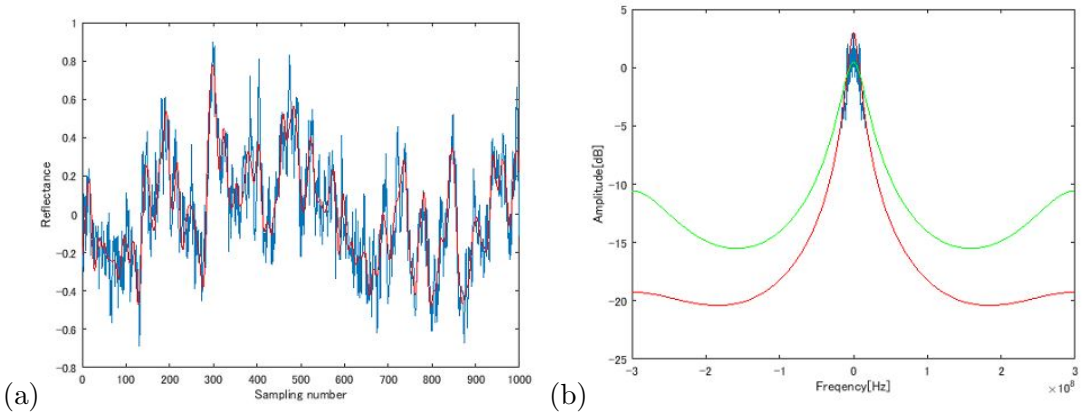

Figure 4.12: $\hat{\boldsymbol{h}}$ restored for one cycle pulse transmission is indicated by red line in (a) and blue line is set value. The PSD of the restored result (red line) in (a) is shown in (b) using blue curve, the red curve corresponds to the theoretical value of the set AR model, and the green curve corresponds to the theoretical value of the estimated AR model.

After that, we attempted to restore $\boldsymbol{h}$ when the transmission pulse is five cycles pulse. In this case, $\boldsymbol{y}$ and its square amplitude of $\boldsymbol{y}$ in frequency domain are shown in Fig. 4.13. The restored $\hat{\boldsymbol{h}}$ is shown in Fig. 4.14, and the estimated parameters are $\hat{\boldsymbol{a}} = \{0.6753, 0.6757\}$ and $\hat{\sigma_h^2} = 0.0883$, and the estimation error is considerably larger than that of the time domain method.

For comparison, the estimates simply restored by Eq. 4.2 are shown in Fig. 4.15, where the singular values of $\boldsymbol{W}$ greater than σ_n^2 are used to define $\boldsymbol{W}^+$. As a result of observation noise amplification, $\hat{\boldsymbol{h}}$ shown by a red line has large noisy component. These results relatively indicate the effectiveness of the application of our method, including the method in time domain and the method in frequency domain.

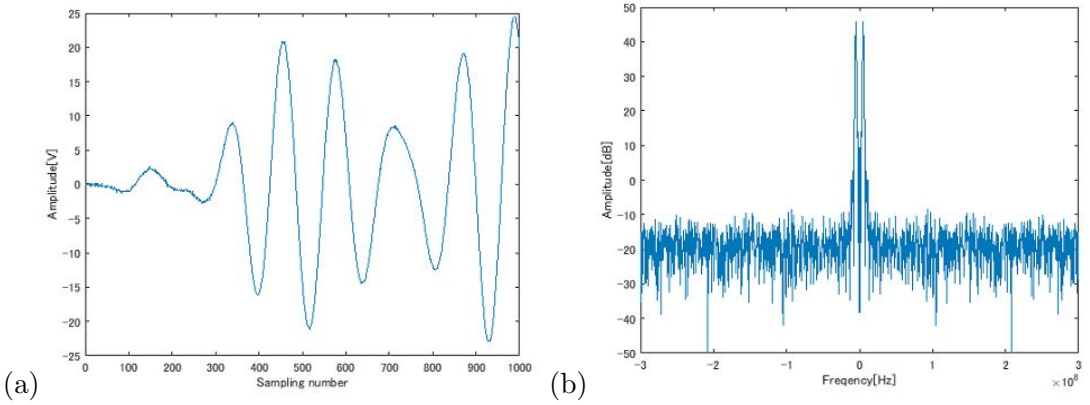

(a) (b)

Figure 4.13: The echo $\boldsymbol{y}$ generated by convolving the five cycles pulse with $\boldsymbol{h}$ and adding observation noise is shown in (a) and its square amplitude of $\boldsymbol{y}$ in frequency domain is shown in (b).

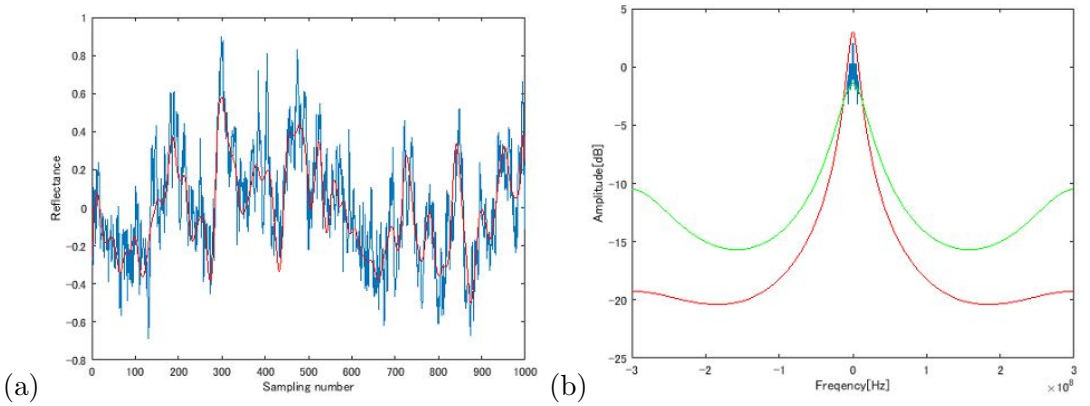

(a) (b)

Figure 4.14: $\hat{\boldsymbol{h}}$ restored for five cycles pulse transmission is indicated by red line in (a) and blue line is set value. The PSD of the restored result (red line) in (a) is shown in (b) using blue curve, the red curve corresponds to the theoretical value of the set AR model, and the green curve corresponds to the theoretical value of the estimated AR model.

Regarding the results of time domain method, the results of frequency domain method maintain a relatively large error. The proposed time domain method is a good candidate for reflectivity recovery applications at least under the condition adopted this time. However, since the evaluation is a result only for second order AR model and the evaluation by statistical analysis is not performed, more quantitative evaluations need to be conducted.

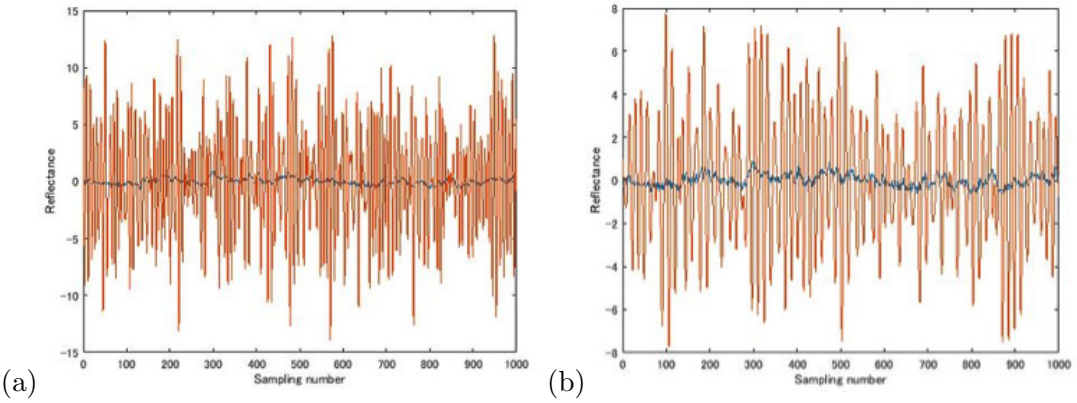

(a) (b)

Figure 4.15: $\hat{\boldsymbol{h}}$ obtained by pseudo-inverse filtering for one cycle pulse transmission is shown in (a) and that for five cycles pulse transmission is shown in (b). Red line indicates $\hat{\boldsymbol{h}}$ and blue line indicates set $\boldsymbol{h}$.

4.7 Conclusions

In this study, in order to restore scatterer distribution from ultrasonic echo, the empirical Bayesian method was first adopted. Although AR model identification is usually performed directly on the observed time series, in this problem, it is a latent time series that model identification should be done, and the identification is impossible with the well-known Levinson-Durbin algorithm. In identifying and restoring the latent time series in this study, an ill-posed characteristic is strong, that is, observations are largely restricted. However, we confirmed through ideal data simulations that the empirical Bayes could properly solve the problem.

The focus then drifted to the frequency domain technique, which using the evaluation function J to get the wanted parameters. As a consequence, the restoration of $\boldsymbol{h}$ can be retrieved from the MAP estimation. Indeed, due to their feasibility, they allow appropriate modeling the reflectivity to some extent. However, the accuracy of this method is inferior to the empirical Bayesian-based method in the time domain.

The simulations were carried out only under restricted conditions, and there are still some important matters deserved to be confirmed. First, the performance of the empirical Bayes against the higher order AR models should be evaluated. Various complicated conditions, for example, the characteristics of a transducer and a propagation medium should be taken into consideration. To do so, we are advancing simulations based on finite element method (FEM) using PZFlex, a standard FEM code for ultrasound analysis. For the reason that the echo generation process is complicated and depends not only on reflection but also on transmittance and diffraction, it is difficult in principle to restore the reflectance of the scatterers purely. However, the obtained $\hat{\boldsymbol{h}}$ contains

information on the tissue, and we expect to be able to diagnose tissue properties from the change $\hat{\boldsymbol{h}}$.

In the next stage, we are going to examine a new imaging system which presents organ boundaries and inside the organ separately. By subtracting the echo corresponding to the image of the inside the organ, which is obtained by the method in this study, from the original echoes, and subsequently applying a method to extract the organ boundaries, the imaging system above is expected to be constructed.

Chapter 5

Strong Scatterer-Based Super-Resolution Ultrasound Imaging

5.1 Introduction

Ultrasound imaging is going through a technology-enabled revolution [183–185]. With the availability of real-time channel data acquisition and software beamforming, new opportunities for improving image quality, more accurate quantification, and higher frame rates in ultrasound imaging have emerged. For instance, transmitting a long pulse wave to enhance the SNR such as chirp-coded imaging [186, 187] or maximum-length sequence (M-sequence)-coded imaging [188, 189]; synthetic aperture (SA) imaging to achieve dynamic focusing in both transmitting and receiving [190–192]; 2D micromachined ultrasound array transducers to generate 3D ultrasound images [193, 194]; compounding imaging to reduce the clutter and artifacts [195–197]; and non-linear imaging to enhance the resolution and contrast [198–200]. Therefore, by exploiting new flexibility in the channel data combined with increased processing capabilities, there is still considerable potential for further improvement in ultransound imaging quality.

We proposed the super resolution FM-chirp correlation method (SCM) [201] as a super-resolution ultrasound imaging technique. In the method, multiple transmission/reception operations (TRs) for each imaging line are required as a focused beam, which reduces the frame rate. In order to improve the frame rate, the synthetic aperture-SCM (SA-SCM) was proposed. In this scheme, a divergent wave is transmitted and it was demonstrated by simulations that the SA-SCM offers both high frame rate and high

range resolution performance. However, these methods generate the lateral discontinuities, because the SCM processing is performed line by line in the image. On the other hand, the SCM processing uses the phase information of the different frequency carrier waves to realize super resolution in the range direction. Hence, high-frequencies are desired to improve the range resolution. In addition, a high-frequency pulse is desired to generate a narrower beam, which helps to improve the lateral and contrast resolutions. However, rapid attenuation and grating lobes are issues which are still to be solved.

In order to solve the lateral discontinuities, in this study, we propose another version called SCM-weighted SA [202] in which the SCM is performed on each echo received by each transducer element and the SCM result is used as a weight for DAS beamforming in the subsequent SA step. The SCM-weighted SA can generate multiple B-mode images each of them corresponds to each carrier frequency, and the appropriate low frequency images among them have no grating lobes.

The multiple frequency B-mode images can be generated by the SCM-weighted SA and the frequency characteristics of the biological tissue are expected to be extracted from those images. Alternatively, in order to improve the SNR and the contrast, those images can be integrated into one image. Thereafter in this study, not just simply averaging multiple frequency images obtained by the SCM-weighted SA, we propose a new method called SCM-weighted SA-SCM. In the SCM-weighted SA-SCM, the SCM processing is applied again to the image lines of the multiple frequency images from the SCM-weighted SA instead of the application of simple average processing. We show the experimental results and indicate that the SCM-weighted SA-SCM further improves the spatial resolution and removes the grating lobes shown in the high frequency images derived by the SCM-weighted SA.

5.2 Methods

5.2.1 SA beamforming method

One of the major methods for beamforming is focusing. In transmission, delays are applied to control the contributions coming from all transducer's elements to achieve a given point, called focal point in tranmission. In reception, the echoes received by the elements (raw channel data) are delayed so that they sum contributions coming from the same given point of the medium, called the focal point in the reception. Beamforming is more extensive in reception than in transmission. During reception, the raw channel data can be stored, and the algorithms can be selected to improve the results according

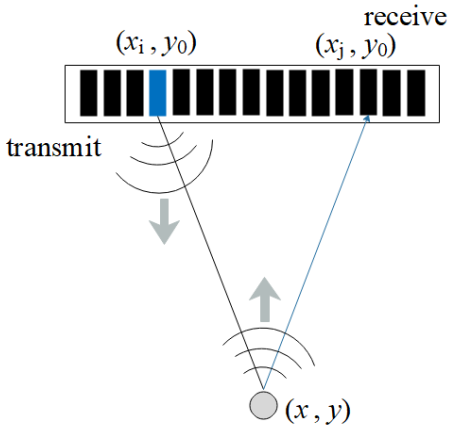

Figure 5.1: Schematic of synthetic aperture imaging.

to the postprocessing. However, in transmission, once the elements have been excited, we cannot control the process of beamforming anymore and preprocessing is limited.

We use hereafter the DAS [203] as a reception beamformer, which is the most conventional method. As shown in the Fig. 5.1, a spherical diverging wave is emitted by one element in a linear array, and after a complex combination of reflection, refraction, scattering and attenuation, the echo is received by all elements in the linear array. As a reception dynamic focus, the amount of delay time applied to each array element with respect to the focus point (x, y) can be calculated by:

$$\tau = \frac{\sqrt{(x_i - x)^2 + (y_0 - y)^2} + \sqrt{(x_j - x)^2 + (y_0 - y)^2}}{c}, \tag{5.1}$$

where (x_i, y_0) is the coordinate of the ith element in the transmitting array, (x_j, y_0) is the coordinate of the jth element in the receiving array and c is the speed of sound in the propagation medium.

5.2.2 Original SCM

MUSIC algorithm [204, 205] is the most known method in the category of eigenspace-based beamformers. Its main development is based on the idea of separating the eigenspace of the covariance matrix of the raw channel data into signal and noise components using prior information about the covariance of the noise. The original SCM based on the MUSIC algorithm will be introduced.

In transmission, an FM-chirp pulse $s(t) = \mathrm{Re}[x(t)e^{j\omega_0 t}]$ with a center frequency of ω_0 is transmitted, and in reception, the echo signal $y(t)$ in the RF (radio-frequency)-band

received from D point scatterers, which can be formulated as:

$$y(t) = \int_{-\infty}^{\infty} h(\tau)s(t-\tau)d\tau, \tag{5.2}$$

$$h(t) = \sum_{i=1}^{D} h_i \delta(t-\tau_i), \tag{5.3}$$

where $\{h_i\}$ is the set of all scatterers reflectances, $\{\tau_i\}$ is the set of the propagation delay times for the echoes of all scatterers, and $\delta(\cdot)$ is the Dirac delta function. For the sake of generality, we consider the frequency characteristics of both the transducers and the propagation paths are omitted. The received FM-chirped echo is expressed in the form of a baseband IQ (in-phase/quadrature) signal $\nu(t)$, and a compressed signal $z(t)$, can be described:

$$\nu(t) = \sum_{i=1}^{D} h_i x(t-\tau_i)e^{-j\omega_0\tau_i} + n(t), \tag{5.4}$$

$$z(t) = \sum_{i=1}^{D} h_i r(t-\tau_i)e^{-j\omega_0\tau_i} + m(t), \tag{5.5}$$

where $r(t)$ is the auto-correlation function of $x(t)$ in the base band that takes complex values. The observation noise $n(t)$ is assumed to be Gaussian white noise with variance σ^2, and $m(t)$ is the complex-valued cross-correlation of $x(t)$ and $n(t)$.

Note that in the form of Eq. 5.5, we assume that the echo from each scatterer has a phase that depends on both the carrier frequency ω_0 and the scatterer's position. To make the scatterer separation based on the phase information possible, different carrier frequencies were applied. In this case, the sets of $\{z(t)\}$ are obtained by varying ω_0. Further simplifying Eq. 5.5 by a discrete representation, we use the compressed echo vector $\boldsymbol{z} \equiv [z(t_1), z(t_2), \cdots, z(t_M)]^\top$; the steering vector $\boldsymbol{r}_i \equiv [r(t_1 - \tau_i), r(t_2-\tau_i), \cdots, r(t_M-\tau_i)]^\top$ to indicate the compressed echo of the ith scatterer, and the noise vector $\boldsymbol{m} \equiv [m(t_1), m(t_2), \cdots, m(t_M)]^\top$, where M is the number of sampling time. Using the array manifold matrix $\boldsymbol{\Gamma} \equiv [\boldsymbol{r}_1, \boldsymbol{r}_2, \cdots, \boldsymbol{r}_D]$ and the gain vector $\boldsymbol{g} \equiv [h_1 e^{-j\omega_0\tau_1}, h_2 e^{-j\omega_0\tau_2}, \cdots, h_D e^{-j\omega_0\tau_D}]^\top$, $\boldsymbol{z}$ and its variance-covariance matrix $\boldsymbol{R}$ can be formulated as follows:

$$\boldsymbol{z} = \boldsymbol{\Gamma}\boldsymbol{g} + \boldsymbol{m}, \tag{5.6}$$

$$\boldsymbol{R} = \boldsymbol{\Gamma}\boldsymbol{G}\boldsymbol{\Gamma}^\top + \boldsymbol{R}_n, \tag{5.7}$$

where $\boldsymbol{G} \equiv E_{\omega_0}\left[\boldsymbol{g}\boldsymbol{g}^H\right]$, $\boldsymbol{R}_n \equiv E_n\left[\boldsymbol{m}\boldsymbol{m}^H\right] = \sigma^2\boldsymbol{R}_0$, $E[\cdot]$ denotes the expectation operators, the superscript $\top$ and H denote the transpose of a vector or matrix and the conjugate transpose, respectively. It is clearly seen that the echoes and the observation noise are statistically independent. The symmetrical matrix $\boldsymbol{R}_0$ consists of $r(t)$, and its

(k,l)th element is $r(t_k - t_l)$. The covariance matrix $\boldsymbol{R}$ that can be decomposed by using the eigenvalues $\{\lambda_i\}$ and the eigenvectors $\{\boldsymbol{e}_i\}$, which can be expressed as follows:

$$\boldsymbol{R}\boldsymbol{e}_i = \lambda_i \boldsymbol{R}_0 \boldsymbol{e}_i, \quad i = 1, 2, \cdots, M. \tag{5.8}$$

When $M > D$, the column vectors of $\boldsymbol{\Gamma}$ are linearly independent, and thus the rank of $\boldsymbol{R} - \boldsymbol{R}_n = \boldsymbol{\Gamma}\boldsymbol{G}\boldsymbol{\Gamma}^H$ is D. Therefore, $\boldsymbol{R}$ has D generalized eigenvalues that are greater than σ^2 and $M - D$ generalized eigenvalues that are equal to σ^2. The set of D eigenvectors $\{\boldsymbol{e}_i\}_{i=1}^{D}$ that corresponds to the D largest eigenvalues spans the signal subspace. The remaining $M - D$ eigenvectors $\{\boldsymbol{e}_i\}_{i=D+1}^{M}$ thus span the noise subspace.

The SCM estimates the true delay using the MUSIC algorithm, the orthogonality between the steering vector and the noise subspace can be evaluated by varying the delay time of the steering vector as per a super-resolution delay profile $S(t_i)$, which is defined as:

$$S(t_i) \equiv \frac{\boldsymbol{r}_i^H \boldsymbol{R}_0^{-1} \boldsymbol{r}_i}{\sum_{j=D+1}^{M} |\boldsymbol{r}_i^H \boldsymbol{e}_j|^2}. \tag{5.9}$$

If t_i matches the actual scatterer position, the corresponding $\boldsymbol{r}_i$ is then orthogonal to $\{\boldsymbol{e}_j\}_{j=D+1}^{M}$, and the results of Eq. 5.9 thus become sharp peaks. In this scheme, D must be the number of scatterers, and in practical applications, e.g., the Akaike's information criterion (AIC) [206–208] or minimum description length (MDL) criterion [209, 210] are used to determine D. In estimating $\boldsymbol{R}$, the implicit estimation of $\boldsymbol{R}_n$ can be stabilized by performing multiple transmissions, known as snapshots, all of which have the same carrier frequency. However, when the real-time processing requirements are considered, it is better that the number of TRs is small; therefore, in this study, we omitted the snapshot step. In addition, to prevent artifacts being caused through periodicity, we changed the transmission carrier frequency at random. Using the K transmissions with the randomly shifted frequency band, we then estimate $\boldsymbol{R}$ as an ensemble average of $\hat{\boldsymbol{R}} = (\sum_{k=1}^{K} \boldsymbol{z}_k \boldsymbol{z}_k^H)/K$. Here, $\boldsymbol{z}_k$ represents a compressed echo vector that corresponds to the kth transmission.

5.2.3 SA-SCM

The SCM performs super-resolution processing of each imaging line. Therefore, it is necessary to transmit multiple FM chirp pulses with different frequency bands in each direction that correspond to an imaging line; see Fig. 5.2(a). If an image consisting of N lines and K transmissions is formed for each direction, then $N \times K$ transmissions must be made to generate the complete image. This greatly reduces the frame rate of the moving image obtained. To reduce the number of transmission and reception processes that are required, the SCM is extended to an SA-based version, called SA-SCM. In

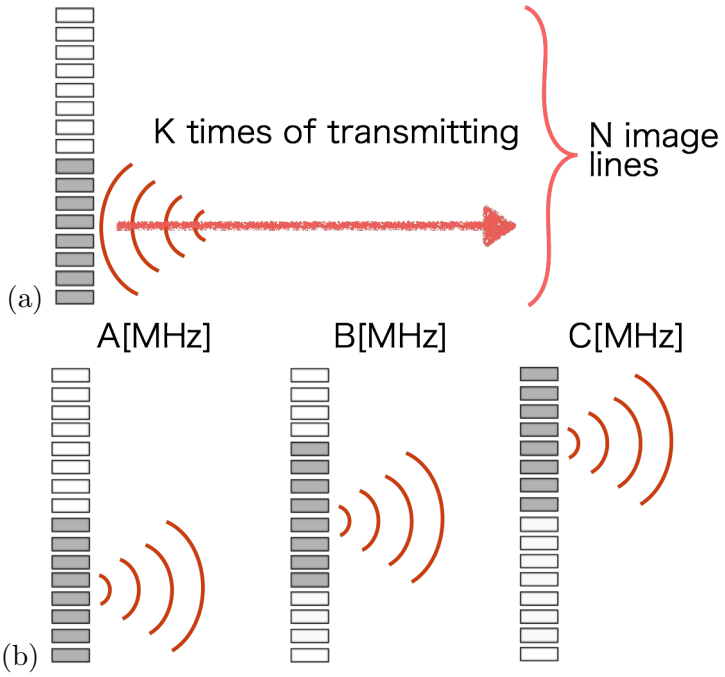

Figure 5.2: Transmission procedures for super-resolution FM-chirp correlation method (SCM) and synthetic aperture SCM (SA-SCM): (a) focused pulse transmission for SCM; (b) unfocused pulse transmission for SA-SCM.

SA, unfocused pulses are transmitted over a wide range from the sub-aperture elements [Fig. 5.2(b)], and for each of these transmission events, echoes from the entire imaging area are received simultaneously by all elements. Dynamic focusing is performed, e.g., using DAS beam forming. By randomly changing the frequency band for each transmitted FM-chirp pulse in the SA process, the total number of transmissions can be reduced. The $N \times K$ times transmission events in the SCM described above are reduced K-fold in the SA-SCM. The echo signals with different frequencies that were obtained by dynamic focusing processes corresponding to each line are used as the inputs of the SCM.

To avoid frequency deviations related to the positioning of the sub-aperture used for transmission, a frequency band is assigned randomly to the position of this sub-aperture. For super-resolution imaging, the SCM algorithm uses the carrier phase information along the imaging line. The carrier that is contained in the compressed echo signal may be disturbed by dynamic focusing and this would cause super-resolution performance degradation.

5.2.4 SCM-weighted SA

In the SCM and SA-SCM, the ultrasound image is a collection of all the frequencies formed by each line. Therefore, discontinuities of the image brightness are likely to

occur in the lateral direction. Besides, for the SCM and SA-SCM, the effect of the grating lobes is unavoidable because the results from all the carrier frequencies are used to synthesis the final result. To avoid these lateral discontinuities and reduce the number of SA processing steps, we can reverse the processing order of the SCM and the SA in the SA-SCM method; this reversal processing causes the SCM to be applied firstly to each echo that is measured at each transducer element, and the results from the SCM are then used as the input for SA processing. However, the SCM results at each element contain no phase information and are simply positively-valued signals. Therefore, the cancellation of the positive and negative signals, which is expected to reduce the number of unwanted signals, is less likely to occur. For further improvements, a strategy in which the SCM results are used as weights for SA processing can be considered, and this version is called SCM-weighted SA [202].

As the SCM processing is performed first for each element, the number of SA operations can be reduced. Therefore, SCM-weighted SA also offers the potential to reduce the computation time required for each image. But it should be noted that in the SCM-weighted SA method, in contrast to the SA-SCM, the transmission position at the transducer must be fixed. When different frequency pulses are transmitted from different positions, the positions of the corresponding reflected waves are shifted between the echoes of the different frequencies received by each element, and SCM processing then cannot be executed in the SCM-weighted SA.

5.2.5 SCM-weighted SA-SCM

As stated above, in order to reduce the lateral discontinuities, the SCM-weighted SA method was proposed. In the SCM-weighted SA, it can generate multiple frequency images, and the grating lobes can be suppressed in the low frequency images. When the multiple frequency images are averaged to generate high SNR B-mode image, its spatial resolution becomes an intermediate value of the original multiple images and the grating lobe remains. Instead of simple averaging, we adopt the SCM method to integrate the multiple images obtained by the SCM-weighted SA. Namely, the SCM is applied again to each line signals in the results of the SCM-weighted SA. We call it SCM-weighted SA-SCM, which gives more favorite features such as suppression of grating lobes, reduction of noise and further improvement of the range resolution compared to the existing methods. Unlike the SCM-weighted SA, the computational complexity of the SCM-weighted SA-SCM has dramatically increased.

5.3 Experiments

5.3.1 Experimental setup

In the experiments, the transmission and reception sequences were generated by using an experimental platform for medical ultrasound (RSYS0003, Microsonic Inc., Japan) with a sampling rate of 31.25 MHz, as shown in Fig. 5.3. The number of transducer elements used for both transmission and reception is 64, while the element pitch is 0.315 mm. A linear array probe (T0-1599, Nihon Dempa Kogyo Co., Ltd., Japan) was also used. This probe's center frequency is 7.5 MHz and its specific bandwidth is 70%. The signal processing required was performed offline by using MATLAB software.

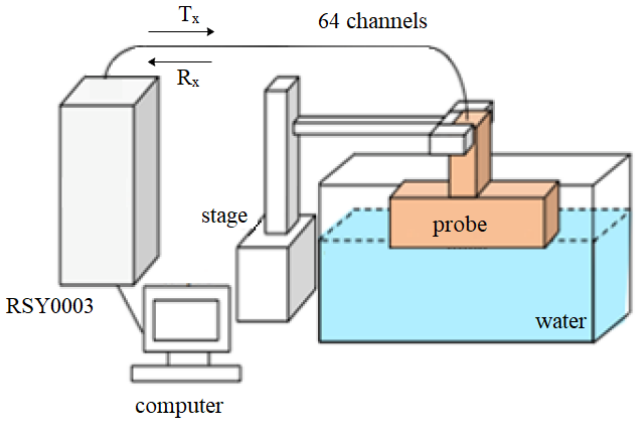

(a)

(b)

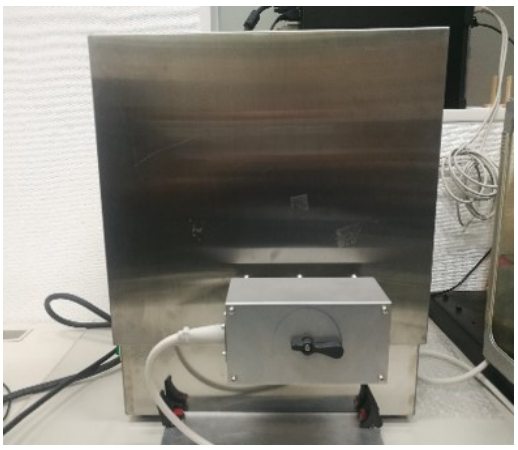

(c)

Figure 5.3: Experimental conditions: (a) experimental system used for the measurements; (b) ultrasound experimental platform RSYS0003; (c) illustration of the probe.

Table 5.1: Parameter settings for transmitted FM-chirp pulse

Parameter	Value
Frequency band width	2 MHz
Chirp pulse duration	5 μs
Variation range of center freq.	6.5 to 8.5 MHz
Applied voltage	20 V
Number of transmission	15
Apodization	Hanning window

5.3.2 Experiment using vinyl-coated metal wire

Considering the low reflectance of biological tissue, we used a vinyl-coated metal wire instead of a pure metal wire for the imaging target in this experiment. The vinyl-coated metal wire with a diameter of 1.5 mm that was placed in the water at a distance of 10 mm from the transducer as an imaging target, as shown in Fig. 5.4. In fact, the reflection coefficient of the vinyl coated metal wire used in this study was not so high, and we confirmed that saturation of the echo signal did not occur. The divergent waves were transmitted by using a central sub-array composed of 8 elements with a focal point of -0.63 mm with respect to the sub-array width of 2.52 mm. Because the probe element spacing is wider, it is likely that grating lobes will be formed. The frequency band of the FM chirp pulse that is used in the experiment is set at a relatively narrow 2 MHz, as described in the Table 5.1. Although the frequency band that is used is not the most effective band for all the transmissions, it was confirmed that it can be performed appropriately.

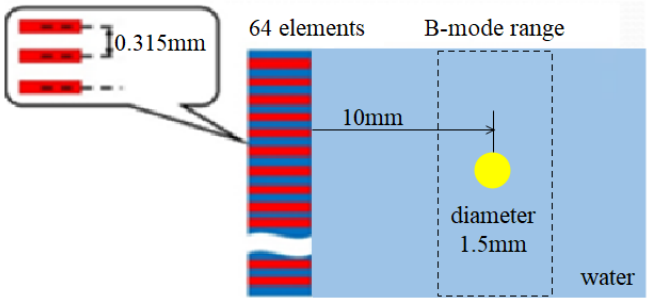

Figure 5.4: Experiment using vinyl-coated metal wire.

5.3.3 Experiment using phantom

Subsequently, we present the experimental results obtained by using a soft tissue-mimicking phantom (US-2 multi-purpose phantom N-365; Kyoto Kagaku Co., Ltd., Japan, see Fig. 5.5), with a speed of sound of $1,432$ m/s, acoustic impedance of 1.38 Rayl and attenuation of 0.59 dB/cm/MHz at 25°C. As shown in Fig. 5.6, the phantom includes six nylon wires which will be used for experiments, each of which has a diameter of 0.05 mm. The distances between these wires are 0.5 mm, 1.0 mm, 2.0 mm, 3.0 mm and 4.0 mm, as measured from the side that is near to the phantom's surface. The

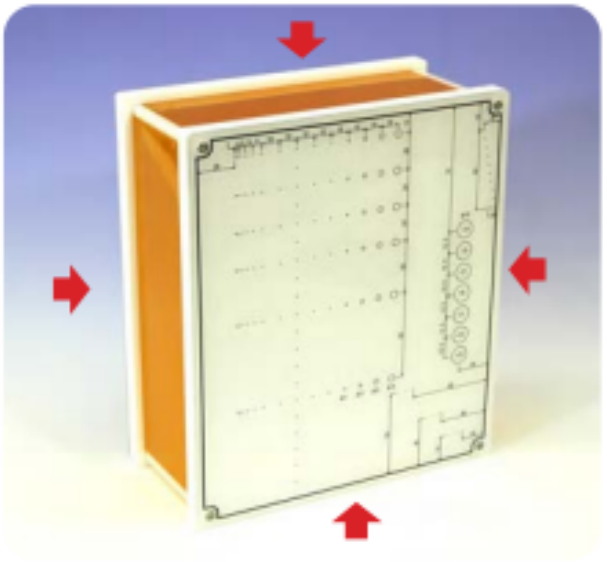

(a)

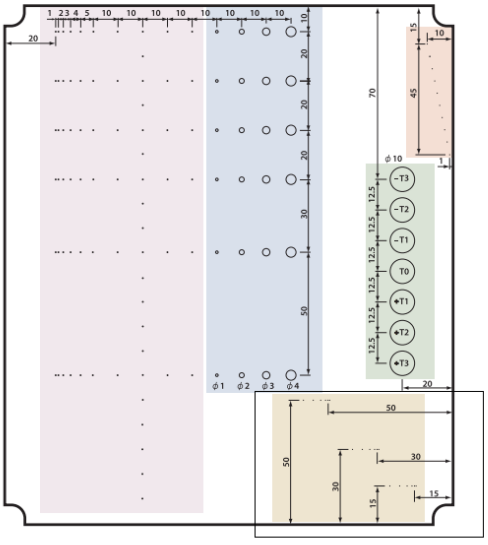

(b)

Figure 5.5: Phantom N-365: (a) schematic diagram; (b) target layout.

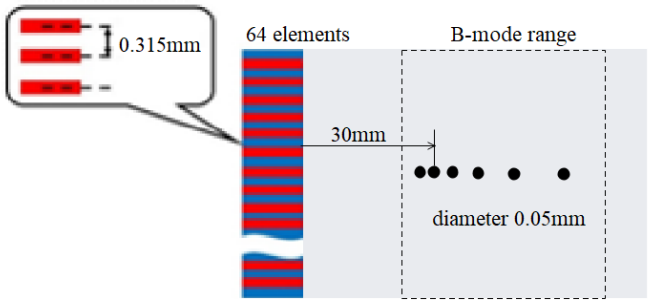

Figure 5.6: Experiment using soft tissue-mimicking phantom (the black line part of the Fig. 5.5(b)).

transmission condition, including the frequency band and the number of transmission, is also as same as that in the experiments using the vinyl-coated metal wire.

5.4 Experimental Results and Discussion

5.4.1 Results of vinyl-coated metal wire

Based on the original SCM reviewed above, the dimension D of the signal subspace theoretically corresponds to the number of point scatterers. Therefore, we set $D = 1$ uniformly for all SCM processing in the wire experiments.

As mentioned in Introduction, we want to detect a strong scatterer with high resolution and suppress unnecessary signals such as speckles. In the radar signal processing, a technique called CFAR (Constant False Alarm Rate) [211] is often used to keep the false alarm probability constant by making the fluctuation of the unnecessary signal uniform. Therefore, in this study, we also show the B mode imaging result normalized in amplitude by the fluctuation range of grating lobes and speckles by each method (adopting standard deviation). The results of the metal wire experiment by this normalization method are shown in Fig. 5.7. In the case of the SA and SCM-weighted SA, the images that were acquired by using the average of 15 pulse transmissions, with each transmission correspondings to each frequency. In Fig. 5.7(b), the SA-SCM produces the result with high range resolution and lateral discontinuity. Although the SCM-weighted SA (Fig. 5.7(c)) offers good continuity in the lateral direction, the artifacts corresponding to the grating lobes are remarkable. Clearly, the SCM-weighted SA-SCM (Fig. 5.7(d)) proposed in this study presents superiority over the SCM-weighted SA in terms of improving the range resolution and lowering the artifacts of the final image.

To quantitatively examine the range resolution, Fig. 5.8 shows the cross-sectional view in the range direction near the target. In this figure, we using standard deviation normalization, specifically by subtracting the corresponding noise from the signal, and then normalizing via dividing by the corresponding standard deviation. From the figure, it can be confirmed that the SCM-weighted SA-SCM has a very high resolution in the range direction and that the resolution is somewhat higher than both the SA-SCM and SCM-weighted SA.

To confirm artifacts corresponding to grating lobes, the results of the SA for different frequencies are shown in Figs. 5.9(a) and (b). From the results, we can observe that as the frequency grows higher, grating lobes stand out conspicuously in the SA. Since the SA-SCM uses these information line-by-line to perform the SCM processing, these grating lobes cause artifacts. The SCM-weigthed SA can similarly generate B-mode images for each transmission, so the results for different frequencies of the SCM-weighted SA are shown in Figs. 5.9(c) and (d), the grating lobe was not so noticeable in Fig. 5.9(c), but there is a concern when using a higher frequency as shown in Fig. 5.9(d). For

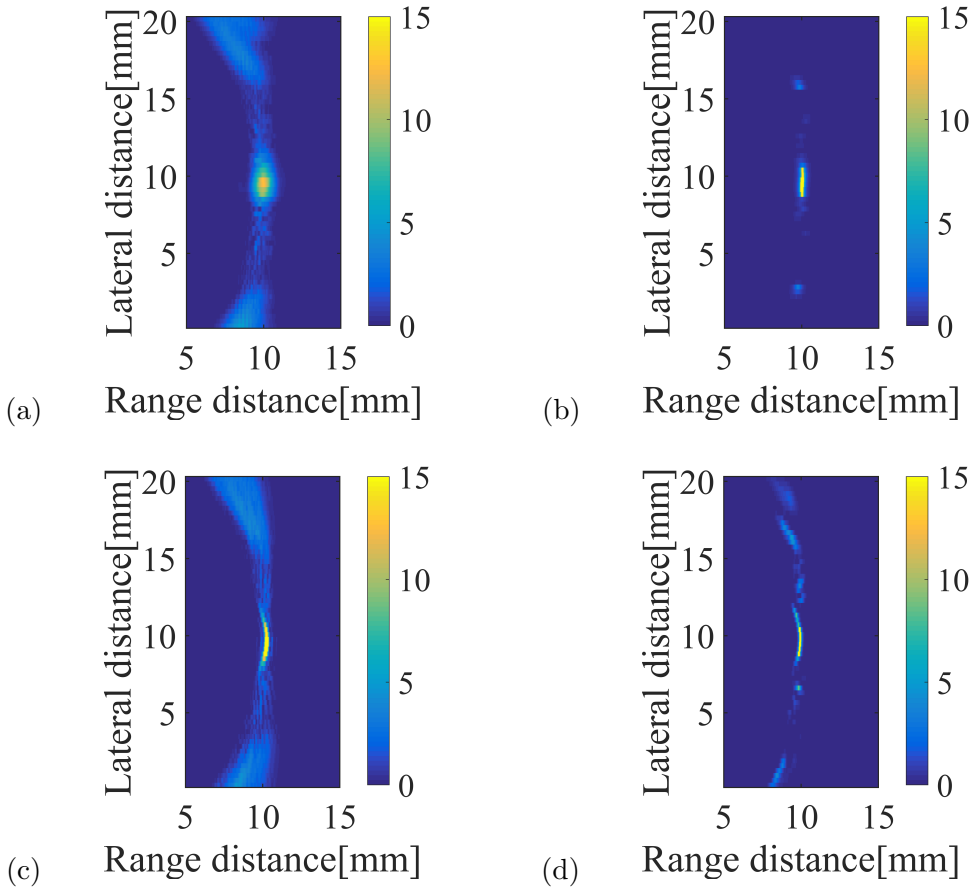

Figure 5.7: B-mode images of metal wire acquired by (a) averaged SA; (b) SA-SCM; (c) averaged SCM-weighted SA; and (d) SCM-weighted SA-SCM. Color bar shows in linear range, not in dB.

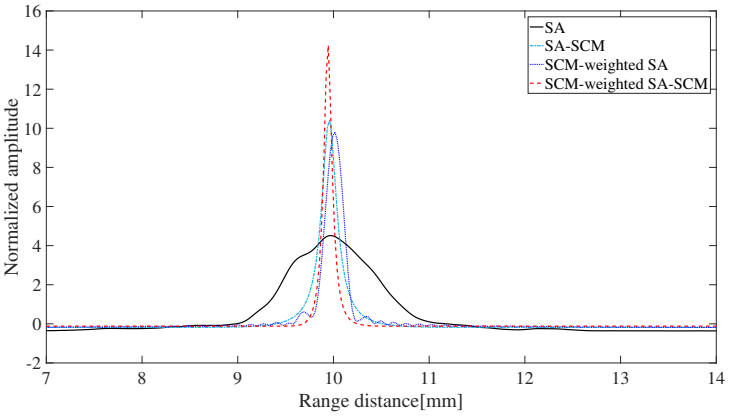

Figure 5.8: Comparison of range resolution corresponds to Fig. 5.7.

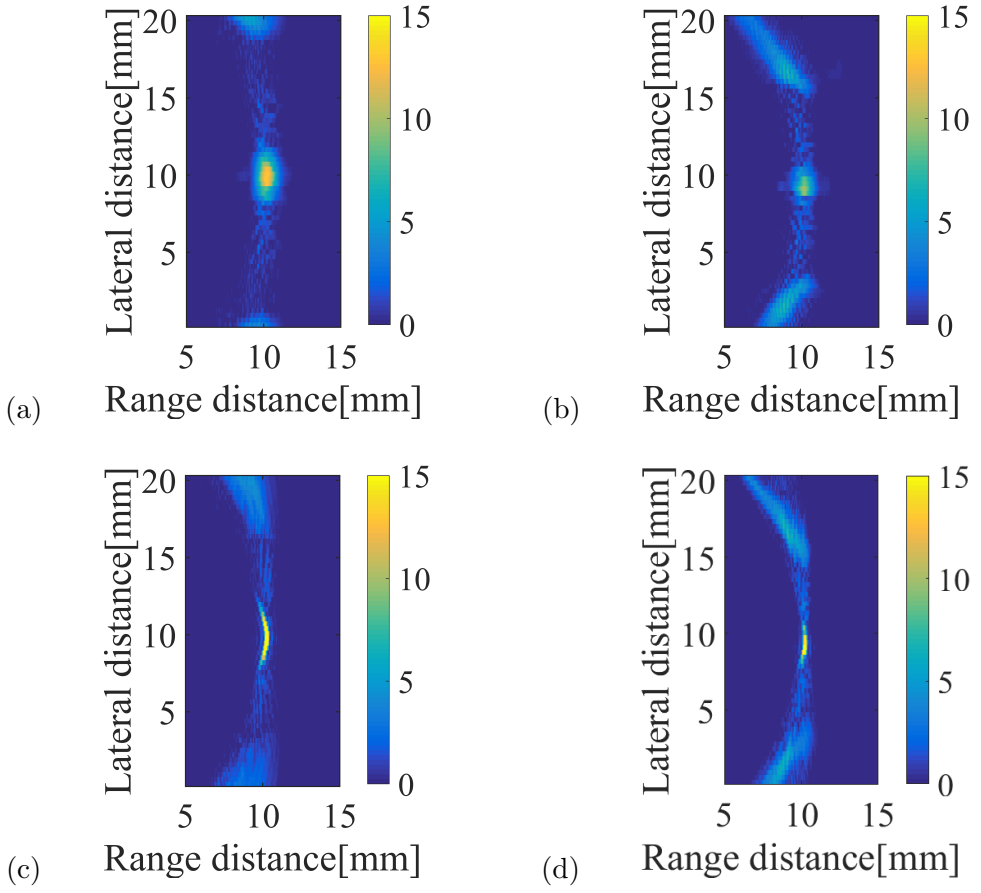

Figure 5.9: B-mode images of metal wire acquired by: (a) SA with 6.5 MHz; (b) SA with 8.5 MHz; (c) SCM-weighted SA with 6.5 MHz; and (d) SCM-weighted SA with 8.5 MHz. Color bar shows in linear range, not in dB.

further improvements, the SCM-weighted SA-SCM is considered, and from the result, it is confirmed that the proposed method has the high range resolution and less artifacts in the final image.

5.4.2 Results of phantom

As explained in Sec. 5.2.2, in theory, $D = 6$ is should be used to calculate the signal subspace via SCM processing in the phantom experiments, so we set $D = 6$ uniformly for all the SCM processing.

Fig. 5.10 shows the B-mode images using the SA, the SA-SCM, the SCM-weighted SA and the SCM-weighted SA-SCM, respectively. The B-mode images of the SA and the SCM-weighted SA were generated as average of 15 images. For the SA-SCM (Fig. 5.10(b)), the result shows a significant improvement of the range resolution compared with the SA (Fig. 5.10(a)). However, the deepest scatterer in the phantom can not be clearly detected in the SA-SCM. This observation is coherent with the fact that SA-SCM is capable of improving the range resolution with the signal and noise components which are clearly decomposed. In this experiment, the intensity of the distant scatterers is greatly reduced due to the attenuation of the propagation medium, and the propagating pulses are distorted by the effect of scattering by the scatterers existing before them. Because of the large number of scatterers in the phantom, the signal components of the last scatterer can hardly be guaranteed in the SCM processing. Therefore, the SA-SCM improved range resolution of the SA image, at the cost of diagnosable depth. The resolution of the target points is offered by the SCM-weighted SA (Fig. 5.10(c)) that perfectly detects the six scatterers, but the range resolution of the final image is not improved as strong as the SA-SCM. Moreover, by using the SCM-weighted SA-SCM, the range resolution can be further improved, but like SA-SCM, the last scatterer was not clearly detected. Compared with the SA-SCM and the SCM-weighted SA methods, the SCM-weighted SA-SCM highly improved the range resolution at the cost of a slight lateral resolution degradation.

Fig. 5.11 compares the performances of the SA, the SA-SCM, the SCM-weighted SA, and the SCM-weighted SA-SCM to detect scaterers located at range direction. As we all known, in ultrasound imaging systems, transmission of a short pulse can easily improve the range resolution. Therefore, comparisons were made with the results for a wide band pulse when using the entire effective band of the probe at one time. The amplitude profile result acquired using a 4 MHz wide band pulse without FM modulation with the center frequency of 7.5 MHz is also superimposed in Fig. 5.11. From these results, the range resolution using the wide band pulse is better than using the SCM-weighted SA-SCM, however, this is only for the first few scatterers, and the deep scatterers are completely undetectable in the wide band pulse as shown in Fig. 5.10(e). Overall, we can state that the best range resolution of the phantom experiment is obtained by the SCM-weighted SA-SCM.

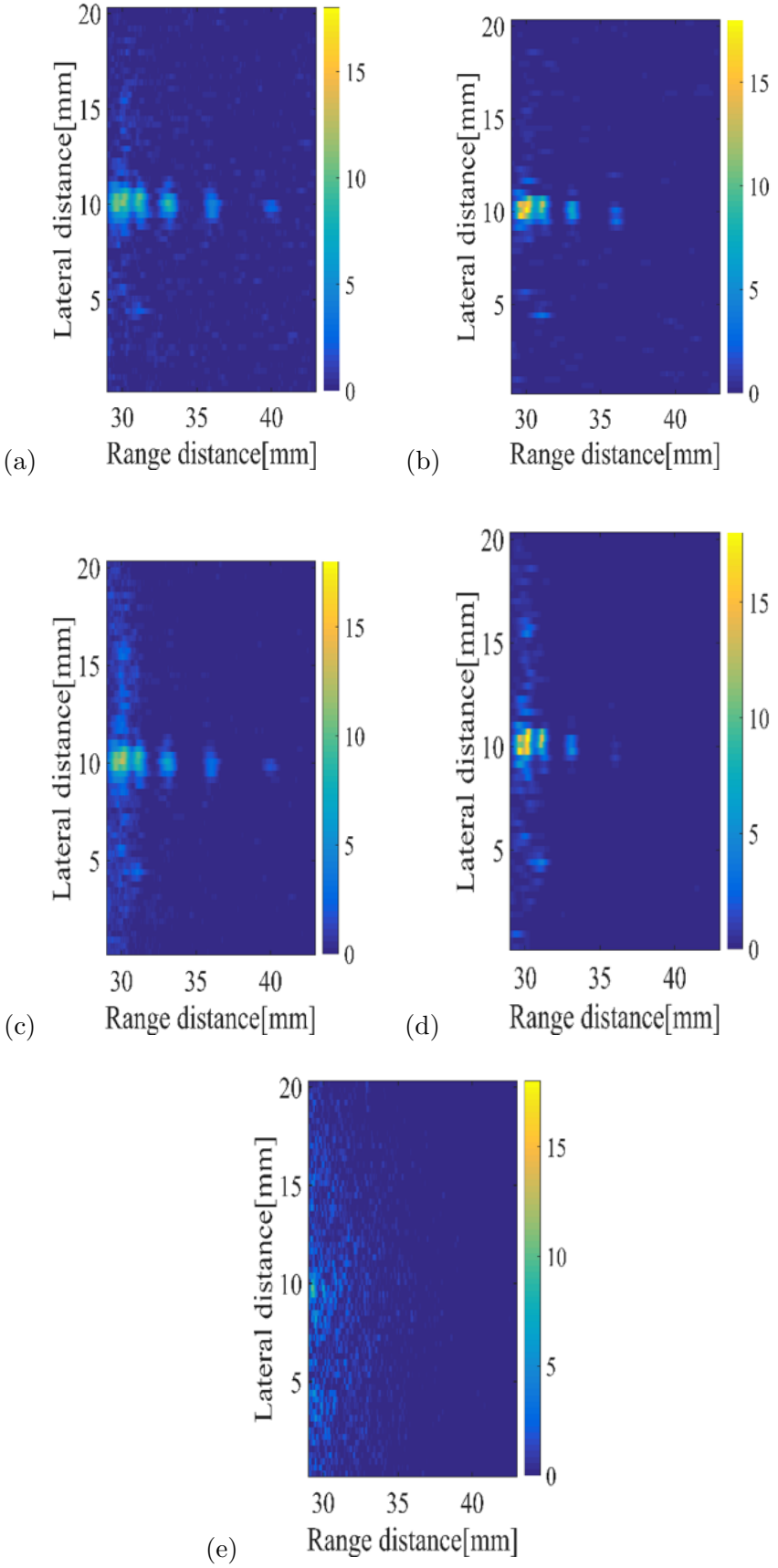

Figure 5.10: B-mode images of phantom acquired by: (a) averaged SA; (b) SA-SCM; (c) averaged SCM-weighted SA; (d) SCM-weighted SA-SCM; and (e) SA with wide band. Color bar shows in linear range, not in dB.

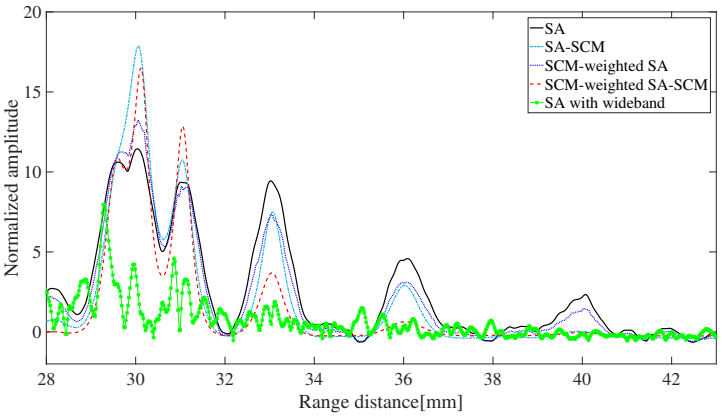

Figure 5.11: Comparison of range resolution corresponds to Fig. 5.10.

5.5 Conclusions

In this study, we investigated the use of SCM-weighted SA and SCM-weighted SA-SCM in metal wire and phantom through simple experiments without moving the sub-array in transmission. Through the experiments, we confirmed their effectiveness and fine imaging is effectively performed by using our methods compared to conventional B-mode imaging.

In the SCM-weighted SA, the current results revealed that the proposed method SCM-weighted SA was able to avoid grating lobes in low frequency images. Furthermore, it may have more potential for constructing the image with low computational calculation costs.

In the SCM-weighted SA-SCM, although the method using the phantom did not detecte all scatterers as expected, all of the results indicated that the proposed method SCM-weighted SA-SCM may have potential to achieve super resolution in the range direction with properly lowering the effects of unwanted artifacts. In the future, it is necessary to confirm the effectiveness of the proposed method by conducting experiments with moving the sub-array in transmission.

The super-resolution method, which is based on the SCM-weighted SA-SCM, is a method which theoretically provides an idea that this processing can be repeated indefinitely until the optimal result is obtained. However, in practical applications, the rationality of the indefinitely repetitions has not yet been confirmed. Because of the limitations of the ultrasonic system, the attenuation of the propagation, and the loss of the noise components during the algorithm calculation.

The SCM-weighted SA-SCM requires high computational cost compared with other proposed methods, it is suitable for imaging scatterers with high reflectance and relatively stationary, such as targeting boundaries of organs or blood vessel walls. Furthermore, small scatterers within the tissue appear as speckle patterns in the B-mode image and are useful not only for the diagnosis of tissue characteristics but also for image processing such as motion analysis. We are currently investigating a method for small scatterers based on empirical Bayes deconvolution [124]. By combining this method with the SCM-weighted SA-SCM, it is possible to realize a new imaging scheme.

Chapter 6

Conclusions and Future Works

6.1 Conclusions and Statement of Contributions

We first investigated the use of PZT-FET receiver in medical ultrasound by creating a structure that enables direct coupling of a PZT element to the gate of a MOSFET. Through the experimental observation, the performances of the proposed device have been shown, which demonstrated that it could offer high sensitivity and wide dynamic range compared to a typical transducer.

Second, we proposed a new estimation for small scatterers in medical ultrasound, by modeling AR processes with unknown parameters. Under this assumption, scatterer distribution can be restored based on empirical Bayesian learning. Concretely, in the time domain, the AR parameters are estimated by maximizing the marginal likelihood function, and the scatterers are estimated as a MAP estimator using these parameters. Such a scheme is stably realized by the EM algorithm. In the frequency domain, the method of steepest descent [181] is used for the evaluation function, and the recovered results could be calculated by the MAP estimator. The proposed framework taking the aforementioned distribution into account and evaluated on simulated data, the results demonstrated the recovery of small scatters could be performed accurately.

Finally, the third contribution is the improvement of ultrasound medical imaging based on the SCM framework for strong scatterers. The proposed methods have advantages in range resolution and suppression of grating lobes. Also, we considered that in combination with the second contribution, a new scheme could simultaneously image small scatterers and strong scatterers.

Overall, we have studied high resolution and high sensitivity imaging of scatterers distribution in medical ultrasound. To the best of our knowledge, this is the first attempt to

specifically consider both the small scatterers distribution and strong scatterers beamforming from received echoes in medical ultrasound imaging. Moreover, the newly proposed device PZT-FET was evaluated, and found it can improve the image accuracy and solve the echo's energy problem.

6.2 Suggestions for Future Research

6.2.1 Exploration of other piezoelectric materials

The specific bandwidth remains low because of the dominance of the PZT resonance at the quarter-wave (1/4 λ) resonance frequency, f_R (14 MHz). Thus, as a potential solution, it may be possible to expand the receiver characteristics and provide further improvements using a relaxer with higher piezoelectric properties than the PZT material.

6.2.2 Further design for PZT-FET MUTs

Another possible solution to enable increased the device performance is to design an array transducer containing many PZT-FET MUTs. In this case, the device may amplify the electrical signal efficiently with a wide frequency bandwidth.

6.2.3 Examination for more AR models

For small scatterers, the empirical Bayesian estimation is applied to echoes; we have confirmed its effectiveness through a second-order AR model. After that, high-order AR models should be assumed, and the most suitable AR model needs to be confirmed.

6.2.4 Evaluation on other types of ultrasonic data

In the empirical Bayesian method, it should be noticed that the validation of the proposed methods is performed only on simulation data. It is very important to evaluate its performance on other types of in vivo data, such as healthy and pathological carotid artery data. In the future, we should conduct experiments on living tissue.

6.2.5 Application in harmonic processing

The SCM framework is based on the carrier phase information, which is useful for fundamental imaging to receive super resolution and statistical stability. Since the harmonic

envelope becomes narrower and the wavelength becomes shorter, the harmonic with the SCM framework is expected to be superior to the fundamental with the SCM framework. It is necessary for further researches to adapt and utilize the SCM technique for harmonic imaging.

6.2.6 Compensation for frequency dependent attenuation

Ultrasound imaging of deep parts in a living body with high resolution and high SNR is strongly required. However, living body has the property of FDA. FDA is a problem that cannot be ignored when using high frequency or harmonic imaging. In the future, we should examine the attenuation characteristics of the steering vector for the SCM framework.

6.2.7 Combination with other processing techniques

In the SCM frame work, our approach is to apply the DAS for the beamforming. However, there are many other beamforming techniques in ultrasound imaging that can be combined with the proposed SCM framework. For further improve the quality of ultrasonic image, methods such as MV or F-DMAS [212] can be considered.

6.2.8 Improvement of new system for ultrasound imaging

By substracting corresponding small scatterers echo from the entire echo, the strong scatterers can be stably detected. After that, we can use the SCM framework for strong scatterers. In summary, new system that images organ boundary and organ inside separately should be developed.

Bibliography

[1] L. F. Richardson. Apparatus for warning a ship at sea of its nearness to large objects wholly or partly under water, 05 1912.

[2] A. Manbachi and R. S. C. Cobbold. Development and application of piezoelectric materials for ultrasound generation and detection. *Ultrasound*, 19(4):187–196, 2011.

[3] T. L. Szabo. *Diagnostic Ultrasound Imaging: Inside Out*. Elsevier Academic Press, 2004.

[4] S. Y. Sokolov. Zur frage der fortpflanzung ultrakustischer schwingungen in verschiedenen korpern. *Electr. Nachr. Tech.*, 6:454–461, 1929.

[5] J. J. Wild and D. Neal. Use of high frequency ultrasonic waves for detection changes of texture in living tissue. *Lancet*, 260:655–657, 1951.

[6] T. Cieszynski. Intracardiac method for the investigation of structure of the heart with the aid of ultrasonics. *Arch. Immunol. Ther. Exp. (Warsz).*, 8:551–557, 1960.

[7] I. Donald, J. MacVicar, and T. G. Brown. Investigation of abdominal masses by pulsed ultrasound. *Lancet*, 1(7032):1188–1195, 1960.

[8] N. Born, C. T. Lancee, G. van Zwieten, F. E. Kloster, and J. Roelandt. Multiscan echocardiography. i. technical description. *Circulation*, 48(5):1066–1074, 1973.

[9] M. Pamilo, M. Soiva, and E. M. Lavast. Realtime ultrasound, axillary mammography, and clinical examination in the detection of axillary lymph node metastases in breast cancer patients. *J. Ultrasound Med.*, 8(3):115–120, 1989.

[10] T. G. John, J. D. Greig, J. L. Crosbie, W. F. Miles, and O. J. Garden. Superior staging of liver tumors with laparoscopy and laparoscopic ultrasound. *Annals of Surgery*, 220(6):711–719, 1994.

[11] D. B. Williams, A. V. Sahai, L. Aabakken, I. D. Penman, A. Van Velse, J. Webb, M. Wilson, B. J. Hoffman, and R. H. Hawes. Endoscopic ultrasound guided fine

needle aspiration biopsy: a large single centre experience. *Gut*, 44(5):720–726, 1999.

[12] J. Garcia-Aguilar, J. Pollack, S. H. Lee, E. H. De Anda, A. Mellgren, W. D. Wong, C. O. Finne, D. A. Rothenberger, and R. D. Madoff. Accuracy of endorectal ultrasonography in preoperative staging of rectal tumors. *Diseases of the colon and rectum*, 45(1):10–15, 2002.

[13] M. J. Roman, T. Z. Naqvi, J. M. Gardin, M. Gerhard-Herman, M. Jaff, and E. Mohler. Clinical application of noninvasive vascular ultrasound in cardiovascular risk stratification: a report from the american society of echocardiography and the society of vascular medicine and biology. *Journal of the American Society of Echocardiography*, 19(8):943–954, 2006.

[14] R. S. Cobbold. *Foundations of Biomedical Ultrasound*. Oxford University Press, 2006.

[15] J. W. Hunt, M. Arditi, and F. S.Foster. Ultrasound transducers for pulse-echo medical imaging. *IEEE Transactions on Biomedical Engineering*, 8:453–481, 1983.

[16] M. Postema. *Fundamentals of Medical Ultrasonics*. CRC Press, 2014.

[17] D. R. Dance, S. Christofides, A. D. A. Maidment, I. D. McLean, and K. H. Ng. *Diagnostic Radiology Physics*. International Atomic Energy Agency, 2014.

[18] V. Gibbs, D. Cole, and A. Sassano. *Ultrasound Physics and Technology: How, Why and When*. Elsevier Health Sciences, 2011.

[19] R. Velavan. Applications of ultrasound in medical diagnosis. *Int. Jour. of Biotech Trends and Tech.*, 6(2):37–39, 2016.

[20] K. Lindstrom and I. Edler. The history of echocardiography. *Ultrasound in Med. and Biol.*, 30(12):1565–1644, 2004.

[21] A. Carovac, F. Smajlovic, and D. Junuzovic. Application of ultrasound in medicine. *Acta Inform Med.*, 19(3):168–171, 2011.

[22] B. Ward, A. C. Baker, and V. F. Humphrey. Nonlinear propagation applied to the improvement of resolution in diagnostic medical ultrasound. *Acoustical Society of America*, 101(1):143–154, 1997.

[23] S. H. Kim and B. I. Choi. Three-dimensional and four-dimensional ultrasound: techniques and abdominal applications. *J. Med. Ultrasound*, 15(4):228–242, 2007.

[24] J. Tichy, J. Erhart, E. Kittinger, and J. Privratska. *Fundamentals of Piezoelectric Sensorics: Mechanical, Dielectric, and Thermodynamical Properties of Piezoelectric Materials*. Springer Science and Business Media, 2010.

[25] A. Safari and E. K. Akdogan. *Piezoelectric and Acoustic Materials for Transducer Applications*. Springer Science and Business Media, 2008.

[26] D. Ensminger and L.J. Bond. *Ultrasonics: Fundamentals, Technologies, and Applications*. CRC Press, 2011.

[27] P. Suetens. *Fundamentals of Medical Imaging*. Cambridge University Press, 2002.

[28] M. E. Schafer and P. A. Lewin. The influence of front-end hardware on digital ultrasonic imaging. *IEEE Tran. on Sonics and Ultr.*, 31(4):295–306, 1984.

[29] B. Jaffe, W. R. Cook, and H. Jaffe. *Piezoelectric Ceramics*. Academic New York, 1971.

[30] B. Jaffe, R. S. Roth, and S. Marzullo. Piezoelectric properties of lead zirconate-lead titanate solid-solution ceramics. *J. Appl. Phys.*, 25(6):809–810, 1954.

[31] W. G. Cady. *Piezoelectricity*. New York: McGraw-Hill, 1946.

[32] J. F. Tressler, S. Alkoy, and R. E. Newnham. Piezoelectric sensors and sensor materials. *Journal of Electroceramics*, 2(4):257–272, 1998.

[33] B. Ren and C. J. Lissenden. Pvdf multielement lamb wave sensor for structural health monitoring. *IEEE Trans. Ultrason. Ferroelectr. Freq. Control*, 63(1):178–185, 2016.

[34] M. A. Dubois and P. Muralt. Properties of aluminum nitride thin films for piezoelectric transducers and microwave filter applications. *Appl. Phys. Lett.*, 74(20): 3032–3034, 1999.

[35] Y. Huang, X. Duan, Y. Cui, and C. M. Lieber. Gallium nitride nanowire nanodevices. *Nano Lett.*, 2(2):101–104, 2002.

[36] M. H. Francombe and S. V. Krishnaswamy. Properties of aluminum nitride thin films for piezoelectric transducers and microwave filter applications. *J. Vac. Sci. Technol.*, A8(3):1382–1390, 1990.

[37] Q. F. Zhou, J. Cannata, and K. Kirk Shung. Design and modeling of inversion layer ultrasonic transducers using $linbo_3$ single crystal. *Ultrasonics*, 44:e607–e611, 2006.

[38] P. Han, W. Yan, J. Tian, X. Huang, and H. Pan. Cut directions for the optimization of piezoelectric coefficients of lead magnesium niobatelead titanate ferroelectric crystals. *Appl. Phys. Lett.*, 86(5):052902, 2005.

[39] Y. Chen, K. H. Lam, D. Zhou, and H. L. W. Chan. High-frequency pinpmnpt single crystal ultrasonic transducer for imaging applications. *Appl. Phys. A*, 108 (4):987–991, 2012.

[40] D. Lin, K. W. Kwok, and H. L. W. Chan. Piezoelectric and ferroelectric properties of cu-doped $k_{0.5}na_{0.5}nbo_3$ lead-free ceramics. *Journal of Physics D: Applied Physics*, 41(4):045401, 2008.

[41] R. Cheng, Z. Xu, R. Chu, J. Hao, J. Du, W. Ji, and G. Li. Large piezoelectric effect in $bi_{1/2}na_{1/2}tio_3$-based lead-free piezoceramics. *Ceramics International*, 41 (6):8119–8127, 2015.

[42] C. Beekman, W. Siemons, T. Z. Ward, M. Chi, J. Howe, M. D. Biegalski, N. Balke, P. Maksymovych, A. K. Farrar, J. B. Romero, P. Gao, X. Q. Pan, D. A. Tenne, and H. M. Christen. Phase transitions, phase coexistence, and piezoelectric switching behavior in highly strained $bifeo_3$ films. *Ceramics International*, 25:5561–5567, 2013.

[43] H. J. Lee, S. Zhang, Y. Bar-Cohen, and S. T. Sherrit. High temperature, high power piezoelectric composite transducers. *Sensors*, 14(8):14526–14552, 2014.

[44] M. J. Zipparo, K. F. Bing, and K. R. Nightingale. Imaging arrays with improved transmit power capability. *IEEE Trans. Ultrason. Ferroelectr. Freq. Control*, 57 (9):2076–2090, 2010.

[45] S. Saitoh, M. Izumi, and Y. Mine. A dual frequency ultrasonic probe for medical applications. *IEEE Trans. Ultrason. Ferroelectr. Freq. Control*, 42(2):294–300, 1995.

[46] C. Y. Park, J. H. Sung, and J. S. Jeong. Design and fabrication of ultrasound linear array transducer based on polarization inversion technique. *Sensors and Actuators A: Physical*, 280:484–494, 2018.

[47] S. Takeuchi, T. Sato, S. Wakui, and N. Kawashima. Detection of harmonic ultrasound scattered from microbubbles with ultrasound transducer for harmonic imaging having double peak type frequency characteristics. *Colloids and Surfaces B: Biointerfaces*, 25(3):257–268, 2002.

[48] E. W. Cherin, J. K. Poulsen, A. F. W. van der Steen, P. Lum, and F. S. Foster. Experimental characterization of fundamental and second harmonic beams for a high frequency ultrasound transducer. *Ultrasound Med. Biol.*, 28:635–646, 2002.

[49] H. H. Kim, J. M. Cannata, R. Liu, J. H. Chang, R. H. Silverman, and K. K. Shung. 20 mhz/40 mhz dual element transducers for high frequency harmonic imaging. *IEEE Trans. Ultrason. Ferroelectr. Freq. Control*, 55(12):2683–2691, 2008.

[50] J. Lee, J. Y. Moon, and J. H. Chang. A 35 mhz/105 mhz dual dlement focused transducer for intravascular ultrasound tissue imaging using the third harmonic. *Sensors*, 18(2290):1–14, 2018.

[51] T. Ma, M. Yu, Z. Chen, C. Fei, K. K. Shung, and Q. Zhou. Multi-frequency intravascular ultrasound (ivus) imaging. *IEEE Trans. Ultrason. Ferroelectr. Freq. Control*, 62(1):97–107, 2015.

[52] Q. Q. Zhang, S. J. Gross, S. Tadigadapa, T. N. Jackson, F. T. Djuth, and S. Trolier-McKinstry. Lead zirconate titanate films for d33 mode cantilever actuators. *Sensors and Actuators A: Physical*, 105:91–97, 2003.

[53] A. Safari, A. Halliyal, R. E. Newnham, and I. M. Lachman. Transverse honeycomb composite transducers. *Materials Research Bulletin*, 17(3):301–308, 1982.

[54] Z. Qiu, R. O'Leary, A. Gachagan, and J. Dobson. Design of a low profile array transducer in d_{15} mode for high angled shear wave generation. *IEEE Int. Ultrasonics Symp.*, pages 1–4, 2016.

[55] H. Miao, Q. Huan, F. Li, and G. Kang. A variable-frequency bidirectional shear horizontal (sh) wave transducer based on dual face-shear (d_{24}) piezoelectric wafers. *Ultrasonics*, 89:13–21, 2018.

[56] W. Zhou, H. Li, and F. G. Yuan. Fundamental understanding of wave generation and reception using d_{36} type piezoelectric transducers. *Ultrasonics*, 57:135–143, 2015.

[57] D. G. Wildes, R. Y. Chiao, C. M. W. Daft, K. W. Rigby, L. S. Smith, and K. E. Thomenius. Elevation performance of 1.25d and 1.5d transducer arrays. *IEEE Trans. Ultrason. Ferroelectr. Freq. Control*, 44(5):1027–1037, 1997.

[58] P. G. Barthe and M. H. Slayton. Characterization of 1.5-d ultrasound transducer arrays. *IEEE Int. Ultrasonics Symp.*, 2:1489–1493, 1996.

[59] P. Y. Guo, S. K. Yan, and Q. Zhu. Elevation beamforming performance of a 1.75d array. *IEEE Int. Ultrasonics Symp.*, pages 1113–1116, 2001.

[60] Y. Mendelsohn and E. Wiener-Avnear. Simulations of circular 2d phase-array ultrasonic imaging transducers. *IEEE Trans. Ultrason. Ferroelectr. Freq. Control*, 39:657–666, 2002.

[61] A. Tweedie, V. Murray, and G. Hayward. Aperiodic and deterministic 2d phased array structures for ultrasonic imaging. *IEEE Int. Ultrasonics Symp.*, pages 406–409, 2009.

[62] J. A. Brown, C. Morton-Demore, F. S. Foster, and G. R. Lockwood. Performance of a 50 mhz annular array based imaging system. *IEEE Int. Ultrasonics Symp.*, pages 760–763, 2004.

[63] E. J. Gottlieb, J. M. Cannata, C. H. Hu, and K. K. Shung. Development of a high-frequency (> 50 mhz) copolymer annular-array, ultrasound transducer. *IEEE Trans. Ultrason. Ferroelectr. Freq. Control*, 53(5):1037–1045, 2006.

[64] X. Wang, J. Zhou, J. Song, J. Liu, N. Xu, and Z. L. Wang. Piezoelectric field effect transistor and nanoforce sensor based on a single zno nanowire. *Nano Lett.*, 6(12):2768–2772, 2006.

[65] Z. L. Wang. Nanopiezotronics. *Adv. Mater.*, 19(6):889–892, 2007.

[66] Z. L. Wang. Progress in piezotronics and piezo-phototronics. *Adv. Mater.*, 24: 4623–4646, 2012.

[67] O. Hayden, R. Agarwal, and W. Lu. Semiconductor nanowire devices. *Nano Today*, 3(5-6):12–22, 2008.

[68] S. J. Tans, A. R. M. Verschueren, and C. Dekker. Room-temperature transistor based on a single carbon nanotube. *Nature*, 393(6680):49–52, 1998.

[69] T. Rueckes, K. Kim, E. Joselevich, G. Y. Tseng, C. L. Cheung, and C. M. Lieber. Carbon nanotube-based nonvolatile random access memory for molecular computing. *Science*, 289(5476):94–97, 2000.

[70] W. Liu, M. Lee, L. Ding, J. Liu, and Z. L. Wang. Piezopotential gated nanowire-nanotube hybrid field-effect transistor. *Nano Lett.*, 10(8):3084–3089, 2010.

[71] J. H. He, C. L. Hsin, J. Liu, L. J. Chen, and Z. L. Wang. Piezoelectric gated diode of a single zno nanowire. *Adv. Mater.*, 19(6):781–784, 2007.

[72] P. Bergveld. The development and application of fet-based biosensors. *Biosensors*, 2:15–33, 1986.

[73] A. Tixier-Mita, S. Ihida, B. Segard, G. A. Cathcart, T. Takahashi, H. Fujita, and H. Toshiyoshi. Review on thin-film transistor technology, its applications, and possible new applications to biological cells. *Jpn. J. Appl. Phys.*, 55:04EA08, 2016.

[74] I. Graz, M. Krause, S. Bauer-Gogonea, S. Bauer, S. P. Lacour, B. Ploss, M. Zirkl, B. Stadlober, and S. Wagner. Flexible active-matrix cells with selectively poled bifunctional polymer-ceramic nanocomposite for pressure and temperature sensing skin. *J. App. Phys.*, 106:034503, 2009.

[75] S. M. Jejurikar, M. M. De Souza, and K. P. Adhib. Understanding the role of the insulator in the performance of zno tfts. *Thin Solid Films*, 518(4):1177–1179, 2009.

[76] M. T. Kao and J. FinLin. Electrical properties of aln_x/al/mo composite film prepared for use in thin-film transistors. *Thin Solid Films*, 518(14):3917–3922, 2010.

[77] T. P. Brody, J. A. Asars, and G. D. Dixon. A 6 × 6 inch 20 lines-per-inch liquid-crystal display panel. *IEEE Tran. Electron Dev.*, 20(11):995–1001, 1973.

[78] P. G. LeComber, W. E. Spear, and A. Ghaith. Amorphous-silicon field-effect device and possible application. *Electronics Lett.*, 15(6):179–181, 1979.

[79] S. Kim, X. Zhang, R. Daugherty, E. Lee, G. Kunnen, D. R. Allee, E. Forsythe, and J. Chae. Microelectromechanical systems (mems) based-ultrasonic electrostatic actuators on a flexible substrate. *IEEE Tran. Electron Dev.*, 33(7):1072–1074, 2012.

[80] T. Someya, Y. Kato, T. Sekitani, S. Iba, Y. Noguchi, Y. Murase, H. Kawaguchi, and T. Sakurai. Conformable, flexible, large-area networks of pressure and thermal sensors with organic transistor active matrixes. *Proc. National Acad. Sci.*, 35(102): 12321–12325, 2005.

[81] Y. Kato, T. Sekitani, Y. Noguchi, T. Yokota, M. Takamiya, T. Sakurai, and T. Someya. Large-area flexible ultrasonic imaging system with an organic transistor active matrix. *IEEE Tran. Electron Dev.*, 57(5):995–1002, 2010.

[82] K. Fukuda, Y. Takeda, M. Mizukami, D. Kumaki, and S. Tokito. Fully solution-processed flexible organic thin film transistor arrays with high mobility and exceptional uniformity. *Sci. Rep.*, 4:3947, 2014.

[83] D. Khodagholy, T. Doublet, P. Quilichini, M. Gurfinkel, P. Leleux, A. Ghestem, E. Ismailova, T. Herve, S. Sanaur, C. Bernard, and G. G. Malliaras. In vivo recordings of brain activity using organic transistors. *Nat. Communications*, 4: 1575, 2013.

[84] O. Oralkan, A. S. Ergun, C. H. Cheng, J. A. Johnson, M. Karaman, T. H. Lee, and B. T. Khuri-Yakub. Volumetric ultrasound imaging using 2-d cmut array. *IEEE Trans. Ultrason. Ferroelectr. Freq. Control*, 50(11):1581–1594, 2003.

[85] D. E. Dausch, J. B. Castellucci, D. R. Chou, and O. T. von Ramm. Piezoelectric micromachined ultrasound transducer (pmut) arrays for 3d imaging probes. *IEEE Int. Ultrasonics Symp.*, pages 930–933, 2006.

[86] D. E. Dausch, K. H. Gilchrist, J. B. Castellucci, D. R. Chou, and O. T. von Ramm. Performance of flexure-mode pmut 2d arrays. *IEEE Int. Ultrasonics Symp.*, pages 1053–1056, 2007.

[87] I. O. Wygant, X. Zhuang, D. T. Yeh, A. Nikoozadeh, O. Oralkan, A. S. Ergun, M. Karaman, and B. T. Khuri-Yakub. Integrated ultrasonic imaging systems based on cmut arrays: recent progress. *IEEE Int. Ultrasonics Symp.*, 1:391–394, 2004.

[88] I. O. Wygant, X. Zhuang, D. T. Yeh, O. Oralkan, A. S. Ergun, M. Karaman, and B. T. Khuri-Yakub. Integration of 2d cmut arrays with front-end electronics for volumetric ultrasound imaging. *IEEE Trans. Ultrason. Ferroelectr. Freq. Control*, 55(2):327–342, 2008.

[89] F. Y. Lin, W. C. Tian, and P. C. Li. Cmos-based capacitive micromachined ultrasonic transducers operating without external dc bias. *IEEE Int. Ultrasonics Symp.*, pages 1420–1423, 2013.

[90] R. Reger, A. Edstrand, and B. Griffin. Post-complementary-metal-oxide-semiconductor compatible piezoelectric micro-machined ultrasonic transducers. *IEEE Int. Ultrasonics Symp.*, 2018.

[91] J. A. Jensen. Deconvolution of ultrasound images. *Ultrasonic Imaging*, 14(1):1–15, 1992.

[92] J. A. Jensen, J. Mathorne, T. Gravesen, and B. Stage. Deconvolution of in vivo ultrasound b-mode images. *Ultrasonic Imaging*, 15(2):122–133, 1993.

[93] O. Michailovich and A. Tannenbaum. Blind deconvolution of medical ultrasound images: A parametric inverse filtering approach. *IEEE Tran. Image Proc.*, 16(12): 3005–3019, 2007.

[94] R. Jirik and T. Taxt. High-resolution ultrasonic imaging using two-dimensional homomorphic filtering. *IEEE Trans. Ultrason. Ferroelectr. Freq. Control*, 53(8): 1440–1448, 2006.

[95] J. A. Jensen and S. Leeman. Nonparametric estimation of ultrasound pulses. *IEEE Tran. Bio. Eng.*, 41(10):929–936, 1994.

[96] N. Wiener. *Extrapolation, Interpolation, and Smoothing of Stationary Time Series: with Engineering Applications.* MIT Press, 1949.

[97] B. Mandersson and G. Salomonsson. Weighted least-squares pulse-shaping filters with application to ultrasonic signals. *IEEE Trans. Ultrason. Ferroelectr. Freq. Control*, 36(1):109–113, 1989.

[98] C. Y. Chi and J. M. Mendel. Performance of minimum-variance deconvolution filter. *IEEE Trans. Acoustics, Speech, and Signal Proc.*, 32(6):1145–1154, 1984.

[99] D. W. Oldenburg. A comprehensive solution to the linear deconvolution problem. *Geophys. J. R. Astr. Society*, 65(2):331–357, 1981.

[100] B. Drachman. Two methods to deconvolve: L1-method using simplex algorithm and l2-method using least squares and a parameter. *IEEE Trans. Ant. Propag.*, 32(3):219–225, 1984.

[101] X. M. Lu, J. M. Reid, and S. H. Wang. A practical application of l1 deconvolution for medical ultrasound. *IEEE Int. Ultrasonics Symp.*, pages 1177–1180, 1991.

[102] R. Demirli and J. Saniie. Model-based estimation of ultrasonic echoes. part i: analysis and algorithms. *IEEE Trans. Ultrason. Ferroelectr. Freq. Control*, 48(3): 787–802, 2001.

[103] W. Liang, P. W. Que, H. M. Lei, and L. Chen. Matching pursuit for decomposition and approximation of ultrasonic pulse-echo wavelet and its application in ultrasonic nondestructive evaluation. *Rev. Sci. Instrum.*, 79(7):075105, 2008.

[104] K. Koh, S. J. Kim, and S. P. Boyd. Model-based estimation of ultrasonic echoes. part i: analysis and algorithms. *J. Mach. Learn. Res.*, 8:1519–1555, 2007.

[105] J. M. Bioucas-Dias and M. A. Figueiredo. A new twist: two-step iterative shrinkage/thresholding algorithms for image restoration. *IEEE Trans. Image Proc.*, 16 (12):2992–3004, 2007.

[106] G. Hayward and J. E. Lewis. Comparison of some non-adaptive deconvolution techniques for resolution enhancement of ultrasonic data. *Ultrasonics*, 27(3):155–164, 1989.

[107] X. Zhang, M. Burger, X. Bresson, and S. Osher. Bregmanized nonlocal regularization for deconvolution and sparse reconstruction. *SIAM J. Imag. Sci.*, 3(3): 253–276, 2010.

[108] M.Alessandri. *Statistical Methods for Analysis and Processing of Medical Ultrasound*. PhD thesis, University of Bologna, 2008.

[109] M. A. T. Figueiredo and R. D. Nowak. An em algorithm for wavelet-based image restoration. *IEEE Trans. Image Proc.*, 12(8):906–916, 2003.

[110] J. M. Bioucas-Dias. Bayesian wavelet-based image deconvolution: a gem algorithm exploiting a class of heavy-tailed priors. *IEEE Trans. Image Proc.*, 15(4):937–951, 2006.

[111] J. Ng, R. Prager, N. Kingsbury, G. Treece, and A. Gee. Wavelet restoration of medical pulse-echo ultrasound images in an em framework. *IEEE Trans. Ultrason. Ferroelectr. Freq. Control*, 54(3):550–568, 2007.

[112] O. V. Michailovich and D. Adam. A novel approach to the 2-d blind deconvolution problem in medical ultrasound. *IEEE Trans. Med. Imag.*, 24(1):86–104, 2005.

[113] Harry C. Andrews and B. R. Hunt. *Digital Image Restoration*. PrenticeHall Professional Technical Reference, 1977.

[114] P. Mohana Shankar. A general statistical model for ultrasonic backscattering from tissues. *IEEE Trans. Ultrason. Ferroelectr. Freq. Control*, 47(3):727–736, 2000.

[115] S. Boyd and L. Vandenberghe. *Convex Optimization*. Cambridge university press, 2004.

[116] S. Maggio, M. Alessandrini, L. De Marchi, and N. Speciale. Computer aided detection of prostate cancer based on gda and predictive deconvolution. *IEEE Int. Ultrasonics Symp.*, pages 28–31, 2008.

[117] J. A. Jensen. Estimation of pulses in ultrasound b-scan images. *IEEE Trans. Med. Imag.*, 10(2):164–172, 1991.

[118] J. A. Jensen. Estimation of in-vivo pulses in medical ultrasound. *Ultrasonic Imaging*, 16(3):190–203, 1994.

[119] N. Testoni. *Adaptive Multiscale Biological Signal Processing*. PhD thesis, University of Bologna, 2008.

[120] S. Maggio, A. Palladini, L. De Marchi, M. Alessandrini, N. Speciale, and G. Masetti. Predictive deconvolution and hybrid feature selection for computer-aided detection of prostate cancer. *IEEE Trans. Med. Imag.*, 29(2):455–464, 2010.

[121] X. Zhang, M. Burger, X. Bresson, and S. Osher. Restoration of medical ultrasound images using two dimensional homomorphic deconvolution. *IEEE Trans. Ultrason. Ferroelect., Freq. Contr.*, 42(4):543–553, 1995.

[122] O. Michailovich and A. Tannenbaum. Despeckling of medical ultrasound images. *IEEE Trans. Ultrason. Ferroelect., Freq. Contr.*, 53(1):64–78, 2006.

[123] O. Michailovich and A. Tannenbaum. Blind deconvolution of medical ultrasound images: A parametric inverse filtering approach. *IEEE Trans. Image Proc.*, 16 (12):3005–3019, 2007.

[124] J. Zhu and N. Tagawa. Restoration of scatterer distribution based on empirical bayesian learning with consideration of statistical properties. *Proc. Mtgs. Acoust.*, 32:020005, 2017.

[125] K. E. Thomenius. Evolution of ultrasound beamformers. *IEEE Int. Ultrasonics Symp.*, 2:1615–1622, 1996.

[126] M. Sadeghi and A. Mahloojifar. Improving beamforming performance by phased synthetic aperture imaging in medical ultrasound. *J. Ultrasound Med.*, 44(1): 51–62, 2017.

[127] J. Camacho, M. Parrilla, and C. Fritsch. Phase coherence imaging. *IEEE Trans. Ultrason. Ferroelectr. Freq. Control*, 56(5):958–974, 2009.

[128] J. Capon. High-resolution frequency-wavenumber spectrum analysis. *Proc. IEEE*, 57(8):1408–1418, 1969.

[129] Z. Wang, J. Li, L. De Marchi, M. Alessandrini, N. Speciale, and G. Masetti. Time-delay- and time-reversal-based robust capon beamformers for ultrasound imaging. *IEEE Trans. Med. Imag.*, 24(10):1308–1322, 2005.

[130] J. F. Synnevag, A. Austeng, and S. Holm. Benefits of minimum-variance beamforming in medical ultrasound imaging. *IEEE Trans. Ultrason. Ferroelectr. Freq. Control*, 56(9):1868–1879, 2009.

[131] S. Mehdizadeh, A. Austeng, T. F. Johansen, and S. Holm. Minimum variance beamforming applied to ultrasound imaging with a partially shaded aperture. *IEEE Trans. Ultrason. Ferroelectr. Freq. Control*, 59(4):683–693, 2012.

[132] S. Okumura, H. Taki, and T. Sato. High-contrast and low-computational complexity medical ultrasound imaging using beamspace capon method. *37th Annual Int. Conference of the IEEE Engineering in Med. and Bio. Society*, pages 6334–6337, 2015.

[133] S. Okumura, H. Taki, and T. Sato. Stabilization techniques for high resolution ultrasound imaging using beamspace capon method. *IEEE Int. Conference on Acoustics, Speech and Signal Proc.*, pages 892–896, 2015.

[134] R. Schmidt. *A signal subspace approach to multiple emitter location and spectral estimation.* PhD thesis, Stanford University, 1981.

[135] W. Zhang and A. Hoorfar. Through-the-wall target localization with time reversal music method. *Progress In Electromagnetics Research*, 106:75–89, 2010.

[136] F. Yan, Y. Shen, M. Jin, and X. Qiao. Computationally efficient direction finding using polynomial rooting with reduced-order and real-valued computations. *Journal of Systems Engineering and Electronics*, 27(4):739–745, 2016.

[137] M. Pesavento, A. B. Gershman, and M. Haardt. Unitary root-music with a real-valued eigendecomposition: A theoretical and experimental performance study. *IEEE Transactions on Signal Processing*, 48(5):1306–1314, 2000.

[138] H. Krim and M. Viberg. Two decades of array signal processing research: the parametric approach. *IEEE Signal Proc. Magazine*, 13(4):67–94, 1996.

[139] P. Stoica and K. C. Sharman. Maximum likelihood methods for direction-of-arrival estimation. *IEEE Trans. Acoustics, Speech and Signal Proc.*, 38(7):1132–1143, 1990.

[140] H. B. Lim, N. T. T. Nhung, E. P. Li, and N. D. Thang. Confocal microwave imaging for breast cancer detection: Delay-multiply-and-sum image reconstruction algorithm. *IEEE Trans. Biomed. Eng.*, 55(6):1697–1704, 2008.

[141] J. Park, S. Jeon, J. Meng, L. Song, J. S. Lee, and C. Kim. Delay-multiply-and-sum-based synthetic aperture focusing in photoacoustic microscopy. *Journal of biomedical optics*, 21(3):036010, 2016.

[142] S. Maggio, M. Alessandrini, L. De Marchi, and N. Speciale. Low-complexity delay-multiply-and-sum (dmas) beamforming using baseband spatial coherence. *IEEE Int. Ultrasonics Symp.*, 2018.

[143] G. Matrone, A. Savoia, G. Caliano, and G. Magenes. The delay multiply and sum beamforming algorithm in ultrasound b-mode medical imaging. *IEEE Trans. Med. Imag.*, 34(4):940–949, 2015.

[144] G. Matrone, A. Ramalli, P. Tortoli, and G. Magenes. Experimental evaluation of ultrasound higher-order harmonic imaging with filtered-delay multiply and sum (f-dmas) non-linear beamforming. *Ultrasonics*, 86:59–68, 2018.

[145] M. F. Schiffner and G. Schmitz. Fast image acquisition in pulse-echo ultrasound imaging using compressed sensing. *IEEE Int. Ultrasonics Symp.*, pages 1944–1947, 2012.

[146] Z. Chen, A. Basarab, and D. Kouame. Compressive deconvolution in medical ultrasound imaging. *IEEE Tran. Med. Imag.*, 35(3):728–737, 2016.

[147] M. Mozaffarzadeh and M. Orooji. Image enhancement and noise reduction using modified delay-multiply-and-sum beamformer: Application to medical photoacoustic imaging. *25th Iranian Con. Elec. Eng.*, pages 65–69, 2017.

[148] B. M. Asl and A. Mahloojifar. Minimum variance beamforming combined with adaptive coherence weighting applied to medical ultrasound imaging. *IEEE Trans. Ultrason. Ferroelectr. Freq. Control*, 56(9):1923–1931, 2009.

[149] M. Mozaffarzadeh, A. Mahloojifar, and M. Orooji. Medical photoacoustic beamforming using minimum variance-based delay multiply and sum. *Digital Optical Tech.*, 10335:1033522, 2017.

[150] M. Mozaffarzadeh, A. Mahloojifar, M. Orooji, S. Adabi, and M. Nasiriavanaki. Double stage delay multiply and sum beamforming algorithm: Application to linear-array photoacoustic imaging. *IEEE Tran. Bio. Eng.*, 65(1):31–42, 2018.

[151] Y. P. Zheng, R. G. Maev, and I. Y. Solodov. Nonlinear acoustic applications for material characterization: a review. *Can. J. Phys.*, 77(12):927–967, 1999.

[152] N. Park, H. Kang, J. Park, Y. Lee, Y. Yun, J. H. Lee, S. G. Lee, Y. H. Lee, and D. Suh. Ferroelectric single-crystal gated graphene/hexagonal-bn/ferroelectric field-effect transistor. *ACS Nano.*, 9:10729–10736, 2015.

[153] C. S. Lao, Q. Kuang, and Z. L. Wang. Polymer functionalized piezoelectric-fet as humidity/chemical nanosensors. *Appl. Phys. Lett.*, 90:262107, 2007.

[154] C. T. Lee and Y. S. Chiu. Piezoelectric zno-nanorod-structured pressure sensors using gan-based field-effect-transistor. *Appl. Phys. Lett.*, 106:073502, 2015.

[155] M. Sung, K. Shin, and W. Moon. A micro-machined hydrophone employing a piezoelectric body combined on the gate of a field-effect transistor. *Sensors and Actuators A: Physical*, 237:155–166, 2016.

[156] P. Fei, P. H. Yeh, J. Zhou, S. Xu, Y. Gao, J. Song, Y. Gu, Y. Huang, and Z. L. Wang. Piezoelectric potential gated field-effect transistor based on a free-standing zno wire. *Nano Lett.*, 9:3435–3439, 2009.

[157] N. T. Tien, T. Q. Trung, Y. G. Seoul, D. I. Kim, and N. E. Lee. Physically responsive field-effect transistors with giant electromechanical coupling induced by nanocomposite gate dielectrics. *ACS Nano*, 5:7069–7076, 2011.

[158] A. Manbachi and R. S. C. Cobbold. Development and application of piezoelectric materials for ultrasound generation and detection. *Ultrasound*, 19:187–196, 2011.

[159] E. E. Aktakka, R. L. Petersin, and K. Najafi. A cmos-compatible piezoelectric vibration energy scavenger based on the integration of bulk pzt films on silicon. *IEEE Int. Electron Devices Meeting*, 31:1–4, 2010.

[160] X. C. Jin, O. Oralkan, F. L. Degertekin, and B. T. Khuri-Yakub. Characterization of one-dimensional capacitive micromachined ultrasonic immersion transducer arrays. *IEEE Trans. Ultrason. Ferroelectr. Freq. Control*, 48:750–760, 2001.

[161] U. Demirci, A. S. Ergun, O. Oralkan, M. Karaman, and B. T. Khuri-Yakub. Forward-viewing cmut arrays for medical imaging. *IEEE Trans. Ultrason. Ferroelectr. Freq. Control*, 51:887–895, 2004.

[162] Y. Ishiguro, J. Zhu, N. Tagawa, T. Okubo, and K. Okubo. Characteristic analysis of diaphragm-type transducer that is thick relative to its size. *Jpn. J. Appl. Phys.*, 56:07JD11, 2017.

[163] S. M. Leinders, K. W. A. van Dongen, N. de Jong, M. D. Verweij, W. J. Westerveld, H. P. Urbach, P. L. M. J. van Neer, and J. Pozo. Membrane design of an all-optical ultrasound receiver. *IEEE Int. Ultrasonics Symp.*, pages 2175–2178, 2013.

[164] D. E. Dausch, J. B. Castellucci, D. R. Chou, and O. T. von Ramm. Theory and operation of 2-d array piezoelectric micromachined ultrasound transducers. *IEEE Trans. Ultrason. Ferroelectr. Freq. Control*, 55:2484–2492, 2008.

[165] C. S. Lam. A review of the recent development of mems and crystal oscillators and their impacts on the frequency control products industry. *IEEE Int. Ultrasonics Symp.*, pages 694–704, 2008.

[166] T. L. Ren, H. Chen, Y. Yang, Y. P. Zhu, D. Fu, C. Wang, X. M. Wu, J. Cai, L. T. Liu, and Z. J. Li. Micromachined piezoelectric acoustic device. *Proc. IEEE 2nd Int. Workshop Electron Devices and Semiconductor Tech.*, June 2009.

[167] Q. Liang, I. Wendelhag, J. Wikstrand, and T. Gustavsson. A multiscale dynamic programming procedure for boundary detection in ultrasonic artery images. *IEEE Trans. Med. Imag.*, 19(2):127–142, 2000.

[168] J. A. Noble and D. Boukerroui. Ultrasound image segmentation: a survey. *IEEE Trans. Med. Imag.*, 25(8):987–1010, 2006.

[169] M. E. Plissiti, D. I. Fotiadis, L. K. Michalis, and G. E. Bozios. An automated method for lumen and media-adventitia border detection in a sequence of ivus frames. *IEEE Trans. Infor. Tech. in Biomedicine*, 8(2):131–141, 2004.

[170] K. Z. Abd-Elmoniem, A. B. M. Youssef, and Y. M.Kadah. Real-time speckle reduction and coherence enhancement in ultrasound imaging via nonlinear anisotropic diffusion. *IEEE Trans. Biomedical Eng.*, 49(9):997–1014, 2002.

[171] F. Zhang, Y. Mo Yoo, L. Mong Koh, and Y. Kim. Nonlinear diffusion in laplacian pyramid domain for ultrasonic speckle reduction. *IEEE Trans. Med. Imag.*, 26(2): 200–211, 2007.

[172] S. K. Narayanan and R. S. D. Wahidabanu. A view on despeckling in ultrasound imaging. *Int. Journal Signal Proc., Image Proc. and Pattern Recognition*, 2(3): 85–98, 2009.

[173] D. Friboulet, H. Liebgott, and R. Prost. Compressive sensing for raw rf signals reconstruction in ultrasound. *IEEE Int. Ultrasonics Symp.*, pages 367–370, 2010.

[174] H. Liebgott, R. Prost, and D. Friboulet. Pre-beamformed rf signal reconstrcution in medical ultrasound using compressive sensing. *Ultrasonics*, 53(2):525–533, 2013.

[175] H. Suzuki, N. Tagawa, and K. Okubo. A study on speckle reduction based on stochastic fluctuation of transmitted ultrasound beam. *IEEE Int. Ultrasonics Symp.*, pages 910–913, 2013.

[176] T. Wada, Y. Ho, K. Okubo, N. Tagawa, and Y. Hirose. High frame rate super resolution imaging based on ultrasound synthetic aperture scheme. *Physics Procedia*, pages 1216–1220, 2015.

[177] T. Yamamura, M. Tanabe, K. Okubo, and N. Tagawa. A method for improving signal-to-noise ratio of tissue harmonic imaging based on bayesian inference using information of fundamental echoes. *Jpn. J. Appl. Phys.*, 51:07GF01, 2012.

[178] T. Hiraoka, N. Tagawa, K. Okubo, Y. Ho, and I. Akiyama. Compensation method for frequency dependent attenuation for tissue harmonic imaging. *IEEE Int. Ultrasonics Symp.*, pages 1085–1088, 2014.

[179] B. P. Carlin and T. A. Louis. Bayes and empirical bays methods for data analysis. *Statistics and Computing*, 7(2):153–154, 1997.

[180] D. P. Wipf and B. D. Rao. An empirical bayesian strategy for solving the simultaneous sparse approximation problem. *IEEE Trans. Signal Processing*, 55(7): 3704–3716, 2007.

[181] A. Sarti, C. Corsi, E. Mazzini, and C. Lamberti. Maximum likelihood segmentation of ultrasound images with rayleigh distribution. *IEEE Trans. Ultrason. Ferroelectr. Freq. Control*, 52(6):947–960, 2005.

[182] N. Tagawa and S. Tsukada. Selective use of appropriate image pairs for shape from multiple motions based on gradient method. *Proc. Int. Conf. Computer vision Theory and Appl.*, pages 554–563, 2016.

[183] M. Mozumi, R. Nagaoka, and H. Hasegawa. Improvement of high-range-resolution imaging by considering change in ultrasonic waveform during propagation. *Jpn. J. Appl. Phys.*, 57:07LF23, 2018.

[184] Y. Kobayashi, T. Azuma, K. Shimizu, M. Koizumi, T. Oya, R. Suzuki, K. Maruyama, K. Seki, and S. Takagi. Development of focus controlling method with transcranial focused ultrasound aided by numerical simulation for noninvasive brain therapy. *Jpn. J. Appl. Phys.*, 57:07LF22, 2018.

[185] H. Nomura, H. Adachi, and T. Kamakura. Feasibility of low-frequency ultrasound imaging using pulse compressed parametric ultrasound. *Ultrasonics*, 89:64–73, 2018.

[186] M. Tanabe, T. Yamamura, K. Okubo, and N. Tagawa. Medical ultrasound imaging using pulse compression technique based on split and merge strategy. *Jpn. J. Appl. Phys.*, 79(7S):07HF15, 2010.

[187] Y. Asakura, K. Okubo, and N. Tagawa. Experimental evaluation of long-range acoustic sensing using super-directivity speaker and super-resolution signal processing with pulse compression technique. *Jpn. J. Appl. Phys.*, 56:07JC14, 2017.

[188] K. Yamanaka, S. Hirata, and H. Hachiya. Evaluation of correlation property of linear-frequency-modulated signals coded by maximum-length sequences. *Jpn. J. Appl. Phys.*, 55:07KC09, 2016.

[189] H. Nomura and R. Nishioka. Time sidelobe reduction of pulse-compressed parametric ultrasound with maximum-length sequence excitation. *Jpn. J. Appl. Phys.*, 57:07LC05, 2018.

[190] A. Ponnle, H. Hasegawa, and H. Kanai. Multi element diverging beam from a linear array transducer for transverse cross sectional imaging of carotid artery: simulations and phantom vessel validation. *Jpn. J. Appl. Phys.*, 50(7S):07HF05, 2011.

[191] H. Hasegawa and H. Kanai. Effect of element directivity on adaptive beamforming applied to high-frame-rate ultrasound. *IEEE Trans. Ultrason. Ferroelectr. Freq. Control*, 62(3):511–523, 2015.

[192] Y. Wang, C. Zheng, H. Peng, and Q. Chen. An adaptive beamforming method for ultrasound imaging based on the mean-to-standard-deviation factor. *Ultrasonics*, 90:32–41, 2018.

[193] M. S. Salim, M. F. Abd Malek, R. B. W. Heng, and N. Sabri. Capacitive micromachined ultrasonic transducers: Technology and application. *J. Ultrasound Med.*, 20(1):8–31, 2012.

[194] Y. Roh. Ultrasonic transducers for medical volumetric imaging. *Jpn. J. Appl. Phys.*, 53(7S):07KA01, 2014.

[195] H. Takahashi, H. Hasegawa, and H. Kanai. Echo speckle imaging of blood particles with high-frame-rate echocardiography. *Jpn. J. Appl. Phys.*, 53(7S):07KF08, 2014.

[196] N. Gonzalez-Salido, L. Medina, and J. Camacho. Full angle spatial compound of arfi images for breast cancer detection. *Ultrasonics*, 71:161–171, 2016.

[197] F. Zhao and J. Luo. Diverging wave compounding with spatio-temporal encoding using orthogonal golay pairs for high frame rate imaging. *Ultrasonics*, 89:155–165, 2018.

[198] W. Guo, Y. Wang, and J. Yu. Ultrasound harmonic enhanced imaging using eigenspace-based coherence factor. *Ultrasonics*, 72:106–116, 2016.

[199] Y. Deng, M. L. Palmeri, N. C. Rouze, G. E. Trahey, C. M. Haystead, and K. R. Nightingale. Quantifying image quality improvement using elevated acoustic output in b-mode harmonic imaging. *Ultrasonics*, 43:2416–2425, 2017.

[200] G. Matrone, A. Ramalli, P. Tortoli, and G. Magenes. Experimental evaluation of ultrasound higher-order harmonic imaging with filtered-delay multiply and sum (f-dmas) non-linear beamforming. *Ultrasonics*, 86:59–68, 2018.

[201] M. Fujiwara, K. Okubo, and N. Tagawa. A novel technique for high resolution ultrasound imaging super resolution fm-chirp correlation method (scm). *IEEE Int. Ultrasonics Symp.*, pages 2390–2393, 2009.

[202] J. Zhu and N. Tagawa. Computationally efficient super resolution ultrasound imaging based on multiple transmission/reception with different carrier frequencies. *Proc. Mtgs. Acoust.*, 32:055001, 2017.

[203] K. Dei and B. Byram. A robust method for ultrasound beamforming in the presence of off-axis clutter and sound speed variation. *Ultrasonics*, 89:34–45, 2018.

[204] R. Schmidt. Multiple emitter location and signal parameter estimation. *IEEE Trans. Antennas Propag.*, 34:276–280, 1986.

[205] H. Hasegawa. Improvement of range spatial resolution of medical ultrasound imaging by element-domain signal processing. *Jpn. J. Appl. Phys.*, 56(7S1):07JF02, 2017.

[206] S. Goto, M. Nakamura, and K. Uosaki. On-line spectral estimation of nonstationary time series based on ar model parameter estimation and order selection with a forgetting factor. *IEEE Trans. Signal Processing*, 43(7S):1519–1522, 1995.

[207] C. Li, L. Huang, N. Duric, H. Zhang, and C. Rowe. An improved automatic time-of-flight picker for medical ultrasound tomography. *Ultrasonics*, 49(1):61–72, 2009.

[208] X. Li, X. Shang, A. Morales-Esteban, and Z. Wang. Identifying p phase arrival of weak events: the akaike information criterion picking application based on the empirical mode decomposition. *Computers and Geosciences*, 100:57–66, 2017.

[209] M. Wax and I. Ziskind. Detection of the number of coherent signals by the mdl principle. *IEEE Trans. Acoustics, Speech, and Signal Proc.*, 37:1190–1196, 1989.

[210] L. Kaur, R. C. Chauhan, and S. C. Saxena. Space-frequency quantiser design for ultrasound image compression based on minimum description length criterion. *Med. Biol. Eng. Comput.*, 43(1):33–39, 2005.

[211] T. Joel and R. Sivakumar. An extensive review on despeckling of medical ultrasound images using various transformation techniques. *Ultrasonics*, 138:18–27, 2018.

[212] R. Kozai, J. Zhu, K. Okubo, and N. Tagawa. Improvement of range resolution of fdmas beamforming in. ultrasound imaging. *14th International Joint Conference on Computer Vision, Imaging and Computer Graphics Theory and Applications*, page 252, 2019.